Toxicology of Nanoparticles after Cellular Uptake

Crystal Cheng

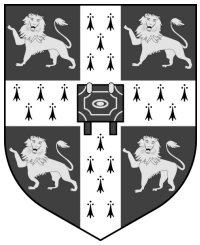

Dissertation submitted for the degree of

Doctor of Philosophy

St John's College

Department of Engineering

University of Cambridge

August 2009

Preface

This dissertation is a culmination of the research completed at the Nanoscience Centre and the Multi-Imaging Centre (Department of Physiology, Development and Neuroscience) at the University of Cambridge. It is the result of my own work and includes nothing which is the outcome of work done in collaboration except where specifically indicated in the text. None of the work has been submitted for any other degree, diploma, or qualifications. The text contains approximately 34,000 words which does not exceed the 65,000 limit.

Abstract

Nanoscience is a multi-disciplinary field with the potential to both create new applications and understand existent systems, but its materials may be sources of toxicological concern. Understanding their toxic potential becomes essential to prevent any occupational, environmental, and consumer hazards. In this study, the toxicity of three different nanoparticles (NPs) was assessed: multi-walled carbon nanotubes (MWNTs), single-walled carbon nanotubes (SWNTs), and zinc oxide (ZnO) nanopowders. A combination of cell viability assays—NR, MTT, LDH, live dead—and microscopy—TEM, SEM, confocal—was used. No direct interactions occurred with any of the assays except the NR and ZnO nanopowders at > 50 μg/mL.

The overall cytotoxic trend was ZnO > MWNT > SWNT. Both uncoated and PVA-coated ZnO nanopowders exhibited dose dependent toxicity with a sudden rate of increase between 12.5 and 25 μg/mL. Zn^{2+} cations appeared to be the major toxic source. Cytotoxic curves of ZnO nanopowders were similar to $ZnCl_2$, a chemical known to dissociate into Zn^{2+} + Cl^{-}, and a stereological analysis indicated specific mitochondrial damage, a condition associated with Zn^{2+} neurotoxicity. Zinc dissolution also increased with decreasing cell pH. Unpurified and purified MWNTs exhibited dose and time dependent toxicity with necrosis as the main mechanism of cell death. The residual iron Fe_2O_3 yielded no toxicity suggesting the nanotubes themselves as the toxic source. MWNTs entered cells both actively and passively and were found in the cytoplasm and nuclei. Only HiPco SWNTs caused significant cell death; none was observed for the unpurified and purified SWNTs. At the concentrations tested, this study found that both ZnO nanopowders and MWNTs caused acute toxicity while SWNTs were not acutely toxic. All three NPs should remain in the research and development stage until further studies can fully characterise their relationship with cells.

Acknowledgments

It has been an honour and privilege to study at the University of Cambridge. This PhD degree would not have been accomplished without the immense support and assistance from numerous people. I would first like to thank my supervisor, Professor Mark E. Welland, for his positive support throughout all three years. My gratitude extends to my two advisors: Alexandra E. Porter, who helped me establish a strong foundation in the first half of the project and for her enthusiasm, ideas, and constant support, and Jeremy N. Skepper, who provided training when needed, assisted with numerous experiments, and was a constant source of expertise, advice, and guidance. My colleague, Karin H. Müller, has been indispensable; she has been the main provider of macrophage cells, and she has always been available to provide experimental knowledge, open to idea exchange, and willing to assist experimentally. Similarly, I thank Krzysztof K. Koziol for his supply and characterisation of samples, patience with explaining the materials science, and earnestness to help despite schedule constraints. Additional thanks goes to Michael Motskin, James Bendall, and Emma Watson for their experimental assistance. I would like to express my sincerest appreciation to my family: to my fiancé, Ian Pong, my model Cambridge PhD forerunner and immediate support; to my older brother, Owen Cheng, my lifelong role model (and another PhD forerunner) who is always present remotely to assist or lend an ear regardless of time zone differences; and to my parents, whom I am forever indebted to for their tireless support, nurturing care, and heartfelt sacrifices. I would like to thank my college, St. John's College, for being my home away from home. Last, but not least, are my funding sources—the Overseas Research Studentship, the Cambridge Overseas Trust, and the funders of the Interdisciplinary Research Collaboration (IRC) in Nanotechnology—for which, without their support, this project would not have been possible.

Contents

List of Figures

List of Tables

List of Abbreviations

3-D	Three-dimension
A549	Human type II lung epithelial cells
AgI	Silver iodide
BET	Brunauer Emmett and Teller
BF TEM	Bright field transmission electron microscopy
BSA	Bovine serum albumin
CB	Carbon black
CNT	Carbon nanotube
CVD	Chemical vapour deposition
DIW	De-ionised water
EDX	Energy dispersive x-ray
Fe	Iron
HEK	Human epithelial keratinocytes
HMM	Human monocyte-derived macrophage cell
ICP-AES	Inductively coupled plasma atomic emission spectroscopy
J774.1	Mouse macrophage cells
Jurkat	Human tumour T lymphocytes
LDH	Lactase dehydrogenase
LSD	Least significant difference
MWNT	Multi-walled carbon nanotube
MTS	3-(4,5- dimethylthiazol-2-yl)-5-(3-carboxymethoxyphenyl)-2-(4-sulfophenyl)-2H-tetrazolium

MTT	3-(4,5-Dimethylthiazol-2-yl)-2,5-diphenyltetrazolium bromide
NP	Nanoparticle
NR	Neutral red
PBS	Phosphate-buffered saline
ROS	Reactive oxygen species
SEM	Scanning electron microscope
SWNT	Single-walled carbon nanotube
TEM	Transmission electron microscope
THF	Tetrahydrofuran
ZnO	Zinc oxide

Chapter 1

Introduction

1.1 Nanoscience/Nanotoxicology

The prefix "nano" derives from Greek meaning "dwarf" [1]. Prior to the emergence of the nanoscience field in the recent few decades, most people may have only known "nano" in reference to the metric unit the "nanometer" (10^{-9} m). Scientists define nano-sized materials as any substance with at least one structural dimension that is 100 nm or less [2]. Hence, nano-substances encompass both natural and man-made materials. In nature, many complex systems are built from nanoscale components; some are benign and critical to the process of life, such as proteins, DNA, and cells, while others may cause harm, such as viruses, dust, or ash particles. Man-made nanoparticles (NPs) may be unintentional by-products of processes, such as vehicle exhaust, tobacco smoke, cooking, or construction, or ones made specifically for product enhancements, such as concealers in cosmetics, whitening ingredients, toothpaste, UV protectors in sun screen, antibacterial agents in sanitising products and apparels, and stain and wrinkle protectors in clothes [1, 3].

The interest in nanomaterials mainly stems from the discovery that nano-sized particles behave differently from their bulk form. Many particles are relatively inert in bulk form, but as the particle size decreases, the surface area increases exponentially and a higher proportion of atoms are exposed to the surface. This increases their surface and chemical reactivity and changes their electric, magnetic, optical, and mechanical properties, qualities that can be harnessed in all areas of science and production, including electronics, mechanical engineering,

chemistry, biology, and medicine. Furthermore, the discovery of the nano-world has led to interest not only in the construction of nano-scale materials but also in the understanding of existent systems. Elucidation of nature's complex systems has always been limited by the trailing development of human technology, but as science enters the nano-realm, researchers have begun to delve into nature's nano-world both to understand how the complex systems work as well as to mimic them. For example, scientists have identified that Lotus leaves are actually covered with parabolic-shaped projections that promote water to bead into droplets and roll off the surface, picking up dirt in the process. Companies have subsequently adapted this effect into self-cleaning surfaces that can be used on windshields, windows, solar panels, and any material that benefits from self-cleaning [4].

On the other hand, the small size is a cause for concern towards human health. Although humans are equipped with natural protective barriers and mechanisms—the skin, mucociliary escalator protecting the respiratory tract, membranes surrounding organs and cells, and macrophages eliminating foreign substances in the blood—nano-sized foreign substances can by-pass these defences and interfere with the normal processes of the cell. Various autoimmune diseases have been attributed to NPs, such as Crohn's, Parkinson's, and Alzheimer's disease. NPs may aggravate the pulmonary system and lead to asthma, bronchitis, or emphysema. Ones that enter the blood may contribute to atherosclerosis, vasoconstriction, or high blood pressure. Those that infiltrate cells may disrupt their processes and induce cancer. Because of these concerns, a part of nanoscience has emerged to understand what specific particles, characteristics, compositions, and behaviors lead to harmful effects.

1.2 Human exposure

With nanomaterials present in such wide-ranging sources, humans are easily, if not constantly, exposed to nanomaterials. Concern arises when the nanomaterials are particularly harmful or when the exposure levels are abnormally high. Foreign substances can enter humans predominantly via three routes: dermal contact, ingestion, and inhalation. The natural human body has its own protective barriers for each route; but when they are perturbed, the substances can enter the systemic circulation and damage less protected sites such as blood vessels, organs, the nervous system, and the brain.

1.2.1 Skin

The skin averages about 1.5 m^2 in area and comprises three layers (in descending order): the epidermis, dermis, and subcutaneous. The outermost layer, the epidermis, ranges between 0.05 mm and 1.5 mm in thickness and is further composed of five layers (in descending order): the stratum corneum, stratum lucidum, stratum granulosum, stratum spinosum, and stratum basale. The stratum corneum is the thickest layer and consists of dead cells that are shed every two weeks. The dermis, ranging between 0.3 mm and 3.0 mm in thickness, houses the hair follicles, oil and sweat glands, and smaller blood vessels and nerves, while the subcutaneous layer contains the fat, connective tissues, and larger blood vessels and nerves [5, 6].

Research on NPs penetrating through the skin suggested that NPs did not penetrate beyond the stratum corneum. In a study by Alvarez-Roman et al. [7], polystyrene NPs 20 and 200 nm in diameter were applied to porcine skin. The NPs were found to accumulate at follicular openings with increasing time and decreasing size; however, the NPs did not penetrate beyond the stratum corneum. In another study, Zvyagin et al. [8] applied 0.3 g of a commercial sunscreen containing ZnO NPs between 26–30 nm topically to human volunteers for 5 minutes. Accumulation was assessed immediately and after 4 and 24 hours after application. ZnO NPs were found mainly in the stratum corneum—in skin folds and hair follicles. The ZnO NPs within the hair follicle roots did not penetrate into neighboring cells or extracellular regions. In a third study, Pflucker et al. [9] applied 20 and 100 nm TiO_2 NPs at a concentration that was double the recommended amount for sunscreen application on the forearm of human volunteers for 6 hours. TiO_2 NPs were found only in the outermost layer of the stratum corneum. All these studies indicated that the skin was an effective barrier against NPs. However, the field of topical drug delivery has sought to deliver drugs *across* the skin barrier.

In topical drug delivery, researchers have focused on coating drugs with lipids to increase penetration across the thick layers of the stratum corneum. Attention has also centered on the role of hair follicles because they extended into the epidermis and were surrounded by cells and blood vessels. Lademann et al. [10] formulated hydrogels containing 320 nm NPs into particle and non-particle forms and assessed how long either remained inside hair follicles. Each gel was applied onto the calves of human volunteers and massaged for 3 minutes. Presence of the hydrogel in the non-particle form was only detected for up to 4 days, while the particle

form lasted until 10 days. The researchers concluded that surface structure affected retention. The same study further assessed the effects of massaging using porcine skin and found that massaging increased penetration depth. In a different study, Toll et al. [11] assessed the effect of NP size and the ”opening up” of hair follicles using skin surface stripping. 0.75, 1.5, 3, or 6.0 μm microspheres were massaged for 2 minutes onto skin samples from human volunteers. Without skin surface stripping, the NPs penetrated up to 25% of the follicles to a maximum depth of 1500 μm, while skin surface stripping yielded up to 55% penetration and a depth of 2300 μm. All four NPs penetrated the follicles, although the optimum size was 1.5 μm. These results indicated that NPs could indeed penetrate the skin barrier via hair follicles. For NPs that could manage to penetrate the follicles, they could then enter the systemic circulation via neighbouring cells and blood vessels.

1.2.2 Pulmonary system

The lungs have a surface area of about 140 m^2 and can be divided into two regions: ~2300 km of airways for air flow and ~300 million alveoli for gas exchange. The airways are covered by a thick layer of mucus and comprise the first line of defence against foreign particles. The mucus traps the particles and slowly moves them upwards along the airway where the particles are subsequently swallowed or expelled orally. The barrier in the alveolar region is much thinner with only 0.5 μm separating the alveoli from the underlying capillaries to allow for gas exchange, and it is protected by macrophages that can phagocytose foreign particles and transport themselves to the mucociliary escalator for excretion. [5, 12]

Pulmonary infiltration is of notable concern as humans survive by breathing. Air, and any foreign particles contained within, constantly flow through the lungs, and the thin alveolar barrier makes the alveoli particularly susceptible to penetration. In 1994, the International Commsion on Radiological Protection predicted the deposition of inhaled particles with diameters of 1–100 nm in the human lung using a mathematical model. Figure 1.1 graphically summarises the results. As the particle diameters decrease, they penetrate further into the pulmonary system. At diameters < 10 μm, the particles can enter the lungs, and at 10 nm, they have the highest deposition in the alveolar regions. With the thin alveolar barrier, such a high deposition rate significantly increases the probability of the particles penetrating the barrier and entering

the systemic circulations [2]. If, indeed, particles are too small and do not activate macrophage phagocytosis or the particle concentration is too high and the macrophages are unable to clear the particles in time, the particles can penetrate the interstitium and subsequently enter the circulatory system and distribute throughout the body, affecting the organs, the cardiovascular system, and numerous other regions.

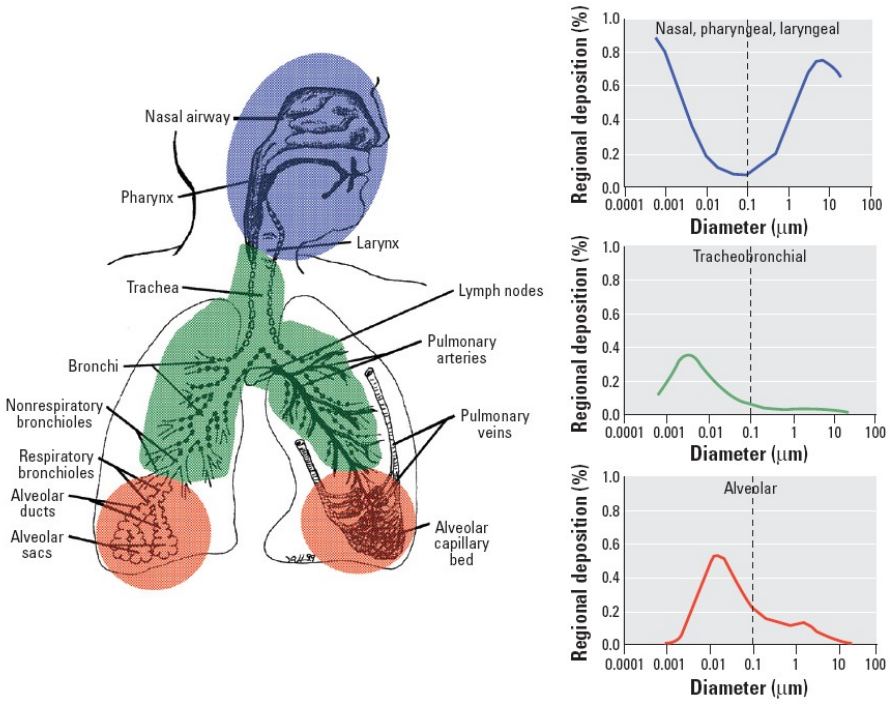

Figure 1.1: Particle deposition (diameters of 1–100 nm) based on a mathematical prediction model by the International Commission on Radiological Protection in 1994. Each graph on the right corresponded to the respectively coloured regions on the diagram on the left. At 10 μm, particles could enter the lung. As the diameters decreased, the particles penetrated deeper into the lungs. 10 nm yielded the greatest deposition potential in the deepest region of the lungs (alveolar). (Image from [2])

1.2.3 Intestinal tract

The intestinal tract is designed to absorb macromolecules. The small intestine is covered with villi and micro-villi which results in a total surface area of about 200 m^2. Intestinal uptake can occur via normal enterocytes or specialised enterocytes called M-cells [13], although a layer of mucus protects access to these cells. Research has shown that the smaller the particles, the

faster they permeate the mucosa into the enterocytes. When latex polystyrene spheres with diameters of 14 nm, 415 nm, and 1.09 μm were administered interluminally into the colon of rats, the 14 nm spheres had crossed the mucous layer and reached the outer mucosa layer within 2 minutes. The 415 nm spheres did not reach the mucosa until 30 minutes, while the 1.09 μm spheres remained within the mucous layer even after 30 minutes [14].

Penetration of intestinal enterocytes have also been shown to be size-dependent. When 50 nm, 300 nm, 1 μm, and 3 μm polystyrene spheres were orally administered to rats at 12.5 mg/kg for 10 days, 50 nm spheres were found in the intestinal enterocytes, villi, crypts, and intracellular junctions. They were also found throughout the body, in the lymph nodes, kidneys, liver, and spleen. 1 μm spheres were present in similar locations but at lower concentrations. The 3 μm spheres, however, were observed only in the intestinal enterocytes and no where else [15]. These results indicated that NPs could cross the epithelial membrane and enter either the lymphatic tissues to trigger the immune system or the capillaries and diffuse to the organs throughout the body.

1.3 Human macrophage cells

Macrophages are a critical component in the human immune system. They originate from the bone marrow as blood monocytes where they circulate in the blood and migrate to tissues to differentiate into macrophages (lung→alveolar macrophages, bone→osteoclasts, liver→Kupffer cells, central nervous system→microglial cells, connective tissue→histiocytes) [16]. Depending on the tissue type, their life span can range from 6 to > 60 days [17, 18]. It is unclear in the literature whether macrophages are able to proliferate. Some studies claim that macrophages are end-stage cells that cannot divide [18, 19], while others have found them to renew for a limited number of cycles [20, 21].

Macrophages are responsible for clearing tissues of waste, such as old or dead cells, and foreign materials, such as pathogens, bacteria, and viruses. When activated, they release various inflammatory markers, including interleukins, reactive oxygen species (ROS), and tumour necrosis factors, that trigger an immune response; additional macrophages and other immune cells are attracted to the site [16, 18, 22].

Because of their broad distribution in the body and their substantial role in foreign body

clearance, primary macrophages are used in the studies in the subsequent chapters. The direct isolation of monocytes from human buffy coats is a more realistic model as the macrophages are primary cells rather than immortalised cell lines.

1.3.1 Phagocytosis

One of the main characteristics of macrophages are their ability to phagocytose. Substances such as cells, cell fragments, bacteria, or particles that are greater than 1 μm in diameter are actively ingested. Once ingested, ROS, digestive enzymes, and acid are produced in contained compartments within the cell to destroy these substances, making macrophages a critical component in pathogen defence [23].

When removing cellular debris, little or no immune response is involved and macrophages remain unstimulated. However, when stress caused by injury or foreign substances triggers an immune response, macrophages become activated and converge at the site of inflammation. They begin their phagocytotic process while simultaneously releasing cytokines and pro-inflammatory mediators and presenting surface antigens that both promote the immune response further as well as attracting the migration of additional macrophages [16, 18, 22].

Macrophages can recognise foreign materials via two main methods. The first method involves certain motifs that are innate on the surface of the foreign material, such as carbohydrates, glycolipids, proteolipids, glycoproteins, and proteins. The second method involves opsonisation, whereby proteins, such as immunoglobulins and complements, are attached to the foreign material to promote phagocytosis [24, 25]. Once the receptors are activated, they begin to cluster and cross-link. This is believed to be the first step leading to the cytoskeletal rearrangement that is a key characteristic of phagocytosis, although the exact mechanisms involved in internalisation are still not fully understood [23, 26]. Depending on which process, the cell membrane either protrudes and surrounds the foreign material or the material "sinks" into the cell [25, 27, 28].

During the final stage of internalisation and the formation of the phagosome, membrane trafficking occurs in order to replenish the lost plasma membrane and to form the new phagosomal membrane. Once the phagosome is formed, it is trafficked through the cell via microtubules where it first merges with late endosomes and, ultimately, with lysosomes where di-

gestive enzymes, proteins, and peptides in an acidic environment destroy the foreign pathogen [24, 25, 27]

1.3.1.1 Frustrated phagocytosis

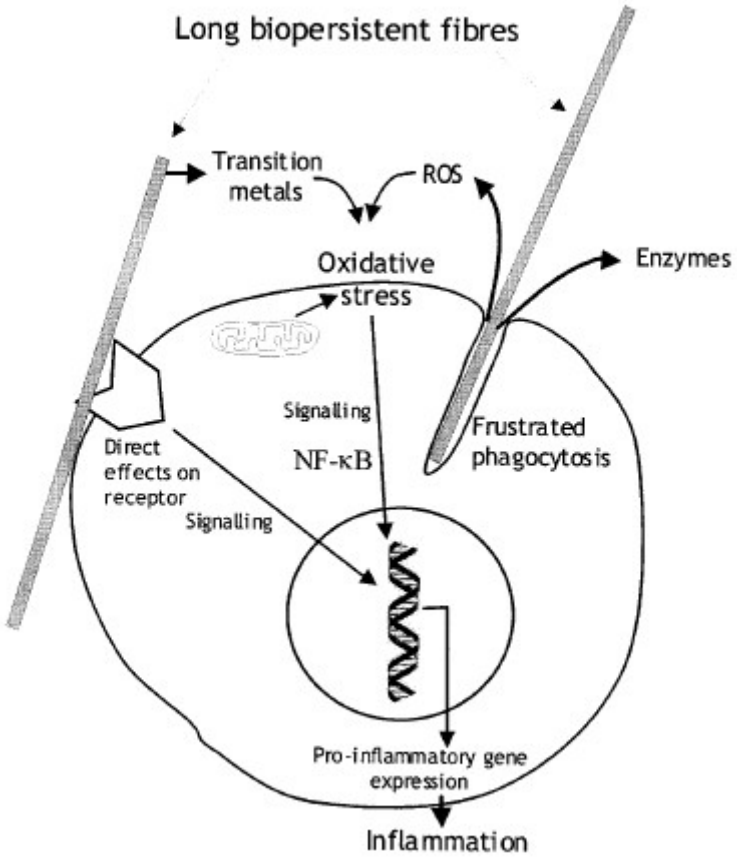

Figure 1.2: Possible proinflammatory cellular pathways caused by fibres. Specifically, frustrated phagocytosis prevents the cell membrane from sealing, which causes digestive enzymes to leak out and generate oxidative stress [12].

During fibre cytotoxicity research, an interesting phenomenon was observed in macrophage phagocytosis. When a fibre's length exceeded the diameter of the macrophage, the macrophage could not fully engulf the fibre within itself; rather, the fibre was seen to protrude from the macrophage plasma membrane. In a study by Dörger et al. [29], rat alveolar and peritoneal macrophages were treated with glass and wool fibres ranging from 1.8 to 76.9 μm in length (median length = 16.3-19.4 μm). Fibres > 20 μm were seen fully phagocytosed; however, 98% of the phagocytosed fibres were < 20 μm indicating that macrophages had difficulty phagocy-

tosing fibres > 20 μm in length. One possible reason might have been the availability of plasma membrane.

Canon et al. [30] assessed the phagocytic capacity of murine bone marrow-derived macrophage cells with polystyrene beads between 13 to > 30 μm in diameter. Beads up to 24 μm were found fully phagocytosed. They determined that phagocytosing macrophages reached a surface area of 3,080 μm2, much higher than the reported surface area of 825 μm2 for resting macrophages. This implicated the possibility of internal membranes being recruited for phagocytosis. To test this observation, macrophages were treated with sucrose to osmotically overload the lysosomes, and phagocytic capacity did indeed decrease.

These results indicated that the macrophage phagocytotic potential could be limited by the available plasma membrane resources. When the macrophages attempted to phagocytose particles greater than its capacity, the phenomenon termed "frustrated phagocytosis" occured. This was implicated in fibre-induced cytotoxicity. When a macrophage failed to fully engulf the fibre, the macrophage remained activated and would attract more macrophages. This, in turn, could lead to increased lung burden. Furthermore, with incomplete phagocytosis, the phagosome could not be fully sealed. As a result, oxidants and enzymes could leak out from the macrophage into the surrounding area and lead to further cytotoxicity (Figure 1.2).

1.3.2 Passive uptake

Cells can also internalise substances passively. Gases, molecules, and inorganic ions are transported by way of a concentration gradient whereby molecules move from areas of higher concentration to lower concentration. As the cell membrane is semi-permeable, oxygen, carbon dioxide, water, and other small molecules can move across the membrane by diffusion [31]. Additionally, channels exist throughout the cell membrane, although movements across are limited by size restrictions, conformation matching, or other protein(s) binding to the channel in order to open/close the channel [32, 33]. Despite these various exclusions, NPs can lead to subsequent cytotoxic effects if they are small enough or shaped similary to the molecules or proteins that are designed to cross membranes or control ion channels.

1.3.3 Cell death

Cell death occurs via two main processes: apoptosis and necrosis (Figure 1.3). Apoptosis, often termed "programmed cell death," is a form of cell suicide triggered by an internal clock or external agents that ultimately leads to nuclear (karyorrhexis) and DNA fragmentation. Morphologically, cells shrink, the nuclei become condensed (pyknosis) leading to margination of chromatin (capping), and apoptotic bodies are formed from the nuclear fragmentation. Necrosis is a more passive form of cell death that can result from environmental stress, such as nutrient deficiency, ATP depletion, and physical damage, and leads to inflammation caused by the release of cell contents and pro-inflammatory molecules. Cells and organelles typically swell, the cytoplasm becomes vacuolated, and the plasma membrane breaks down.

If apoptotic cells are not phagocytosed due to reasons such as insufficient macrophages, excessive apoptosis overwhelming available macrophages, or inability for macrophages to recognise apoptotic cells, secondary necrosis can occur. The plasma membrane of the unphagocytosed cell will subsequently break down and release the intracellular contents that will trigger an inflammatory response [34].

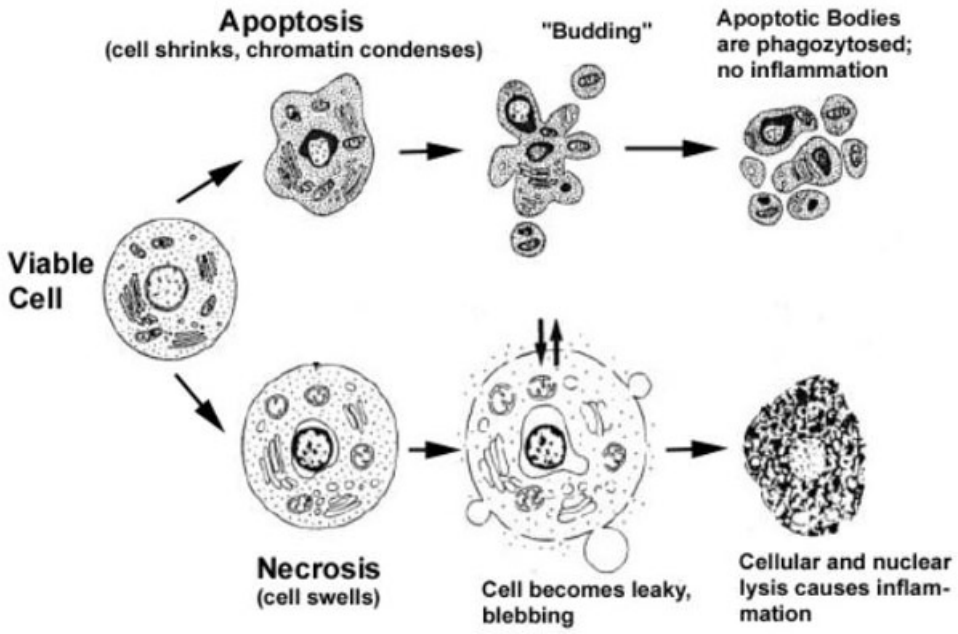

Figure 1.3: Morphological and chemical changes in apoptosis and necrosis [35].

1.4 Challenges of characterising the effects of NPs

1.4.1 Cell viability assays

	Stain/dye	Action	CB	SWNT	C60
Neutral red	Lysosomal uptake into live cells	Lysosomal membrane	F	F	D
MTT	Tetrazolium conversion to insoluble purple formazan in live cells	Mitochondrial metabolism	F	D	D
CellTiter 96® AQueous One	MTS conversion to soluble purple formazan in live cells	Cell metabolism	C	A	A
alamar Blue	Resazurin reduction to red fluorescent dye resorufin by live cells	Cell metabolism	F	D	A
CellTiter-Blue®	Kit form of alamar Blue	Cell metabolism	D	C	A
CytoTox One™ Homogeneous Membrane Integrity	LDH enzymatically reduces resazurin into resorufin	Cell metabolism	F	F	B

A – Assay works well; data reliable.
B – Assay works well; significant difference against no cell control ($p < 0.05$) < 10%.
C – Assay works; significant difference against no cell control ($p < 0.05$) from 10% to < 20%.
D – Assay works poorly; significant difference against no cell control ($p < 0.05$) from 20% to < 50%.
F – Assay fails; significant difference against no cell control ($p < 0.05$) $\geq$ 50%.

Table 1.1: Description of various cell viability assays and their graded validity in measuring CB, SWNT, and C60 toxicity (synthesised from [36])

Various studies have found that some types of NPs (e.g. carbon-based NPs) can interfere with spectrophotometric assay dyes. Monteiro-Riviere et al. [36] recently graded the validity of several assays in assessing the toxicity of the carbon NPs carbon black (CB), single-walled carbon nanotubes (SWNTs), and C60. Table 1.1 listed some of the assay dyes that were assessed using human epithelial keratinocytes (HEK). Two different set-ups were performed for each assay dye: without and with cells present. Without cell presence assessed the interaction between the NPs and the assay dyes only, while the presence of cells assessed the interaction of the NPs after the assay dyes had first interacted with the cells. The difference between these

two set-ups determined the effects that the NPs had on the assay dyes.

Of specific interest were the NR and MTT assays as they were used to assess the toxicity of the NPs in the following chapters. The authors found that the NR dye was readily adsorbed by the carbon NPs which yielded falsely positive toxicity. It seemed that a decrease in particle size led to an increase in surface area and reactive groups, which resulted in increased dye adsorption. For the MTT, CB and SWNT by themselves could convert the tetrazolium into formazan without the presence of cells which also led to a falsely positive toxicity. With NPs affecting many of the standard assays in different ways, the authors concluded that several different spectrophotometric assays should be used in conjunction with imaging to profile NP toxicity.

The following assays are used in this study:

- **Neutral Red (NR)** is a dye made of basic red 5 and toluene red that is internalised into the lysosomes of viable cells only [37].
- **MTT**, or 3-[4,5-dimethylthiazol-2-yl]-2,5-diphenyl tetrazolium bromide, measures the enzymatic conversion of MTT to purple formazan crystals by dehydrogenase enzymes in viable cells [38].
- **Lactate Dehydrogenase (LDH)** is an enzyme present in the cytoplasm of all cells that is released upon damage to the plasma membrane. The presence of LDH will convert the dye tetrazolium salt INT into formazan for the spectrophotometer to detect [39].
- **Live dead** is an assay employing the confocal microscope. Cells are treated with fluorescent markers Hoechst 33358 and propidium iodide (PI) which stain the nuclei of all cells and non-viable cells, respectively. Random frames for each treatment are taken and the number of living and dead cells counted individually.

1.4.2 Imaging

Electron microscopes are ideal imaging tools as electrons have shorter wavelengths than photons, which allow for detailed imaging to as low as 0.1 nm [40], but there are certain limitations depending on which type of microscope is used. The following sections briefly describe the microscopes and techniques used in this study.

1.4.2.1 Transmission electron microscope (TEM)

The TEM operates very similarly to the light microscope. Instead of light, electrons are emitted through a vacuum and concentrated into a beam by way of electromagnetic lenses and yields a resolving power—the point where two adjacent objects are still distinguishable—of 0.1 nm or lower. Depending on the density of the specimen, electrons either travel through and are projected onto a fluorescent screen or are scattered away from the specimen. Because electrons are easily scattered, samples are usually between 20 to 150 nm in thickness [41, 42, 43]. A special protocol is employed to prepare biological samples for the TEM. Treated cells are first chemically fixed to stabilise and preserve the cell structures before all water is removed and embedding resin allowed to infiltrate the cells [44]. Once set, the embedded sample is cut into thin sections with a diamond knife on an ultramicrotome and the sections placed onto grids for imaging. This technique is limited by the required thinness and preservation of the cell samples.

1.4.2.2 Scanning electron microscope (SEM)

The SEM, like the TEM, uses an electron beam condensed by electromagnetic lenses; but rather than penetrating the sample, the electron beam is scanned across the sample surface and the secondary electrons (generated from inelastic scattering—the release of electrons from the atom surface) produced are detected and amplified by detectors and transferred to a cathode ray tube screen for visualisation. A topographical image is produced with a resolution of 1 nm. Sample preparation is not as complex as the TEM; however, all volatile compounds (e.g. water) must be removed or immobilised and a thin electron-conducting layer sputter coated onto non-conducting samples to prevent image disruptions caused by electrons collecting onto the sample (*charging*) [41, 43]. Details may also be lost if they are finer than the thickness of the sputter-coated layer.

1.4.2.3 Electron dispersive x-ray (EDX) analysis

EDX is a technique that can quantitatively or qualitatively determine the elemental composition of a sample based on emitted x-rays. The technique can be used in either the TEM or SEM. When electrons from the electron beam hits the sample, x-rays are released from the atoms

in the sample. Each atomic species releases a characteristic x-ray which the EDX detects in order to generate a spectrum that identifies the type and frequency of the elements present in the sample. As with the SEM, all non-conducting samples require a thin electron-conducting layer to prevent charging. Carbon is chosen as it is at the low end of the spectrum and far from the elements of interest [43, 45].

1.4.2.4 Confocal microscopy

With the confocal microscope, sample thickness is less restricted and cells can be imaged alive and whole without chemical fixation, freeze drying, or any significant manipulation other than the addition of fluorescent stains. The following fluorescent markers are used in this study:

- **Hoechst 33358** diffuses through the plasma membrane of both viable and non-viable cells and binds to the lesser curvature of DNA. The stain is excitable by ultraviolet light usually captured between 400–480 nm by a mercury vapor lamp or an argon laser at 351 or 364 nm to generate a blue emitted fluorescence [46].

- **Propidium Iodide (PI)** enters non-viable cells through their compromised plasma membrane and bind to nucleic acids. It is excitable by a mercury vapor lamp or the argon laser at 488 nm to generate a red emitted fluorescence [46].

- **FM4-64** can be used to label the plasma membrane as well as study endocytosis. The dye inserts into the outer bilayer of the plasma membrane and fluoresces red. It is excitable at 561 or 568 nm with an emission maximum around 630 nm. The dye is a plasma membrane marker and can be tracked as it is internalised into the cell [46].

- **Calcein AM** permeates the cell membrane as a molecule. Intracellular esterases of viable cells hydrolyse the lipophilic acetomethoxyester (AM) group allowing calcium ions to bind to the calcein and generate a green fluorescence. It is excitable by the argon laser at 488 nm emitting at 530 nm [46].

In a confocal microscope, the light source is derived from one or multiple laser(s). The light is focused onto a point in the sample and scanned across the sample. The reflected light from the plane-of-focus is directed through a pinhole and into a detector. The pinhole blocks light

reflected from outside the plane-of-focus which improves the resolution of the plane of interest. Because thin optical sections are scanned each time, multiple sections (Z-plane stacks) can be digitally assembled to create an average or maximum image projection [47]. The microscope can be modified for live cell imaging over extended time periods by housing either the entire microscope or only the culture dish at 37°C and providing a constant supply of oxygen and carbon dioxide. One limitation is light diffraction, where the edges become undefined and hazy, causing the boundaries of objects smaller than the diffraction limit to diffuse, merge, and appear bigger (Figure 1.4); as a result, the XY axes and Z axis resolutions are approximately 200 nm and 600 nm, respectively [48]. This limits the type of NP visible in the microscope. Certain

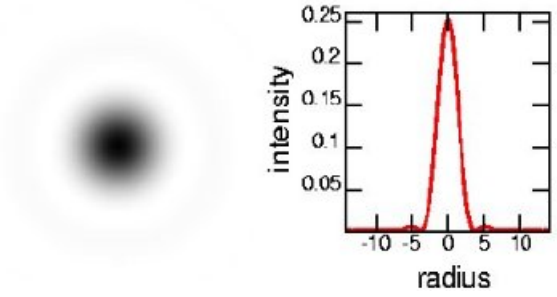

Figure 1.4: Example of light diffraction with a graph of how light intensity is affected in relation to the radius [48].

manipulations can be employed, such as using reflectance if the NP is reflective, exciting the NP if it can be excited to emit fluoresence, or binding fluorescent proteins to the NP to help it fluoresce; however, the low resolution means only large aggregates can be seen rather than individual NPs.

1.5 Scope of project

For this PhD, three different NPs were chosen to assess their toxic potential using similar experimental methods. At the start of this project, the paper by Oberdorster et al. [49] reporting the toxic potential of C60 had only been released for about two years. There was an intense interest in determining whether other carbon-based nanomaterials were toxic; consequently, the carbon nanotubes (CNTs) multi-walled carbon nanotubes (MWNTs) and SWNTs were chosen for this

project. The third NP assessed were the ZnO nanopowders. Although the dimensions of ZnO nanowires would make them better comparisons to the CNTs, ZnO nanopowders constituted the nanowires; understanding how the nanopowders interacted with cells could shed light into later assessments of the nanowires themselves.

Chapter 2

MWNT

2.1 Introduction

MWNTs are stiff, tubular structures consisting of concentric layers of cylindrical graphene sheets. Their diameters can range from 1.4 to 100 nm with lengths $\geq$ 1 μm. MWNTs can have very high aspect ratios and surface area with highly ordered structures and mechanical strength. They also have high electrical and thermal conductivity and can be either metallic or semi-conducting depending on their structure. These features make them ideal candidates for many applications. MWNTs have been formed into "super-strong" fibres that can be used in textiles and electrodes [50]. They can improve the structural and electrical properties of composites such as epoxy which are used for structural applications in aerospace, automotive, and marine industries [51, 52]. Microcatheters containing MWNTs have been developed to improve flexibility and shape retention after intravascular use and to prevent blood coagulation and clot formation [53]. Scaffolds can be created from MWNTs for cell growth in tissue engineering [54]. With such wide-ranging potential, attention has become focused on the possible negative effects of MWNTs. Table 2.1 summarised the details of some of the papers discussed in this chapter.

Many papers were published on the potential health effects of MWNTs, but results were often conflicting. Some studies found that MWNTs decreased cell viability:

- Bottini et al. [55] assessed the toxicity of pristine and oxidised (derived from refluxing the pristine MWNTs in concentrated nitric acid) MWNTs on human tumour T lympho-

Table 2.1: Summary of experimental details of some of the MWNT papers discussed in chapter.

	Materials	Size	Impurity	Dispersant	Model	Conc	Time	Assay	Results
Bottini	Pristine	L: 1-5 um D: 20-40 nm	< 5%	Water	Human tumour T lymphocyte (Jurkat)	40, 400 ug/mL		Trypan Blue	Tox: Oxidised > Pristine (dose and time dependent)
	Oxidised	shorter straighter						Annexin V	death via apoptosis
Hirano		D: 67 nm	< 0.2 % Fe	10% Pluronic F108	Mouse macrophage (J774.1)	10-1000 ug/mL		WST-8	Tox: Dose and time dependent increase
Simon-Deckers	Unpurified /Purified Long	L: 1.5 um D: 44 nm	4.24% vs 0.08% Fe	Arabic gum	Human type II lung epithelial (A549)	0.25-100 ug/mL	48 hrs	LDH, XTT, MTT	Tox: dose dependent, MTT > XTT > LDH, Fe and length no effect
	Unpurified Short	L: 972 nm D: 26 nm	4.24% Fe					TEM	Found in cytoplasm
De Nicola		L: 5-9 um D: 110-170 nm	0.1% Fe	Culture medium	Jurkat	25, 100 ug/mL	24, 48, 72 hrs	Hoechst, PI	Dose and time dependent apoptosis & secondary necrosis; no increase in primary necrosis
Ding			Fe	Culture medium	Human skin fibroblasts (HSF42)	0.06, 0.6 ug/mL	24, 48 hrs	GeneChip system;	Genes expressed: 0.06ug/mL--growth and metabolic reduction, protein degradation; 0.6ug/mL--apoptosis, immune and inflammatory response
								YO-PRO1, PI	Dose-dependent apoptosis & necrosis
Monteiro-Riviere			Fe	Culture medium	Human epithelial keratinocytes (HEK)	0.1, 0.2, 0.4 ug/mL	up to 24 hrs	IL-8 CytoSet kit; TEM	Dose and time dependent increase of IL-8; found in vacuoles, cytoplasm, close to nuclear, pierce plasma membrane
Zhu	Purified MWNTs		0%	Culture medium	Mouse embryonic stem	0, 5, 100 ug/mL	2, 4 hrs	Western blot	p53 activation
Kateb		L: 200-400 nm D: 20 nm	0%	1% Pluronic F108	Mouse microglial (BV2) & glioma (GL261)	80 ug/mL	15, 24, 48 hrs	Cell adherence	No statistical differences in cell number with and without MWNTs
Pulskamp	NT2	D: 10-20 nm	5%	Culture medium	Rat alveolar macrophage (NR8383)	5, 10, 50, 100 ug/mL	24-96 hrs	MTT, WST-1, PI	MTT: up to 70% death, WST and PI: no significant death
	NT3	D: 30-50 nm						TMRE	Dose dependent loss of mitochondria function

	Materials	Size	Impurity	Dispersant	Model	Conc	Time	Assay	Results
Grabins		D: 10 nm	3.75% Fe	Culture medium	Mouse keratinocyte	5, 10, 25, 50 ug/mL	24 hrs	DCHF-DA	Dose-dependent ROS generation, 3-7 fold over Control
Schrand		L: < 10s um D: 9-30 nm	0.49%	Culture medium	Rat macrophage (NR8383) and neuroblastoma	25, 50, 100 ug/mL	24 hrs	DCHF-DA	ROS correlated to amount of Fe; macrophages generated up to 5x more than neuroblastoma
Poland	NTtang1	L: 15±0.5 um D: 15±5 nm	0.003%	Bovine serum albumin	Female C57BL/6 mice	50 ug/mice	24 hrs or 7 days	Histology	NTlong: generated polymorphonuclear leukocytes and granulomas; NTtang: no inflammation
	NTtang2	L: 10±0.32 um D: 15±5 nm	0.002%						
	NTlong1	L: 85±2 um D: 13 nm	0.001%						
	NTlong2	L: 165±5 um D: <56 nm	0.005%						
Muller2005	Unground	L: 5.9±0.05 um D: 9.7±2.1 nm	2.2%	1% Tween 80	Sprague-Dawley rats; peritoneal macrophage	0.5, 2 or 5 mg/rat; 2-, 50, 100 ug/mL	60 days; 6, 24 hrs	Histology; LDH, TNF-a	In vivo: unground-granulomas, ground-rapid clearance; in vitro: ground more toxic than unground
	Ground	L: 0.7±0.07 um D: 11.3±3.9 nm	2.0%						
Lacerda		L: 0.5-2 um D: 20-30 nm	8-10%	Functionalise: diethylentriaminepentaacetic (DTPA) dianhydride	Male nude rats	300, 600 ug/rat	5 min, 30 min, 6 hrs, 24 hrs	Radioactive computed tomography, TEM	60sec: enter systemic circulation, 6hrs: accumulate in kidney and bladder; 24hrs: complete clearance
Raffa	Long	L: ~2 um D: 20-40 nm	3%	1% Pluronic F127	Mouse hippocampal (HN9.10e)	5, 15 ug/mL	1, 12 hrs	Lysotracker probe	Lysosomal uptake greater for short NTs
	Short	L: ~0.3 um D: 35-40 nm	1%						
Sato		L: 220, 825 nm D: 20-40 nm	20%	Carboxyl	Wistar rats	0.1 mg/rat	1, 4 wks	TEM	220nm: phagocytes, lysosomes; 825nm: cytoplasm
Brown		L: < 50 um D: 20-100 nm	5%	Culture medium	Primary human peripheral blood mononuclear cells	15.6-62.5 ug/mL	4 hrs	Light microscopy, TNF-a kit, Cytochrome c reduction	Frustrated phagocytosis, TNF-a and superoxide (O2-) production
Muller2008b		L: 0.7±0.07 um D: 11.3±3.9 nm	2.0%	Culture medium	Rat lung epithelial (RLE) & human breast carcinoma (MCF-7)	10, 25, 50, 100, 125 ug/mL	RLE: 3hrs, MCF-7: 6 hrs	Micronuclei assay with fluorescent in situ hybridisation	Presence of aneugenicity (chromoson loss) and clastogenicity (DNA damage)

cytes (Jurkat) using the Trypan Blue assay. 40 or 400 μg/mL of each were treated for up to 5 days. Both samples caused dose and time dependent toxicity. The oxidised MWNTs were found to be more toxic than the pristine with the highest concentration (400 μg/mL) at 5 days causing > 80% cell death for the oxidised compared to only 35% for the pristine.

- Hirano et al. [56] assessed 10-1000 μg/mL of MWNTs on mouse macrophages (J774.1) for up to 32 hours and similarly found a dose and time dependent toxicity with the WST-8 assay, a modified MTT assay. Cell death reached close to 90% at 100 μg/mL after 32 hours. However, cell death reversed after the 100 μg/mL concentration mark, possibly caused by the observed MWNT aggregation at the higher concentrations. As the MWNTs aggregated, less surface area was exposed to interact with the cells.

- Simon-Deckers et al. [57] compared the toxicity of three different MWNTs—long and short unpurified MWNTs and short purified (via heat treatment) MWNTs—on human type II lung epithelial cells (A549) and found that length and contamination had no effect on the observed dose dependent toxicity. 0.25–100 μg/mL of each were treated for 48 hours, and three assays were used to assess their effects: LDH, XTT (3-[1-(phenylaminocarbonyl)-3,4-tetrazolium]-bis(4-methoxy-6-nitro)benzene-sulfonic acid hydrate), and MTT. Maximum toxic effect was observed with the MTT assay with cell death reaching 50% for the lowest concentration (0.25 μg/mL), while the XTT assay yielded only 10% death at the highest concentration (100 μg/mL). The LDH assay detected 40% death for the highest concentration.

- De Nicola et al. [58] determined that MWNTs induced apoptosis in a dose and time dependent manner. Jurkat cells were treated with 25 or 100 μg/mL of MWNTs for up to 3 days. Hoechst 33358 was used to stain the nuclei, and apoptosis was identified as cells containing fragmented nuclei.

Despite the different MWNT materials, cell lines, concentrations, time points, and assays, all four studies observed a dose and time dependent toxic effect. This confirmed that MWNTs could indeed cause cell death. Studies went further and assessed the mechanisms affected by MWNTs and found that MWNTs up-regulated genes associated with cell cycle regulation, inflammation, and apoptosis:

- Ding et al. [59] used an Affymetrix high-throughput analysis automated GeneChip system to profile genes expressed by human skin fibroblast cells treated with 0.06 and 0.6 ug/mL of MWNTs for 24 and 48 hours. The authors found that different genes were expressed for the two different doses. For the low dose, the genes expressed caused a reduction in cell growth and metabolism and an acceleration in protein degradation. For the high dose, several apoptotic genes were up-regulated, and a significant number of immune and inflammatory response genes were over-expressed.

- Monteiro-Riviere et al. [60] directly assessed for interleukin (IL) 8, a proinflammatory cytokine marker, using an IL-8 cytoset kit. HEK cells were treated with 0.1–0.4 μg/mL of MWNTs for up to 24 hours, and a dose and time dependent increase of IL-8 was observed.

- Zhu et al. [61] detected a dose and time dependent p53 activation, indicating DNA damage, with Western blot on mouse embryonic stem cells treated with 5 and 100 μg/mL of MWNTs purified in concentrated HCl for 2 and 4 hours. The p53 protein was responsible for arresting the cell cycle to allow cells to repair any DNA damage.

These three studies further implicated the toxic role of MWNTs in cells. Genes, markers, and proteins associated with cell damage/repair and inflammation were induced by MWNTs. However, despite the toxic results from the studies above, some studies found that MWNTs caused minimal or no decrease of cell viability:

- Kateb et al. [62] treated 80 μg/mL of MWNTs for 15–48 hours on two mouse cell lines—microglial (BV2) and glioma (GL261). Ten frames for each sample were taken with a two-photon inverted confocal microscope and the number of adherent cells counted to determine cell viability. No statistically significant differences in adherent cells between the control and MWNT-treated cells were observed.

- Pulskamp et al. [63] treated 5–100 μg/mL of MWNTs for 24–96 hours on rat alveolar macrophage (NR8383) cells. Three different assays were used: MTT, WST-1, and PI. The MTT detected up to 70% cell death at the highest concentration and longest time point. As MTT could inflate the toxic response,the WST-1 and PI were used for verification. The WST-1, an assay similar to the MTT, did not detect any cell death. For the

PI, the dye only entered cells with compromised membrances; consequently, cells were treated with PI and FACS analysis used to differentiate between living and dead cells. No significant differences were detected between control and MWNT-treated cells. As both the WST-1 and PI indicated no cytotoxicity, the authors concluded the MWNTs were not toxic.

These two studies used different MWNT materials, cell lines, concentrations, time points, and assays compared to the previous six studies and concluded very different results. With few consistent experimental parameters, the reason(s) for the differing results were difficult to identify. The contradicting results from these eight studies highlight the difficulty in determining the effects of MWNTs. Some of the reasons could be attributed to the MWNT materials themselves, such as the metal content, structural defects, length, and surface chemistry.

Metal content. The metal catalyst (e.g. iron, nickel) used to synthesise CNTs have been found to cause oxidative stress related toxicity, possibly via the Fenton reaction. Two studies found that ROS generation corresponded to the amount of iron available in carbon nanotubes. Grabinski et al. [64] assessed the ROS generation of mouse keratinocytes treated with 5–50μg/mL of MWNTs with 3.75 wt% Fe for 24 hours using the fluorescent probe 20,70-dichlorohydrofluorescein diacetate (DCHF-DA). The DCHF-DA probe bound to ROS and generated fluorescence which would be detected by a microplate reader. They found that the MWNTs caused a dose-dependent increase in ROS generation with a total of 3–7 fold increase over the control. Schrand et al. [65] used the same assay on rat macrophage and neuroblastoma cells treated with 25–100 μg/mL of MWNTs containing 0.49 wt% Fe for 24 hours and similarly found that ROS generation correlated with the amount of Fe in the MWNTs. They also noticed a difference between the two cell lines with macrophages (25 fold increase over control) generating five times more ROS than the neuroblastoma (5 fold increase) cells. If the two studies were compared using the same concentration (25 μg/mL), the MWNTs with 3.75 wt% Fe actually generated less ROS than the MWNTs with 0.49 wt% on macrophage cells. This could be due to the difference in cell line as well as the MWNTs themselves as different characteristics could affect the bioavailability of the Fe.

As ROS were destructive to cells, studies assessed the effect of impurities on cells. Shvedova et al. [66] detected the presence of OH^- free radicals using a technique called electron spin res-

onance spin trapping and found that SWNTs containing 30 wt% Fe caused a dose-dependent decrease in the antioxidants vitamin E and glutathione (GSH) in human keratinocyte (HaCaT) cells treated at 60–240 μg/mL for 18 hours. The addition of the Fe^{3+} chelator, deferoxamine, significantly reduced the cytotoxic effect of SWNTs by up to 30%. Pulskamp et al. [63] determined that MWNTs containing 5 wt% Fe and Ni generated up to a 4 fold increase of ROS in NR8383 cells treated at 5–100 μg/mL for 24 hours. As ROS could affect cell organelles, the authors assessed for mitochondrial damage as mitochondria were important in many cell functions. They observed a dose-dependent (up to 40%) destruction of mitochondrial membrane in NR8383 cells treated with MWNTs containing 5 wt% Fe and Ni. Although the study by Shvedova et al. used SWNTs, these two studies established that the observed ROS generation from the CNTs depleted antioxidants, damaged mitochondria, and led to cell death.

Structural defects. Defects on the MWNT structure could cause inflammation and genotoxic (DNA damage resulting in mutations or cancer) effects. One such defect was the Stone-Wales defect where pentagon-heptagon pairs replaced the normal hexagonal structures. Another was the exposed ends which might be caused by breakages or uncapped ends. Two different papers used the same set of MWNT samples to assess the impact of structural defects.

MWNTs were first ground to introduce defects by an agate ball mill ($MWNT_g$) and were subsequently heated to either 600°C ($MWNT_{g600}$) to eliminate any molecules adsorbed onto the MWNT surface or 2400°C ($MWNT_{g2400}$) to remove any metal contaminants. One set of MWNTs treated at 2400°C was also ground ($MWNT_{2400g}$) to prepare a fourth sample consisting of damaged MWNTs without metal contaminants. Table 2.2 listed the characteristics of the different MWNT samples.

The MWNT samples were dispersed in 1% Tween 80 and injected directly into the lungs of

	MWNT	$MWNT_g$	$MWNT_{g600}$	$MWNT_{g2400}$	$MWNT_{2400g}$
Length (μm)	5.9 ± 0.05		0.7 ± 0.07		
Diameter (nm)	9.7 ± 2.1		11.3 ± 3.9		
Surface area (m^2/g)	213	299	274	190	240
I_D/I_G	1.05 ± 0.05	1.16 ± 0.08	1.10 ± 0.10	0.58 ± 0.14	0.93 ± 0.09
Metal content (%)	2.20	2.94	3.3	0.37	0.21

Table 2.2: A summary of the characterisation details for the MWNTs that were heat treated and ground for the studies by Fenoglio et al. [67] and Muller et al. 2008a [68].

female Wistar rats at 500 μL/rat for 3 or 60 days. After MWNT treatment, the bronchoalveolar lavage fluid was extracted and the production of LDH and proinflammatory factors IL-1β and TNF-α measured to determine acute toxicity. $MWNT_g$ caused the greatest acute toxicity. As both the $MWNT_{g600}$ and $MWNT_{g2400}$ samples decreased LDH, IL-1β, and TNF-α production, acute toxicity appeared to correlate with heat treatment rather than metal content. The MWNT samples were also treated on rat lung epithelial cells and genotoxicity assessed by the prevalence of micronuclei. Similar results were observed: $MWNT_g$ caused the greatest genotoxic response and genotoxicity was better correlated with heat treatment rather than metal content [68]. Interestingly, no ROS production was detected; instead, the MWNTs exhibited free radical scavenging abilities with the ability affected mainly be the amount of defects present [67]. In general, $MWNT_g$, the sample with the most defects, caused the greatest toxicity while $MWNT_{g2400}$, the sample with the least defects, caused the least toxicity.

Length. With length, the toxicology paradigm had established fibres < 3 μm wide, > 20 μm long, and biopersistent as hazardous. MWNTs often fitted into this paradigm, and Poland et al. [69] sought to confirm if MWNTs could cause similar toxicological responses as hazardous fibres. Four different MWNT samples were injected into the abdominal cavity of mice at 50 μg per mice for 1 or 7 days. Two samples contained long straight MWNTs > 20 μm (11% and 76%) while two samples contained short tangled MWNTs (< 20 μm). Histological sections revealed that the MWNT samples with > 20 μm fibres generated polymorphonuclear leukocytes and granulomas, characteristics seen in inflammation when macrophages cannot effectively phagocytose and clear the fibres from the lung airway. These results suggested that long MWNTs could indeed behave similarly to hazardous fibres.

Two studies assessed the impact of length on toxicity. Muller et al. 2005 [70] ground MWNTs to generate two samples of differing length: 5.9 ± 0.05 μm and 0.7 ± 0.07 μm. *In vivo*, rats were treated with 0.5–5 mg/animal of either sample for 60 days. The unground MWNTs formed large aggregates that lodged in airways resulting in artificial granulomas, while grinding the MWNTs led to more effective dispersion in the airways and more rapid clearance, although a substantial amount (36%) still remained in the lungs. *In vitro*, the ground MWNTs caused significant dose-dependent increase in LDH and TNF-α production, while the long MWNTs did not. As the unground MWNTs formed large aggregates that floated at the top of the cul-

ture medium, the authors hypothesised that less of the unground MWNTs were exposed to the cells to cause any toxicity. Contrarily, Simon-deckers et al. [57] found no cytotoxic difference between MWNTs averaging at 1.5 μm and 0.97 μm long. Arabic gum was used to disperse the MWNTs and prevent aggregation suggesting that aggregation might be significant in determining MWNT toxicity.

These studies indicated that length indeed affected the toxic potential of MWNTs, although no definite conclusions could be drawn as results were affected by experimental method (*in vivo* versus *in vitro*) or aggregation.

Surface chemistry. Pristine CNTs were hydrophobic and tended to agglomerate due to van der Waal forces. Studies used a variety of organic solvents (e.g. tetrahydrofuran (THF) and DMSO), and detergents (e.g. SDS, 1% Pluronic, Triton X-100, and Tween 80) to help disperse the CNTs; however, the solvents and detergents themselves were inherently toxic to cells. Although the concentration used was very low, possible cytotoxic effects could still exist. As an alternative to dispersants, MWNTs were functionalised to improve dispersion. Lacerda et al. [71] functionalised MWNTs with diethylentriaminepentaacetic (DTPA) dianhydride using the 1,3 dipolar cycloaddition reaction and significantly unbundled and individualised the MWNTs. The functionalised MWNTs were radio-labelled, and 300 μg/mice were injected into the tail vein. Using a microSingle Photon Emission Tomography computed tomography scanner, the tissue distribution was traced. The functionalised MWNTs entered the systemic circulation within 60 seconds. After 30 minutes, most were localized in the kidneys and bladder, and by 6 hours, almost all the functionalised MWNTs were eliminated via renal excretion. A separate experiment using histological sections of Wistar rats injected with 600 μg/mice of functionalised and unfunctionalised MWNTs was performed, and it was found the unfunctionalised MWNTs accumulated in the lungs and liver after 24 hours while the functionalised MWNTs had no tissue accumulation. This study implicated that functionalised MWNTs, and potentially unbundled and individualised MWNTs, could significantly alter their systemic behaviour and decrease their toxicity.

Clearly, metal content, structural defects, length, and surface chemistry could affect the health effects of MWNTs which made the unambiguous determination of the toxic effects of

MWNTs a challenge. Such contradictory results highlighted the need for alternative ways to study MWNT uptake and cytotoxic effects in cells. Whilst traditional cell viability assays were commonly used for large throughput, they could be prone to false positives; and most assays did not discriminate between the routes of cell death. In contrast, microscopy could provide direct estimates of cell viability with the advantage of assessing CNT presence within the cell.

In previous work, lysosomal uptake of short (average length ~0.3 μm) and long MWNTs (average length ~2 μm) were compared in mouse hippocampal cells (HN9.10e) using a fluorescent Lysotracker probe and fluorescence microscopy. Internalisation of short MWNTs was greater than the long MWNTs. The uptake mechanism was also investigated by employing two different methods of inhibiting active uptake: the endocytosis inhibitor sodium azide and refrigerating the cells at 4°C. Interestingly, results remained the same, indicating that the MWNTs were internalised passively [72]. Two studies using TEM, Monteiro-Riviere et al. [60] and Simon-Deckers et al. [57], found slightly longer MWNTs (< 2–3 μm) in the vacuoles of the cytoplasm, within the free cytoplasm, near the nucleus, and even appearing to pierce the nuclear membrane. Much longer MWNTs (> 50 μm) caused frustrated phagocytosis (as seen through a light microscope) and stimulated TNF-α and superoxide (O_2^-) free radical production in human macrophage cells [73]. All these studies used different forms of microscopy to confirm the presence of MWNT within cells. Understanding how the MWNTs enter cells could provide further insight into their cytotoxic potential.

In a computer simulation, Lopez et al. [74] proposed that nanotubes could spontaneously penetrate the plasma membrane and create pore channels. NTs with a 2 nm length equal to the width of a plasma membrane bilayer hydrophobic core, a 1.3 nm diameter equal to the width of a water molecule, and functionalised hydrophilic end caps were computationally analysed. Figure 2.1 depicted the simulated results. The NT long axis first aligned parallel to the plasma membrane (a), and membrane lipids bound to the hydrophilic ends (b). Thermal fluctuations gradually pushed the NT towards the other end of the bilayer (c) allowing the bound membrane lipids to completely pull one end of the NT across the hydrophobic core (d). The NT situated perpendicularly in the plasma membrane as the lipids rejoined the opposite membrane layer and resulted as a pore (e) that could allow ions or peptides to cross between the intracellular and extracellular environment.

These results have led to the conclusion that MWNTs might not enter cells via active pro-

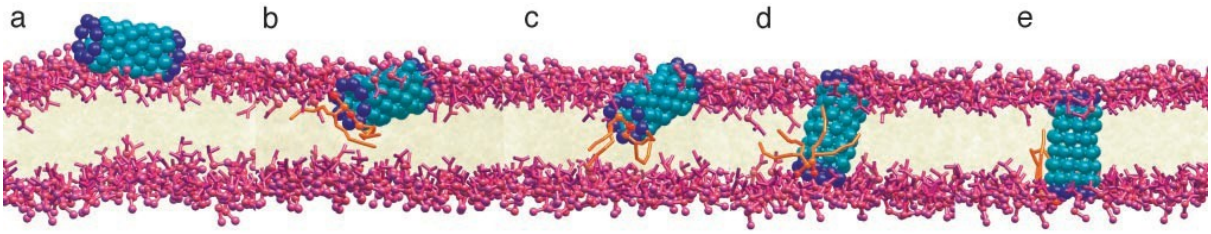

Figure 2.1: Depiction of a computer simulation of an NT crossing a plasma membrane bilayer: a) NT aligns parallel to plasma membrane, b) lipids bind to hydrophilic end cap, c) thermal fluctuation pushes the NT across the hydrophobic core, d) bound lipids begin to interact with opposite plasma membrane, and e) NT nestled across plasma membrane. (Image from Lopez et al. [74]

cesses such as endocytosis, but rather macropinocytosis or diffusion across the plasma membrane. Penetration could lead to negative consequences, such as damaging membranes or creating unnatural pores that expose intracellular compartments to the extracellular environment. Consequently, this study sought to use a combination of cell viability assays and microscopy to understand the cytotoxic effects and uptake mechanisms of MWNTs.

2.2 Materials and methods

2.2.1 Unpurified MWNT production

Aligned arrays of unpurified MWNTs with a carpet-like morphology (Figures 2.2 and 2.3) were synthesised by K. K. Koziol using a chemical vapour deposition (CVD) method from a solution of 5 wt% ferrocene in toluene injected into a furnace at 760°C under an argon atmosphere. The CVD method was used as a technique for producing large amounts of nanotubes with minimal contamination. Ferrocene was used as the source of the metal catalyst iron, and toluene was used as the solvent for ferrocene and the main source of carbon. MWNTs were grown on a quartz substrate and detached after synthesis.

2.2.2 Purification of MWNTs

The removal of metallic impurities from MWNTs by K. K. Koziol was based on high temperature annealing [75, 76, 77] rather than acid treatment in order to minimise highly reactive sites

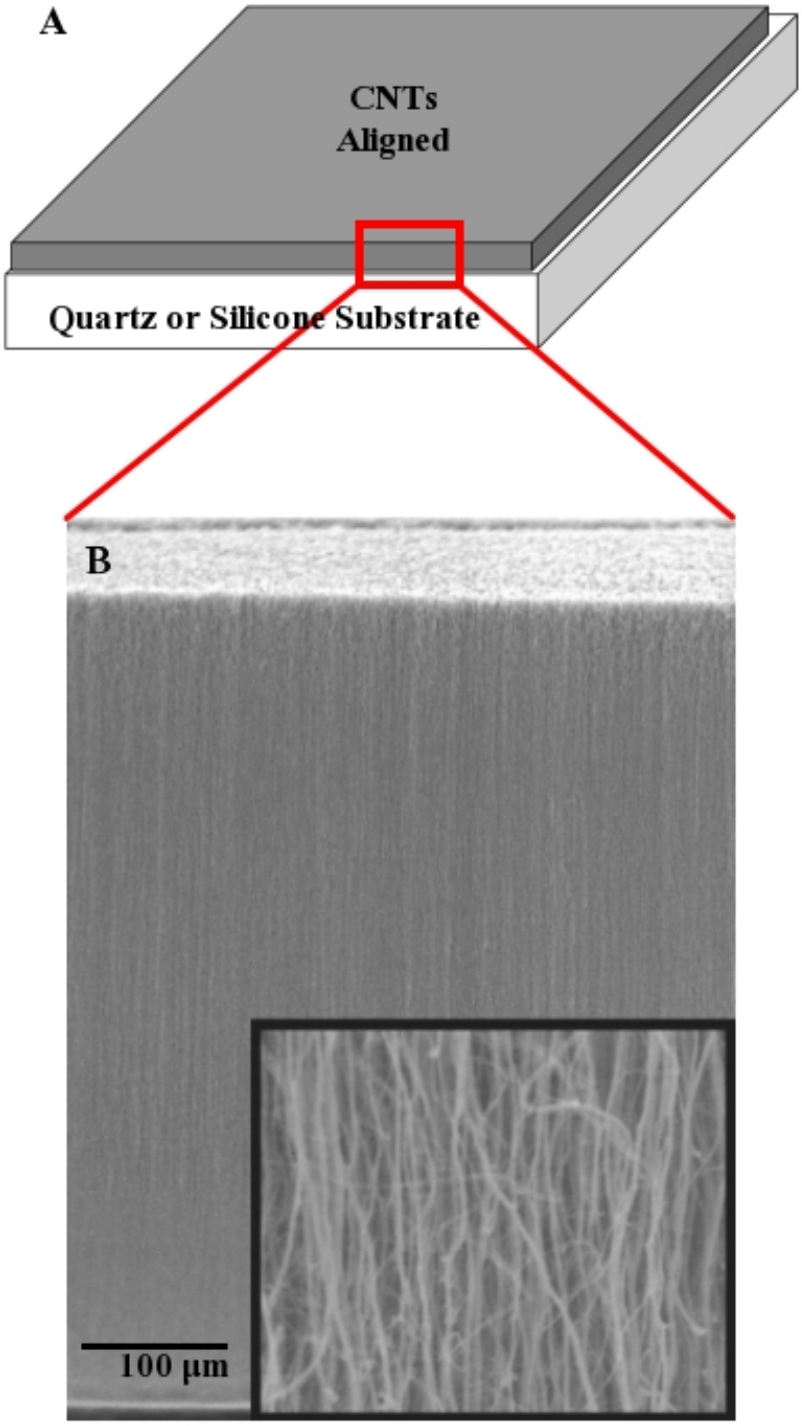

Figure 2.2: A) Diagram of vertically aligned carpet of MWNTs grown from a substrate. Maximum substrate dimensions were 50 x 70 mm. B) SEM image with a magnified inset of vertically aligned MWNTs. (Images and details provided by K. K. Koziol)

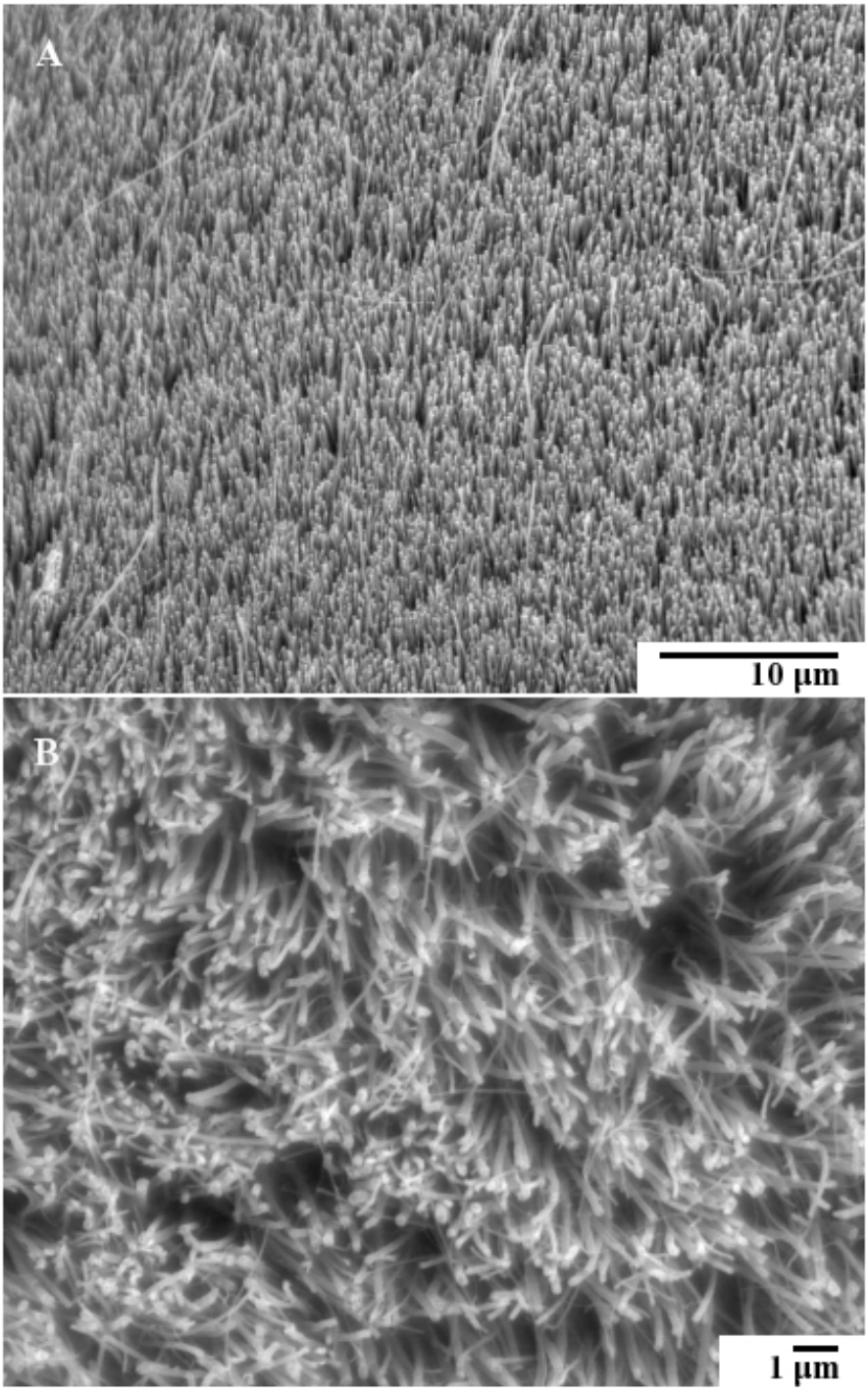

Figure 2.3: SEM images showing the top view of a MWNT carpet. Image B was at higher magnification. (Images provided by K. K. Koziol)

on the surface which could lead to ROS generation. The sample was heated to 2300°C for 6 hours in inert atmosphere (argon).

2.2.3 MWNT characterisation methods

K. K. Koziol performed the characterisation for both the unpurified and purified MWNTs. The protocols were as follows:

- **SEM –** MWNTs were dispersed in ethanol and a few droplets dispensed on an SEM stub and allowed to dry. ImageJ was used to measure the lengths of each individual MWNT.

- **TEM –** MWNTs were dispersed in ethanol and a few droplets were dispensed on a TEM grid and allowed to dry. ImageJ was used to measure the diameters of each individual MWNT.

- **Brunauer Emerett Teller (BET) –** MWNTs were dried thoroughly overnight using heat (200°C) and nitrogen gas. They were then loaded into a MicroMetrics TriStar 3000, and the chamber cooled with liquid nitrogen. The machine introduced nitrogen gas at controlled pressure increments, and the pressure measurements were compared with the saturation pressure to determine the amount of adsorbed gas. The surface area was determined based on the Brunauer Emerett Teller (BET) adsorption isotherm equation [78].

- **Inductively Coupled Plasma Atomic Emission Spectroscopy (ICP-AES) –** MWNTs were digested with HCl or nitric acid and calibration standards for the elements of interest were prepared. As the atoms and ions were excited by the argon laser, characteristic wavelengths and their intensities were emitted and compared to the calibrated standards to determine the exact quantities of the observed elements.

- **Raman Spectroscopy –** Samples were dried on a coverslip and the Raman spectrum taken using an argon ion laser with an excitation of 514.5 nm. The D peak (1500-1600 cm^{-1}) and G peak (~1300 cm^{-1}) could be determined from the Raman spectrum in order to calculate the I_D/I_G ratio (the intensity value of the D peak divided by the intensity value of the G peak), which assessed the amount of disorder within the CNTs. The D mode arose due to laser scattering from defects within the carbon atom structure while the G

mode originated from the carbon atoms vibrating tangentially. No defects would yield a ratio of zero [79].

2.2.4 Human monocyte-derived macrophage (HMM) isolation

Mature HMM cells were obtained from human buffy coat residues (National Blood Service, Brentwood, UK). Individual buffy coat residues were pooled from 3–4 donors and yielded enough HMMs to seed about 5–6 cell culture plates. The buffy coat residues were washed once with PBS, and the resulting cell sediment was mixed with an equal volume of fresh PBS. 30 mL of diluted buffy coat residue were layered onto 15 mL of LymphoPrep (Axis-Shields, Oslo, Norway), and, after centrifugation at 20 °C for 30 min at 600 g, the opaque interphase of mononuclear cells was removed and washed three times with PBS containing 4 mg/mL bovine serum albumin (BSA) to remove platelets. Monocytes were then enriched by an additional centrifugation step in a Percoll gradient [80]. Mononuclear cells were resuspended in 4 mL of PBS and mixed with 8 mL of Percoll: Hanks' balanced salt solution (10× concentrate, 6:1 dilution, at pH 7.0). After centrifugation at 20°C for 30 min at 450 g, the monocytes were collected from the top of the gradient, washed in PBS/BSA, and seeded in 24 and 48-well tissue culture plates at 1–2 × 10^6 cells/well and 0.5–1 × 10^6 cells/well respectively using macrophage serum-free medium (Mϕ-SFM, Invitrogen) unless otherwise stated. After incubation for 1 h at 37 °C, any remaining non-adherent cells were removed by washing twice with PBS. Adherent monocytes were cultured at 37°C in humidified air/5% CO^2 using Mϕ-SFM for at least 6–7 days prior to experiments unless stated otherwise, renewing the culture medium twice a week. HMM preparations were done by K. H. Müller and M. Motskin.

2.2.5 Dispersion

MWNTs are hydrophobic and tend to agglomerate causing extreme difficulty dispersing them in aqueous culture medium. With cell culturing, uniform dispersion is desired to ensure even chemical exposure to cells. As the purpose of this project is to explore natural exposure to MWNTs, minimal manipulation is desired.

MWNTs were initially dispersed in THF; however, THF was cytotoxic. As a result, bovine serum albumin (BSA) was used as the dispersing agent since it was not cytotoxic, and it was

previously used to study lung surfactant proteins [81, 82]. BSA also dispersed the MWNTs better than THF, an observation later confirmed by Buford et al. [83] who found that CNPs dispersed best in serum suspensions.

The MWNTs were first sterilised with ethanol which was subsequently evaporated. The MWNTs were then dispersed in a solution of BSA and phosphate-buffered saline (PBS) that would yield a concentration of 250 μg/mL BSA in the final culture medium treatment solution. The MWNT + BSA solution was sonicated for ~5 minutes before the culture medium was added. The final solution was vortexed, shaken vigorously, and sonicated to enable further dispersion. Although aggregates were still present, a 20 μg/mL solution appeared greyish-pink. As the MWNTs did fall out of solution, the mixture was agitated prior to addition to cells.

2.2.6 Cell viability assays

Three different assays were used: NR, MTT , and live dead.

For the NR, cells were gently washed with PBS for 2–3 times after MWNT treatment. 500 μL/well of NR dye at a concentration of 40 μg/mL in culture medium were added to the cells and placed in the incubator at 37°C for 2–3 hours. The NR dye was removed and the cells gently washed with PBS for 2–3 times. 500 μL/ well of an extracting solution composed of 50% ethanol and 1% glacial acid mixed in DIW was added to lyse the cells and release the dye from the lysosomes. The plates were returned to the incubator for 10–15 minutes. The solutions from each of the wells were mixed using a pipette (to ensure that any available dye has been fully resolubilised) and transferred to a 96-well plate. The absorbance was then measured at the wavelength 540 nm with a spectrophotometer.

For the MTT, cells were gently washed with PBS for 2–3 times after MWNT treatment. 500 μL/well of MTT dye at a concentration of 500 μg/mL in culture medium were added to the cells and placed in the incubator at 37°C for 1–2 hours. The MTT dye was removed and the cells gently washed with PBS for 2–3 times. 500 μL/ well of an extracting solution composed of 0.04 N HCl in isopropanol was added to dissolve the formazan crystals. The plates were returned to the incubator for 10–15 minutes. The solutions from each of the wells were mixed using a pipette (to ensure that any available dye has been fully resolubilised) and

transferred to a 96-well plate. The absorbance was measured at the wavelength 570 nm with a spectrophotometer.

For the live dead, macrophages were seeded and cultured on 13 mm coverslips. Two different dyes were used: Hoechst 33358 and PI. After sample treatment, 6 μL/mL of Hoechst 33358 (from a 1 g/L stock solution made with PBS) was added to each well 4–6 hours prior to confocal microscope imaging. 50 μL/mL of PI (from a 50 μg/mL stock solution made with PBS) was added to each well 30 minutes prior. The coverslips were placed in a lab-made petri dish: a 19 mm hole was drilled in the base of a 30 mm vented-side petri dish and covered with a 27 mm diameter #1 thickness cover-slip with elastomeric cement (Sylguard, Dow Corning) to make a viewing window. 2 mL of culture medium was added. Ten random frames were imaged for each concentration on a Leica SP1 confocal microscope with an HCX APO L U-V-I 40x 0.8w lens or a Leica SP2 confocal microscope with an HCX PL APO CS 63x 1.2 with correction lens. The number of live and dead cells were individually counted, and the results from all ten frames were totaled to determine the final cell death percentage.

2.2.6.1 Assessment of potential interactions between assay dyes and unpurified MWNTs

The MWNTs were incubated with the NR dye for 2–3 hours at a concentration of 40 μg/mL in culture medium and the MTT dye for 1–2 hours at a concentration of 500 μg/mL in culture medium before being washed twice with PBS. Solutions were centrifuged at each wash and the supernatant removed in order to eliminate the extraneous dye without aspirating the MWNTs or any dye that may have bound to the MWNTs. The appropriate extracting solutions (NR: 50% ethanol and 1% glacial acid mixed in DIW, MTT: 0.04 N HCl in isopropanol) were added to dissolve any existing dye and the solutions centrifuged. Only the supernatants were transferred to a 96-well plate in order to eliminate any possible interferences the MWNTs would cause with the laser detection from the plate reader. The NR was scanned at 540 nm and the MTT at 570 nm. There was no statistical analysis as the experiment was only performed once.

2.2.6.2 Unpurified MWNTs treatment

Once the HMMs seeded in 48-well plates were ready, the cells were treated with unpurified MWNTs. A stock solution was prepared for only the highest concentration (20 μg/mL). Subsequent concentrations (0.31 μg/mL to 10 μg/mL) were prepared from this stock solution by

diluting 1:2 with culture medium. The old culture medium was removed from the cells, and 500 μL/well of the treatment solutions were added. The cells were treated with unpurified MWNTs for 1, 2 or 4 days. The treatment solutions were removed, and the cell viability was assessed using NR, MTT, and live dead. The controls were prepared by treating cells under similar conditions but without any unpurified MWNT treatments. NR and MTT assays were performed in triplicates and repeated 6 times, and the live dead was repeated 7 times as singletons. Statistical analysis of ANOVA with LSD and $P < 0.01$ was performed using Analyse-it®.

2.2.6.3 Purified MWNTs and Fe_2O_3 treatment

For the purified MWNTs, a stock solution for the highest concentration (20 μg/mL) was prepared; and for the Fe_2O_3, the proportional equivalent concentration of Fe_2O_3 present at the highest unpurified MWNT concentration was calulated: 1 μg/mL Fe_2O_3 for 20 μg/mL of unpurified MWNTs. Subsequent concentrations for both chemicals were prepared from the stock solutions by diluting 1:2 with culture medium. The NR and MTT assays were performed in triplicates and repeated 3 times, and the live dead was repeated 5 times as singletons. Statistical analysis of ANOVA with LSD and $P < 0.01$ was performed using Analyse-it®.

2.2.7 Time-lapse

HMM cells were seeded and cultured on a 13 mm coverslip and treated with 5 μg/mL of unpurified MWNTs for 4 days. The coverslip was then transferred to a 35 mm Iwaki dish (Barloworld). HEPES buffer was added to eliminate the need for CO_2. 6 μL/mL of Hoechst 33358 (from a 1 g/L stock solution made with PBS) was added 4–6 hours prior to imaging. 15 μL/mL of Annexin V (from Invitrogen ApoDETECT Annexin V-FITC kit) and 5 μL/mL of PI (from a 50 μg/mL stock solution made with PBS) were added shortly before imaging. The Iwaki dish containing the coverslip was placed in a temperature-controlled environment (37°C) with constant oxygen supply on a Leica SP2 confocal microscope using an HCX PL APO CS 63x 1.2 with correction lens. Images were taken at periodic intervals to track the fluorescent colour changes.

2.2.8 Immunostaining

HMM cells were seeded and cultured on a 13 mm coverslip and treated with 5 μg/mL of unpurified MWNTs for 4 days. The treatment solution was removed and the coverslip washed once with PBS. The cells were fixed in 2% formaldehyde for 20 minutes at 4°C. The formaldehyde was removed and the coverslip washed with PBS. PBS containing 1% Triton X-100 and 1% Tween-20 was added for about 30 minutes to permeabilise the cells. The PBS solution was removed, and 2% BSA was added for about 30 minutes. The BSA was removed and, without washing, the primary antibodies (1/100 of cytochrome c (Pharmingen) and 1/500 of cleaved caspase-3 (Promega and Abcam) diluted in 2% BSA) were added and left to refrigerate overnight at 4°C in a humidified chamber. The coverslips were washed 3 times with PBS. 3 μL Hoechst (from a 1 g/L stock solution made with PBS) and the secondary antibodies (mouse anti-goat and rabbit anti-goat) at a concentration of 1/100 were added for 1 hour at room temperature. The coverslips were washed 6 times with PBS and, finally, once in DIW. It was placed face-down over a drop of Prolong medium atop a glass slide and left to dry overnight.

2.2.9 TEM

For general TEM sample preparation, HMM cells were seeded on 6-well plates. Following MWNT exposure, the cells were washed 3 times with saline and then fixed with 4% glutaraldehyde in PIPES buffer (0.1 M, pH 7.4) for 1 hour at 4°C. Without removing the glutaraldehyde, the cells were scraped and transferred to a polypropylene tube to be centrifuged. The supernatant was removed, saline added, and the mixture centrifuged again. This washing process was repeated for a total of 4 times to remove the glutaraldehyde while minimising cell loss. The cells were then incubated in suspension in 1% osmium tetroxide containing 1.5% potassium ferricyanide and 2 mmol/L calcium chloride in 0.1M PIPES buffer at pH 7.4 for 1 hour at 4°C. They were washed 4 times in de-ionised water (DIW) before bulk staining with uranyl acetate for 1 hour at room temperature and covered with aluminium foil. Samples were washed twice in DIW followed by graded solutions of ethanol (70, 95, and 100%) and 100% acetonitrile at three times for each solution. Samples were then infiltrated under vacuum in quetol resin (Agar Scientific, UK) for 3 days and finally cured in fresh quetol resin for 24 h at 60°C. The fixed and embedded cells were sectioned with an ultramicrotome at 70 nm for BF TEM.

For the morphological analysis, the cells were treated with 5 μg/mL and 20 μg/mL unpurified MWNTs for 4 days. A control was prepared by treating cells under similar conditions but without any unpurifid MWNT treatment. After embedding, the samples were sectioned at 70 nm. At least 1000 cells were identified as normal, apoptotic, or necrotic for each treatment condition (control, 5 and 20 μg/mL) according to reference images from Hardwick et al. [84]. Cells were counted as dead only if they exhibited clear signs of end-stage apoptotic or necrotic death. The experiment was repeated a total of 4 times. ANOVA with LSD and $P < 0.01$ was performed using Analyse-it®.

2.2.10 Active/Passive uptake

HMM cells were grown on 13 mm coverslips. To assess active uptake, the cells were treated with 5 μg/mL unpurified MWNTs and placed in the incubator at 37°C for 4 hours. The treatment solution was removed, coverslips washed with 2–3 times with PBS, and fresh culture medium added prior to imaging. To inhibit active processes in order to assess passive uptake, the coverslips were first refrigerated at 4°C for 10–15 minutes or when the culture medium had cooled down. The 5 μg/mL of unpurified MWNTs treatment solution was cooled to 4°C before addition to the cells, and the coverslips were placed back in the refrigerator at 4°C for 4 hours. After the 4 hour treatment, the coverslips were immediately washed 2–3 times with cold PBS and cold culture medium added until imaging. For imaging, the coverslip were transferred to a lab-made Petri dish (refer to section 2.2.6 Cell viability assays). 6 μL/mL of Hoechst 33358 (from a 1 g/L stock solution made with PBS) was added 4–6 hours and Calcein AM (1 μL/mL from a stock of 50 μg diluted in 100 μL DMSO) immediately prior to confocal microscope imaging to identify the nuclei and cytoplasm of living cells, respectively. The unpurified MWNTs were identified via reflectance from the internalised iron. Z-plane stacks were taken with a Leica SP2 confocal microscope using a HCX PL APO CS 63x 1.2 NA lens with a correction collar for coverslip thickness to create an average projection.

For the SEM, cells were grown on 6 mm coverslips and treated similarly as the the coverslips for the confocal imaging. After treatment, the coverslips were rinsed briefly in cold de-ionised water and quench frozen in melting propane cooled in liquid nitrogen according to Warley et al. [85]. They were transferred into a brass block which was placed in an Edwards

360 vacuum coating unit and brought to room temperature over 24 hours at a vacuum of < 1 x 10^{-5} mbar. They then were coated with a thin film of carbon and viewed in a FEI Philips XL30 FEGSEM operated at 5 keV or 20 keV for EDX.

For the viability assays, HMM cells were grown on 48-well plates and subjected to the same conditions as the imaging coverslips. The plates were treated with 5 μg/mL of unpurified MWNTs at either 37°C or 4°C. After 4 hours, the treatment solution was removed, and the cells gently washed 2–3 times with PBS (cold PBS for the cells at 4°C). Fresh culture medium was added, and the cells refrigerated at 4°C were placed in the incubator at 37°C for 1–2 hours to reactivate the cells since active cell processes were required for the viability assays. The NR and MTT assays were performed in triplicates for 3 separate experiments and the live dead individually in 5 separate experiments according to section 2.2.6 Cell viability assays. Controls were prepared by treating cells under similar conditions but without any unpurified MWNT treatments. Statistical analysis of ANOVA with LSD and $P < 0.01$ was performed using Analyse-it®.

2.2.11 Pulse chase

HMM cells were seeded on 48-well plates and treated with 5 μg/mL of unpurified MWNTs for 1 day (*pulse*). Cell viability was assessed using NR (refer to section 2.2.6 Cell viability assays) at various time points after the initial *pulse*: 0, 1, 2, 4, 7, 10, and 14 day. For the 0 day, cells were not washed in PBS prior to NR incubation because PBS washing frequently yielded low spectrophotometric readings. Controls were cells treated under similar conditions but without the unpurified MWNT pulse. Controls were performed in duplicates and NR in quadruplicates. Each experiment was repeated 3 times and statistically analysed with ANOVA with LSD and $P < 0.01$ using Analyse-it®.

2.3 Results

2.3.1 MWNT characterisation

Table 2.3 summarised the characterisation of MWNTs as determined by K. K. Koziol. The diameters and BET surface area of both MWNT samples were the same, although the lengths

	Length(μm)	Diameter (nm)	Surface Area (m^2/g)	Purity (wt% Fe)	I_D/I_G Ratio
Unpurified	2 – 164 (Mean: 26 $\pm$ 22.7)	68 $\pm$ 30	50	6.2	0.44
Purified	4 – 65 (Mean: 12 $\pm$ 9.9)	68 $\pm$ 30	50	0.0005	0.32
Method	SEM	TEM	BET	ICP-AES	Raman

Table 2.3: MWNT characterisation details as assessed by SEM, TEM, BET (Brunauer Emmett and Teller) method, ICP-AES (inductively coupled plasma atomic emission spectroscopy), and Raman spectroscopy.

of the purified MWNTs were about half of the unpurified MWNTs. ICP-AES confirmed that the high temperature purification removed the iron NPs from the unpurified MWNTs. The I_D/I_G ratio revealed a decreasing ratio, indicating that the perfection of the nanotube graphene walls (crystallinity) increased after heat treatment. One side effect of increasing crystallinity would be an increase in brittleness which could be seen in the shorter average length distribution of the purified MWNTs.

Iron NPs could mostly be seen encapsulated within the core of the unpurified MWNTs and on the outer surface (Figure 2.4). As the MWNTs were sealed during processing, only the iron on the outer surface would be directly exposed to the cells. X-ray powder diffraction (XRD) indicated these exterior contaminants as Fe_2O_3.

2.3.2 Assessment of cell viability assay interactions

The discovery that NPs may interfere with certain assays elicited the need to use more than one assay to assess the toxicity of MWNTs. Two colorimetric dye based assays—NR and MTT—and an imaging technique—confocal live dead—were used. The NR and MTT assays were chosen for their ability to analyse large sample sizes quickly; however, their simplicity and efficiency meant decreased sensitivity and limitations. For example, for both assays, a dying cell could register as viable as long as the cell membranes were intact for NR incorporation or dehydrogenase enzymes were present to convert the MTT. Consequently, a more sensitive assay was used as comparison—the live dead assay—which required the user to determine and tally each cell as alive or dead. Nonetheless, dead cells could detach from the coverslips which would deflate the toxicity.

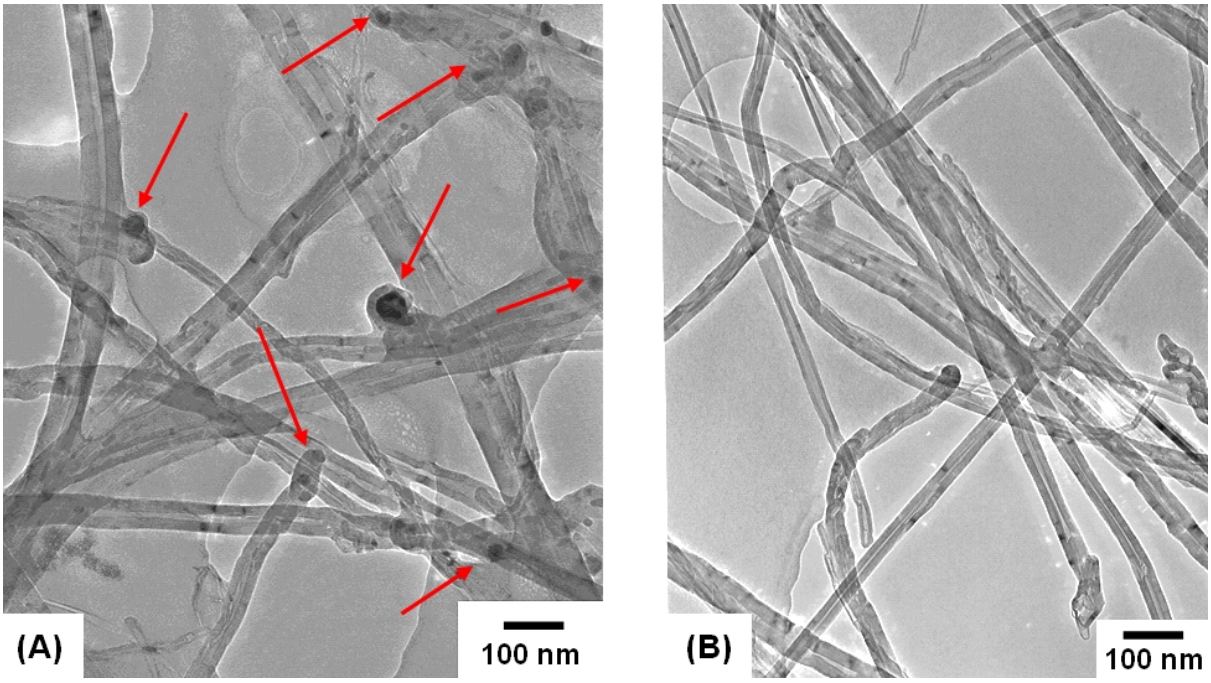

Figure 2.4: BF TEM images of MWNTs: A) unpurified MWNTs with presence of iron particles (red arrows), and B) purified MWNTs. (Images provided by K. K. Koziol)

As it is the dyes in the colorimetric assays that have been shown to bind to NPs, control experiments on the NR and MTT assays were performed using the same protocol as the experiments in this study—but without cells—in order to confirm that the MWNTs did not interfere with the viability assays. Minimal effects were observed for both assays suggesting that the nanotubes did not directly affect the viability assays (Figure 2.5). Only the unpurified MWNTs were assessed as they yielded minimal effects. The purified MWNTs were not assessed since they were derived from the unpurified MWNTs and were assumed to have similar properties.

2.3.3 Unpurified MWNTs toxicity

The HMMs were treated with unpurified MWNTs for 1, 2, and 4 days at concentrations of 0.31 to 20 μg/mL. A time and concentration dependent toxicity was observed with statistical significance for both the MTT and live dead assays at $\geq$ 10 μg/mL (Figure 2.6). Although assay control experiments revealed no interaction between the unpurified MWNTs and the colorimetric dyes, the MTT assay consistently yielded a significantly higher concentration de-

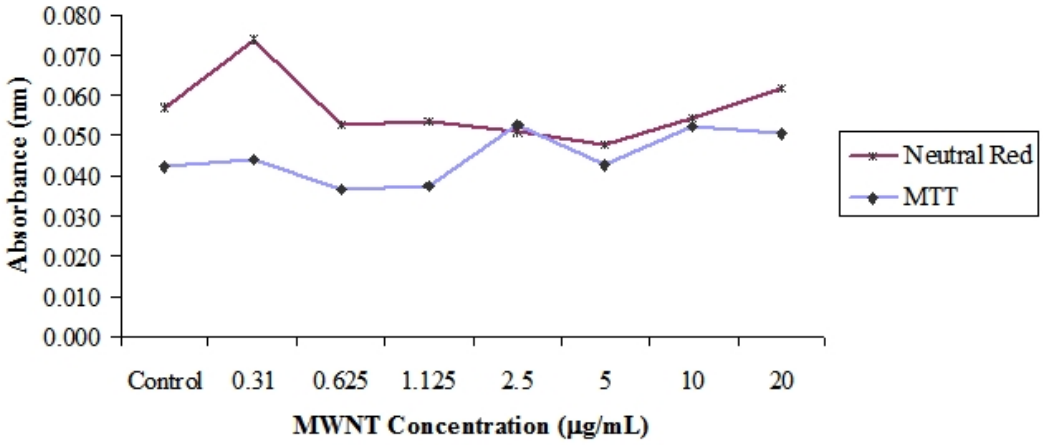

Figure 2.5: Effects of unpurified MWNTs on the NR and MTT dyes. Minimal effects observed.

pendent toxicity than NR and live dead; the highest toxicity was 58% at 10 μg/mL at 1 day. Interestingly, cell death decreased at 2 days. One possibility was that the unpurified MWNTs eliminated the vulnerable cells within the first day while the resistant cells remained viable against the unpurified MWNTs at the second day. By the fourth day, even the resistant cells had become susceptible to the unpurified MWNTs.

2.3.3.1 Mechanism of cell death

Various methods were explored to determine whether unpurified MWNTs caused apoptotic or necrotic death: time-lapse, immunostaining, and morphology.

Time-lapse Time-lapse was performed with the confocal microscope using Hoechst 33358, Annexin V, and PI stains. In normal cells, phosphatidylserine is a phospholipid that remains in the inner layer of the plasma membrane bilayer. During apoptosis, the phosphatidylserine is exposed into the outer layer, and Annexin V binds specifically to the phosphatidylserine [86]. When used in conjunction with PI, apoptosis can be differentiated from necrosis:

1. Hoechst 33358 is used to identify the nuclei of all cells (blue).

2. An apoptotic cell is stained green by the Annexin V. As the plasma membrane becomes permeable, PI, which only stains the nuclei of membrane-compromised cells, would stain the cell red. Thus, the colour sequence would be blue→green→red.

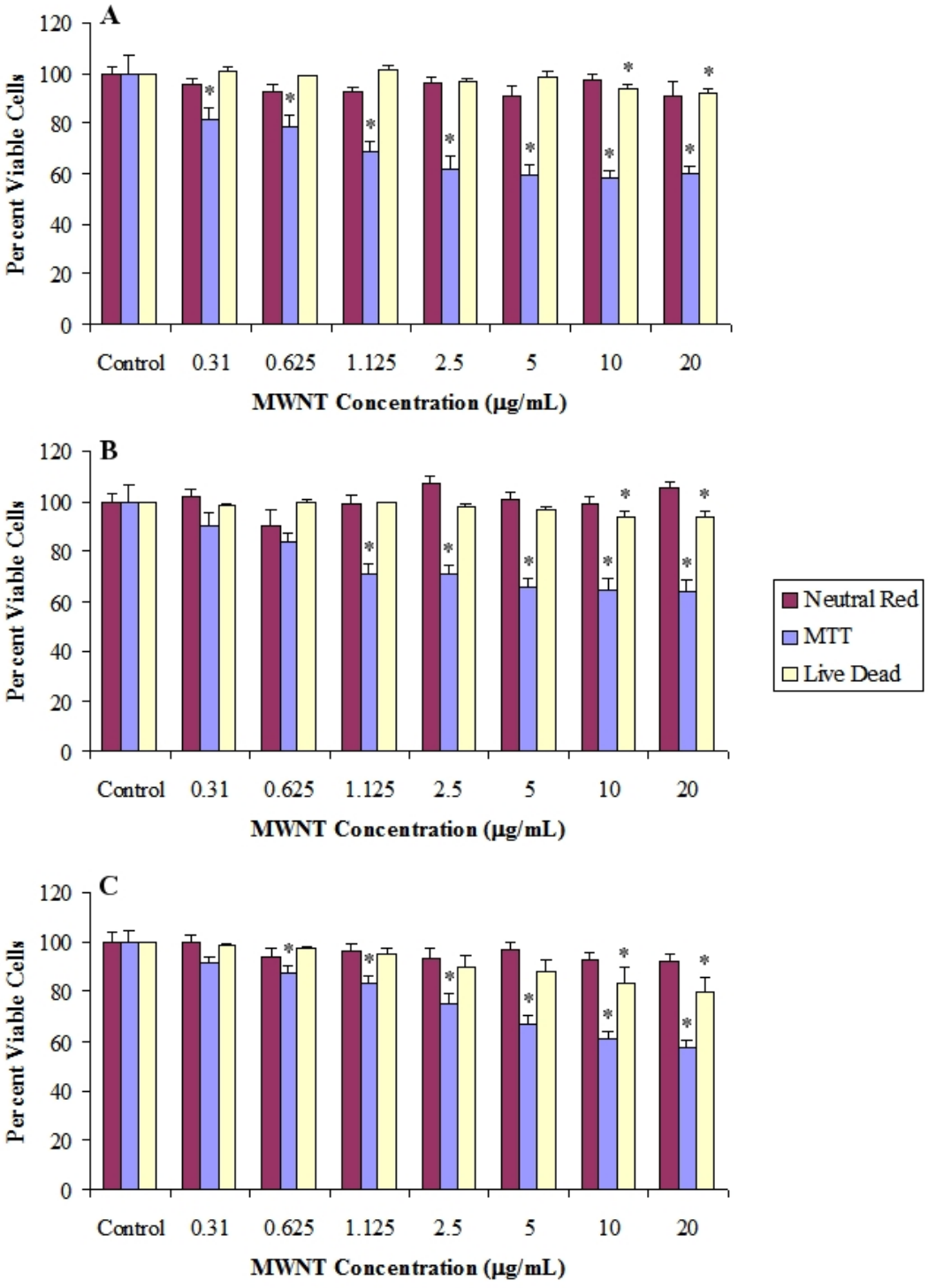

Figure 2.6: Toxicity of unpurified MWNTs. Cells were incubated with MWNTs for 1 (A), 2 (B), and 4 (C) days at 37°C. Cell viability was measured using NR, MTT, and live dead assays. NR and MTT values represented the mean ± SE of six experiments each performed in triplicates; live dead values were the mean ± SE of seven individual experiments (ANOVA with LSD, $P < 0.01$, Analyse-it®). Cells treated under similar conditions but without unpurified MWNTs were used as controls. Statistical significance (*) was assessed between the concentrations and their respective controls.

3. In necrosis, the plasma membrane is already compromised allowing PI to stain the nucleus. Annexin V subsequently infiltrates the cell and stains the now exposed phosphatidylserine. The colour sequence would be blue→red→green [87].

Figure 2.7 was a snapshot of a time lapse experiment with cells only and no MWNT treatment. Thermal drift frequently caused the coverslip to move out of focus during the live imaging. Consequently, the frame of focus could not be maintained long enough to observe significant changes in fluorescence. Additionally, the unpurified MWNTs were found to bind to the Annexin V stain, a different method—immunostaining—was pursued.

Immunostaining for cytochrome c and active caspase-3 Immunostaining eliminated live imaging; instead, cells were fixed and stained for cytochrome c and active caspase-3. Cytochrome c is found within the mitochondria and, when released into the cytosol, indicates early-stage apoptosis. Caspase-3 is an enzyme activated during late stage apoptosis [46]. For this protocol, difficulties arose with active caspase-3 autofluorescence. Active caspase-3 antibody from two different companies (Promega UK and AbCam) were used; however, it could not be determined whether the intense fluoresence observed was caused by active caspase-3 or the cells themselves.

Morphology TEM offered the ability to differentiate apoptosis from necrosis via cell morphology. Images from Hardwick et al. [84] were used as references to determine cells as normal, apoptotic, or necrotic (Figure 2.8).

1. Apoptotic cells appeared shrunken with a condensed cytoplasm and nucleus and heavily capped chromatin (Figure 2.8B).

2. Necrosis could be divided into primary or secondary necrosis:

   (a) Primary necrotic cells were identified as electron-translucent with cytoplasmic and nuclear contents appearing leached out and cytoplasmic vacuolation (Figure 2.8C).

   (b) Secondary necrosis occurred when apoptotic cells were not cleared away fast enough [34, 88]; consequently, they exhibited the nuclear condensation, heavily capped chromatin, and apoptotic bodies characterisitic of apoptosis and the leached out cytoplasmic and nuclear contents of primary necrosis (Figure 2.8D).

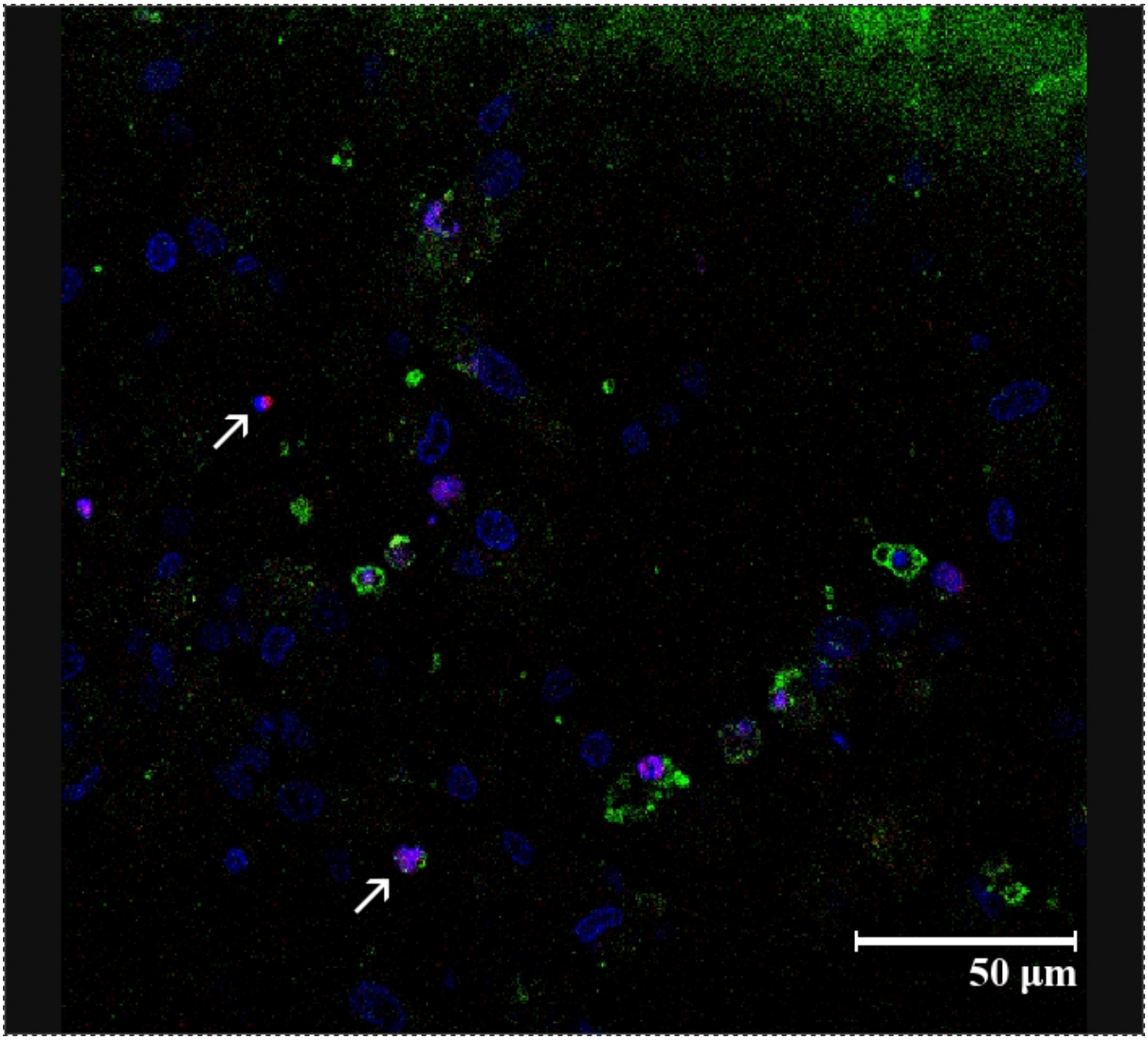

Figure 2.7: Confocal microscope snapshot of a time lapse experiment. HMM cells with fluorescent dyes only (blue = Hoechst 33358, green = Annexin V, red = PI); no MWNTs were present. White arrows indicated cells undergoing necrosis.

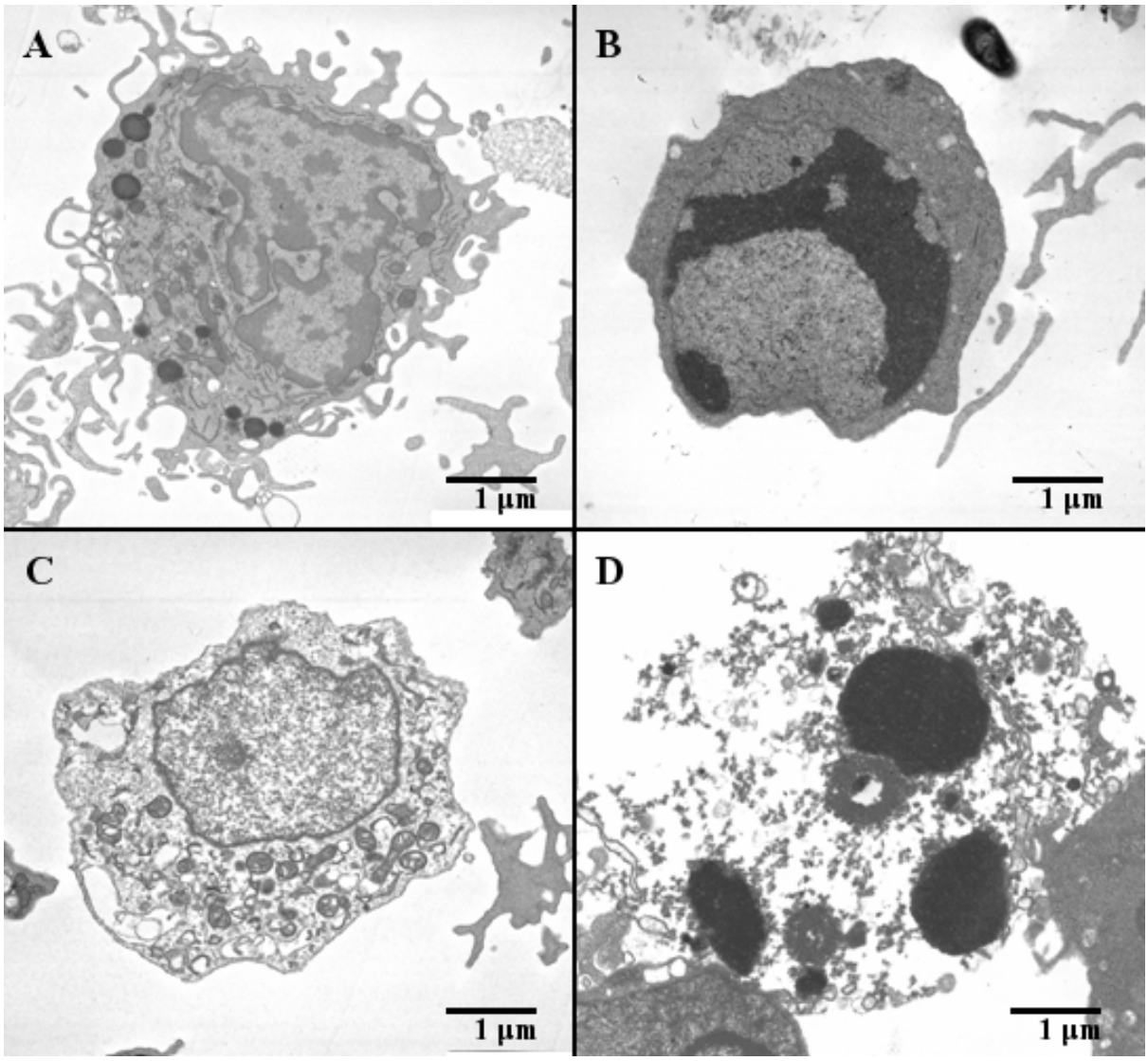

Figure 2.8: BF TEM images of characteristic cell morphologies: A) normal, B) primary apoptosis, C) primary necrosis, and D) secondary necrosis. (Images taken from Hardwick et al [84])

As this method was more labour intensive, only a medium (5 μg/mL) and high (20 μg/mL) concentration at the longest exposure time (4 days) were used. A similar concentration dependent toxicity was observed with 2.11% and 14.28% total cell death (apoptosis + necrosis) at 5 and 20 μg/mL, respectively; only the 20 μg/mL concentration was significantly toxic compared to the control (Figure 2.9). The main route of cell death observed was primary necrosis (Figure 2.10). Apoptosis was mainly observed as secondary necrosis. Additionally, a similar percentage of healthy to dead cells contained unpurified MWNTs suggesting that cells could survive with internalised unpurified MWNTs (Figure 2.11). However, this conclusion could not be confirmed as this study did not determine how long cells containing MWNTs survived and cells were only counted as dead if they exhibited end-stage death.

Furthermore, the 70 nm thickness required for TEM imaging meant that only parts of the cell were assessed for the presence of MWNTs; consequently, it was uncertain if MWNTs could be present in the unsectioned parts of the cell.

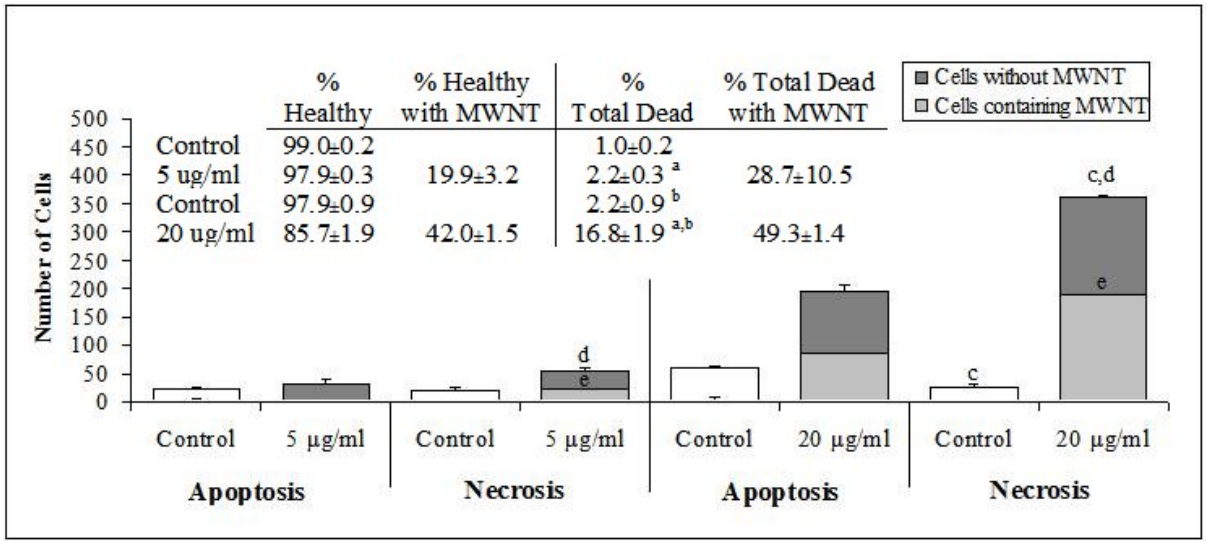

Figure 2.9: TEM viability analysis. Cells were treated with unpurified MWNTs for 4 days at 5 and 20 μg/mL and identified as healthy, apoptotic, or necrotic and whether MWNTs were present in cells or not. Values represented the mean ± SE of four experiments with 1000 cells indexed for each sample (ANOVA with LSD, $P < 0.01$, Analyse-it®). Cells treated under similar conditions but without unpurified MWNTs were used as controls. Letters (a–e) indicated significant difference between values with same letters. Control bars were coloured differently to reduce confusion with samples treated with MWNTs.

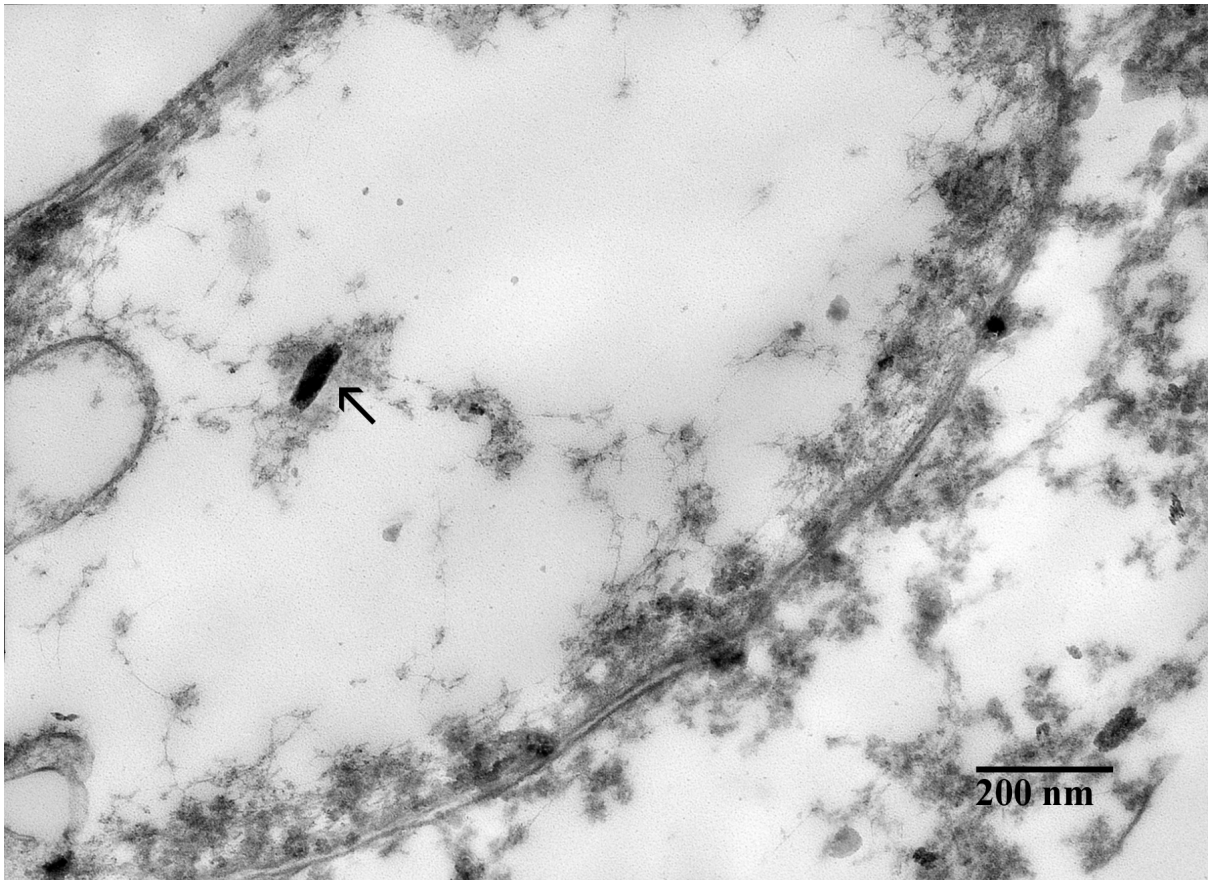

Figure 2.10: BF TEM image of a primary necrotic cell with an unpurified MWNT in the nucleus (black arrow).

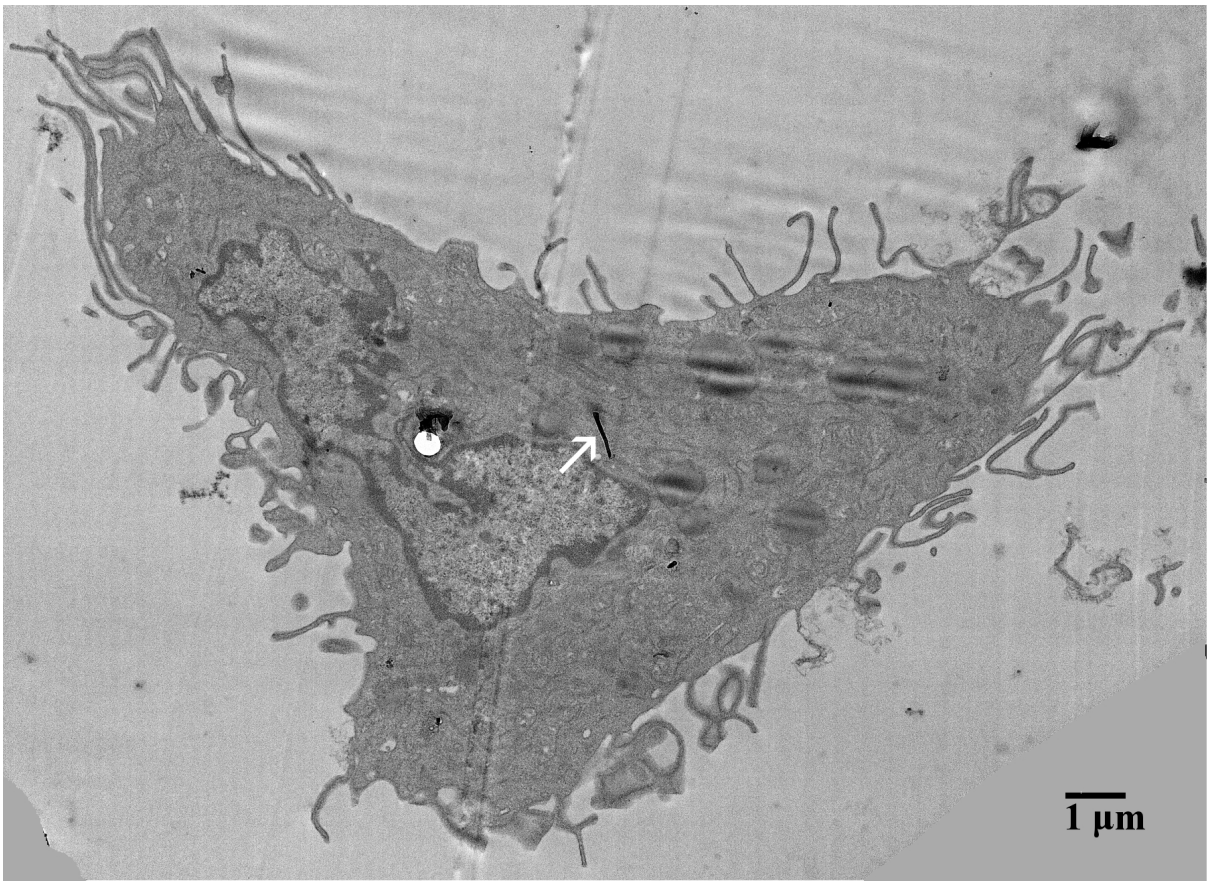

Figure 2.11: BF TEM image of a healthy cell with an unpurified MWNT (white arrow).

Several papers have suggested that MWNTs caused death via apoptosis rather than primary necrosis:

- Bottini et al. [55] only assessed for the presence of apoptosis using Annexin V on Jurkat cells.
- Ding et al. [59] observed dose-dependent apoptotic and necrotic death using YO-PRO1 (apoptotic cells) and PI (necrotic cells) stains on human skin fibroblasts but did not differentiate between primary and secondary necrosis.
- De Nicola et al. [58] used Hoechst 33358 to detect apoptosis and a combination of Hoechst 33358 and PI to differentiate primary from secondary necrosis on Jurkat cells. Primary necrotic cells were defined as PI-stained cells with swollen nuclei and secondary necrotic cells as PI-stained with fragmented or shrunken nuclei. They found that the MWNTs caused dose and time dependent increase in apoptosis and secondary necrosis, but no increase in primary necrosis. Increasing the time exposure increased secondary necrotic death with respect to apoptosis.

These results were contrary to those in this study as primary necrosis was observed as the main route of cell death with minimal apoptosis. Possible reasons for the different results between De Nicola et al. [58] and this study included differences in cell lines (Jurkat versus primary human monocyte macrophages), MWNT dimension and composition (110–170 nm x 5–9 μm with <0.1 wt% Fe versus 68 nm x 2–164 μm with 6.2 wt% Fe), and dose and time exposure (100 μg/mL for 24–48 hrs versus 5 and 20 μg/mL for 96 hrs). Additionally, necrosis could result from culturing cells for an extended time period.

2.3.4 Purified MWNTs toxicity

TEM showed that the majority of the iron was located within the bore of the unpurified MWNT sample and remained as iron NPs and inaccessible to cells (Figure 2.4). Some iron was found on the outer surface—potentially accessible to cells—but had been oxidised mainly into Fe_2O_3. Consequently, the unpurified MWNTs were purified via heat treatment (with no chemical treatment) to eliminate the outer iron contaminants, and cells were treated with purified MWNTs or Fe_2O_3 for 4 days at a proportionally equivalent concentration (i.e. 1 μg/mL Fe_2O_3 for the

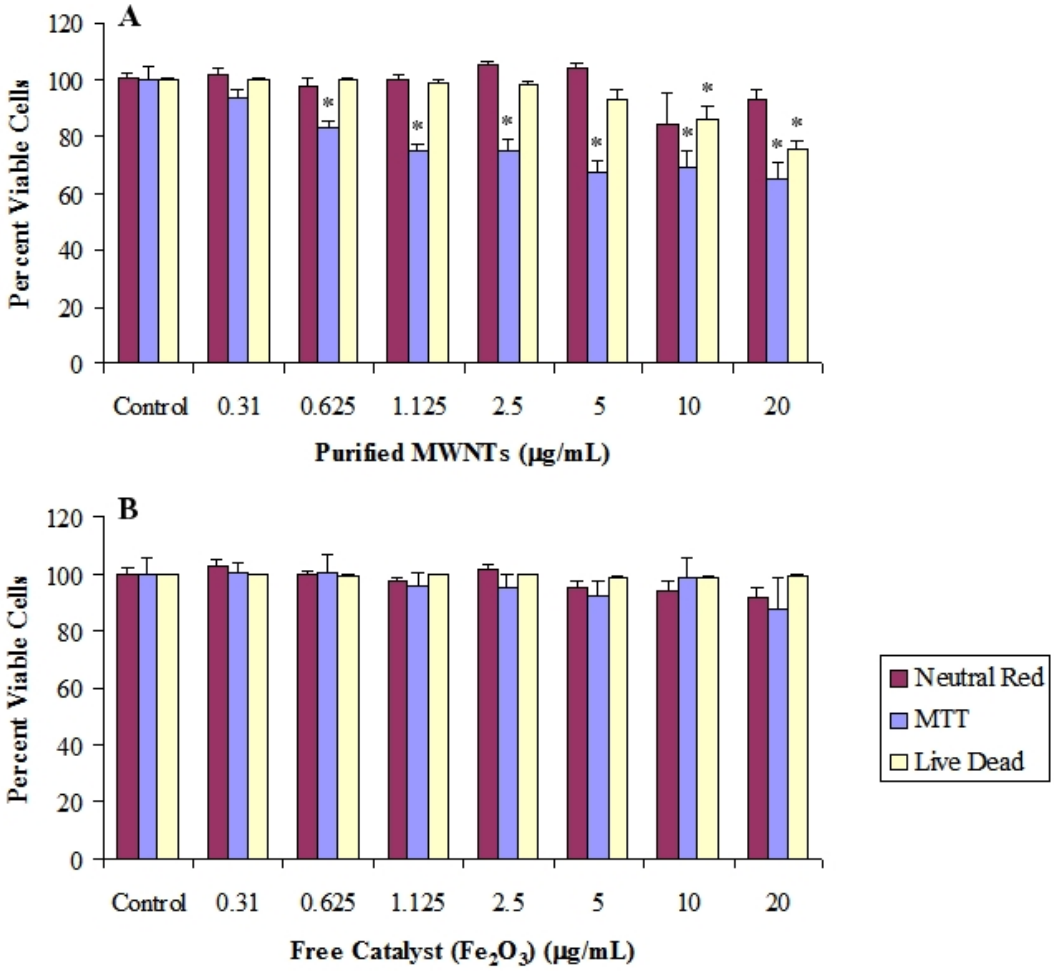

Figure 2.12: Cytotoxic response of cells to purified MWNTs and Fe_2O_3 after 4 days. Cell viability was measured using NR, MTT, and live dead assays. NR and MTT values represent the mean ± SE of three experiments each performed in triplicates; live dead values are the mean ± SE of five individual experiments (ANOVA with LSD, $P < 0.01$, Analyse-it®). Concentrations listed for "Free Fe_2O_3 (μg/mL)" were the proportionally equivalent amounts found in the unpurified MWNTs that were treated on the cells. Cells treated under similar conditions but without purified MWNTs or Fe_2O_3 were used as controls. Statistical significance was compared between the control and treatment concentrations within the individual experiments only (*); significant cell death was seen for the purified MWNTs but not the Fe_2O_3 NPs.

highest MWNT concentration of 20 μg/mL) to further identify the source of MWNT toxicity. Significant toxicity was observed at 10 μg/mL and above for the purified MWNTs whilst none was seen for the Fe_2O_3 (Figure 2.12). Although this study did not measure ROS generation, these results suggested that toxicity was caused by the nanotubes themselves and not the iron within or potentially leached out from the MWNTs.

The results in this study correlated with Simon-deckers et al. [57] and Muller et al. 2008a [68]. Simon-deckers et al. detected that unpurified and purified MWNTs of mean lengths 1.5 μm and diameters 44 nm yielded similar levels of cell death. Muller et al. 2008a concluded that metal contaminants did not generate ROS. They did, however, find that structural defects correlated with acute lung inflammation in rats and genotoxicity in rat lung epithelial cells. In this study, the MWNTs differed only slightly in the I_D/I_G ratios and were more structurally pure than those in the study by Muller et al. 2008a; thus, it could be possible to eliminate structural defects as a factor in the observed toxicity. Nevertheless, the purified MWNTs in this study were about half the length of the unpurified. Although the similar toxicities between the unpurified and purified MWNTs implied that length might not have any effects, such a conclusion cannot be confirmed as the samples were not the same in all aspects (e.g. Fe purity). Further work assessing ROS production is also needed to confirm the presence and source of ROS and whether there is a direct link between the presence of iron NPs, ROS production, and cytotoxic response.

2.3.5 Active/Passive uptake

The confocal microscope was first used to visually determine unpurified MWNT active and passive uptake. Unpurified MWNTs were found within the HMMs after treating for only 4 hours (Figure 2.13) and 4 days (Figure 2.14) at 37°C. To further assess how cells sequestered the unpurified MWNTs, cells were kept on ice and refrigerated at 4°C to inhibit active uptake. Unpurified MWNTs were still found within cells although there were noticeably fewer than at 37°C (Figure 2.15).

These data were confirmed further by SEM of cells treated with unpurified MWNTs at 37°C and 4°C. Cell surface images clearly identified internalised MWNTs extending from the cell surface (Figures 2.16, 2.17). This confirmed that MWNTs could enter cells via both active and

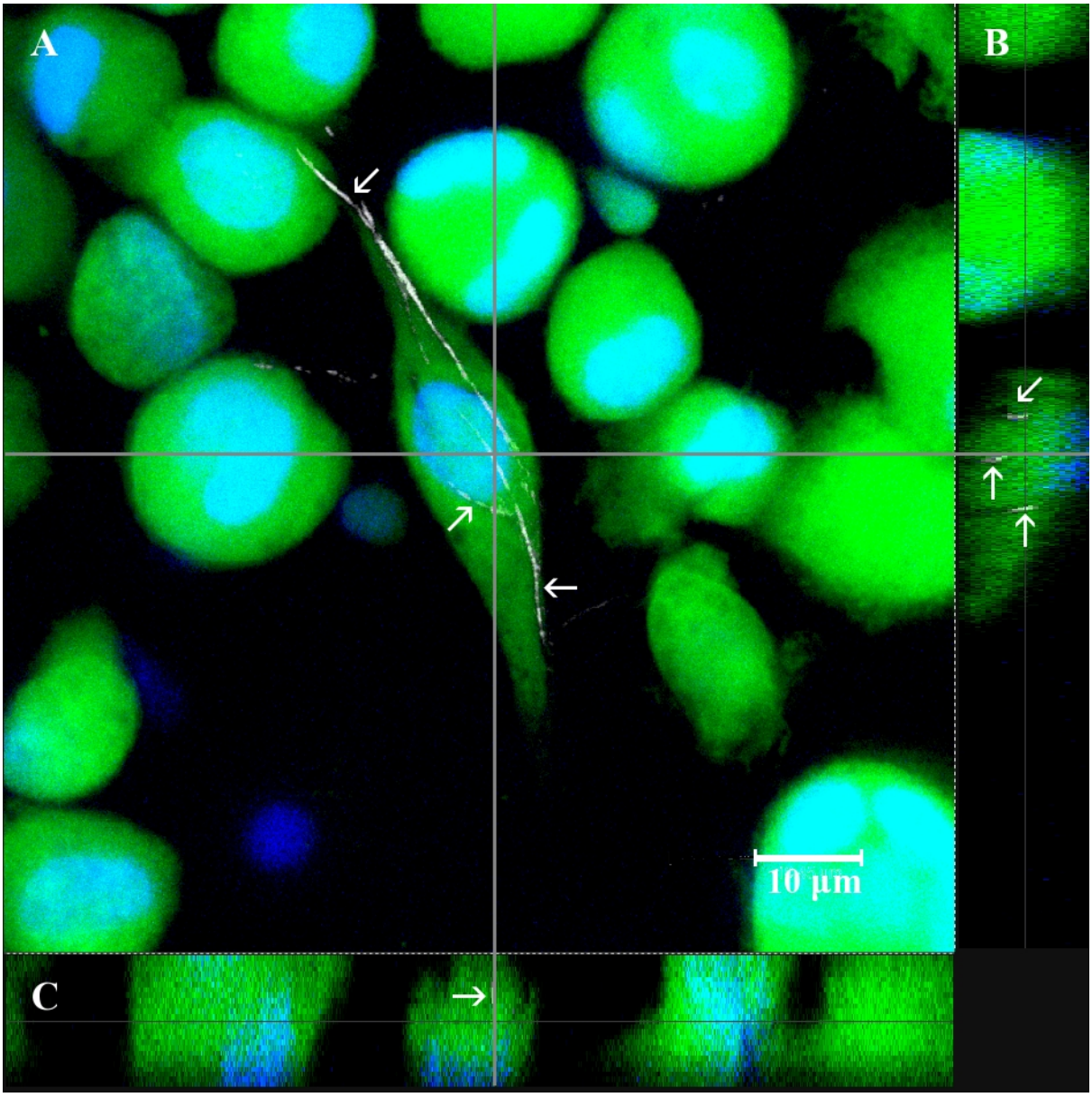

Figure 2.13: Confocal microscope average projection of a stack of images of unpurified MWNTs penetrating the cytoplasm of a cell after 4 hours at 37°C (green = cytoplasm, blue = nuclei, white = MWNTs). White arrows indicated the unpurified MWNTs. Inset A was a XYZ axes projection with a gray cross-section pinpointing the location for the YZ (inset B) and XZ (inset C) axes projections. White reflectance in insets B and C (white arrows) confirmed MWNT presence within the cytoplasm.

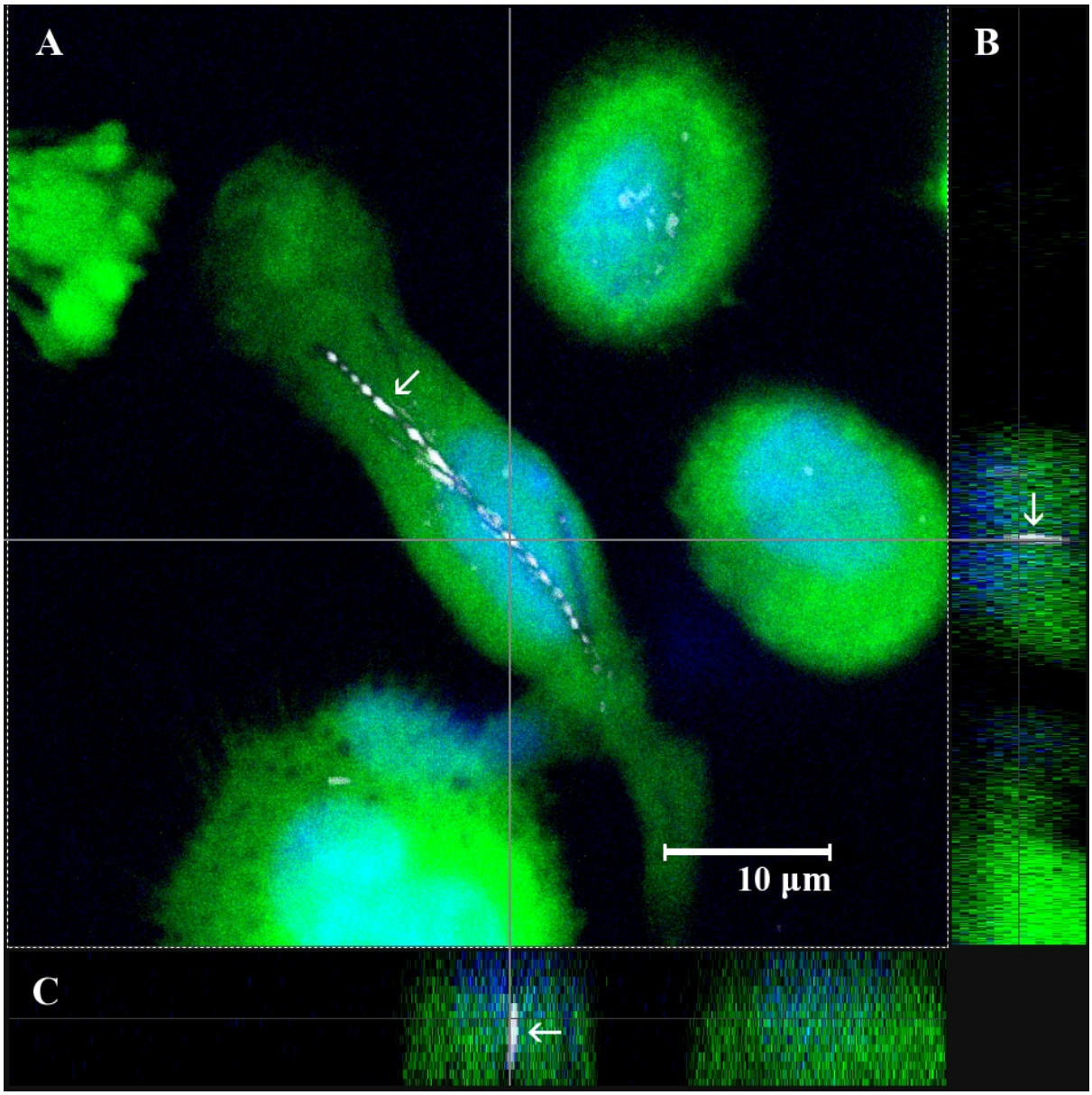

Figure 2.14: Confocal microscope average projection of a stack of images of unpurified MWNTs penetrating the cytoplasm and nucleus of a cell after 4 days at 37°C (green = cytoplasm, blue = nuclei, white = MWNTs). White arrows indicated the unpurified MWNTs. Inset A was a XYZ axes projection with a gray cross-section pinpointing the location for the YZ (inset B) and XZ (inset C) axes projections. White reflectance in insets B and C (white arrows) confirmed MWNT presence within the cytoplasm.

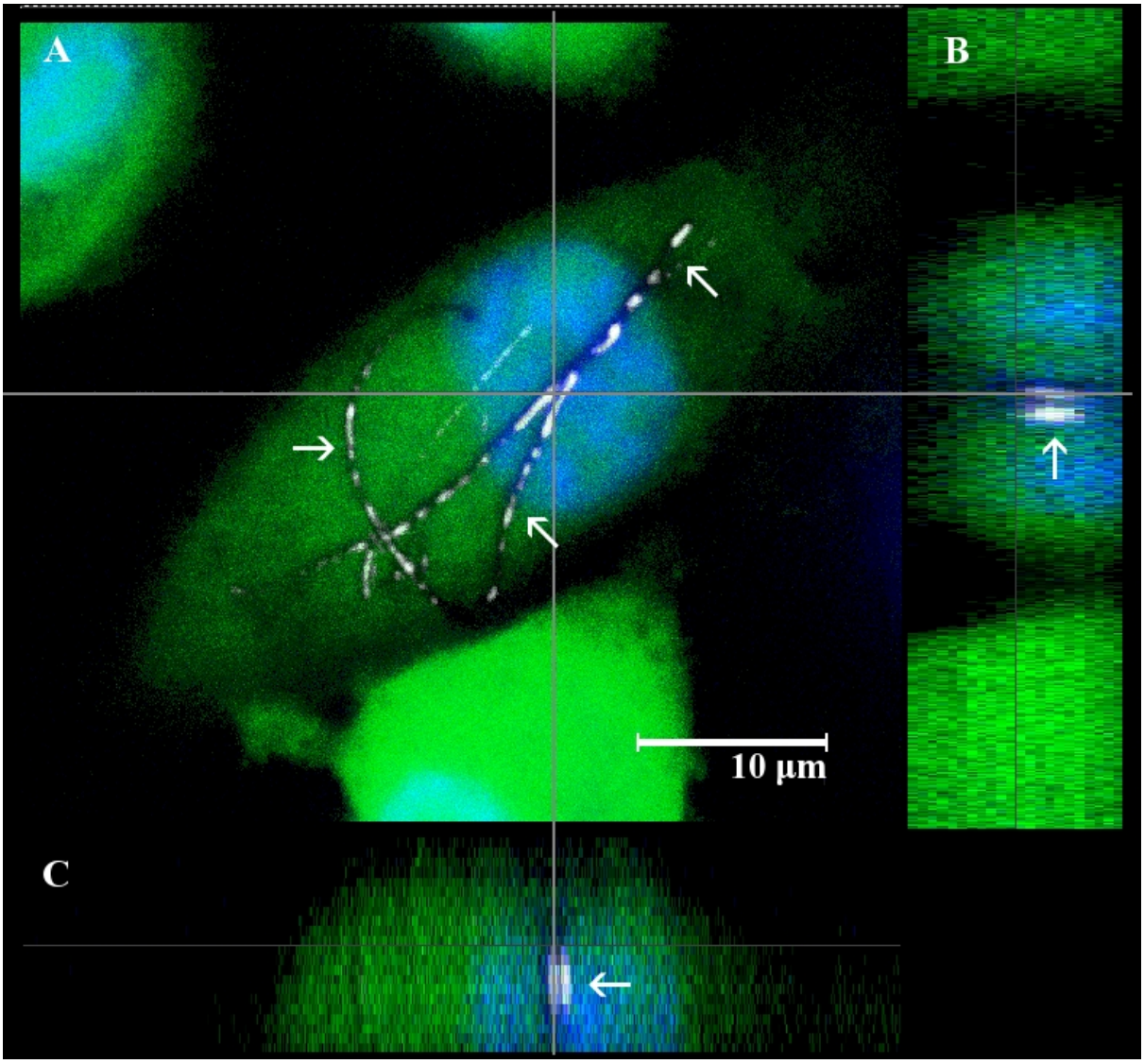

Figure 2.15: Confocal microscope average projection of a stack of images of unpurified MWNTs penetrating the cytoplasm and nucleus of a cell after 4 hours at 4°C (green = cytoplasm, blue = nuclei, white = MWNTs). White arrows indicated the unpurified MWNTs. Inset A was a XYZ axes projection with a gray cross-section pinpointing the location for the YZ (inset B) and XZ (inset C) axes projections. White reflectance in insets B and C (white arrows) confirmed MWNT presence within the nucleus.

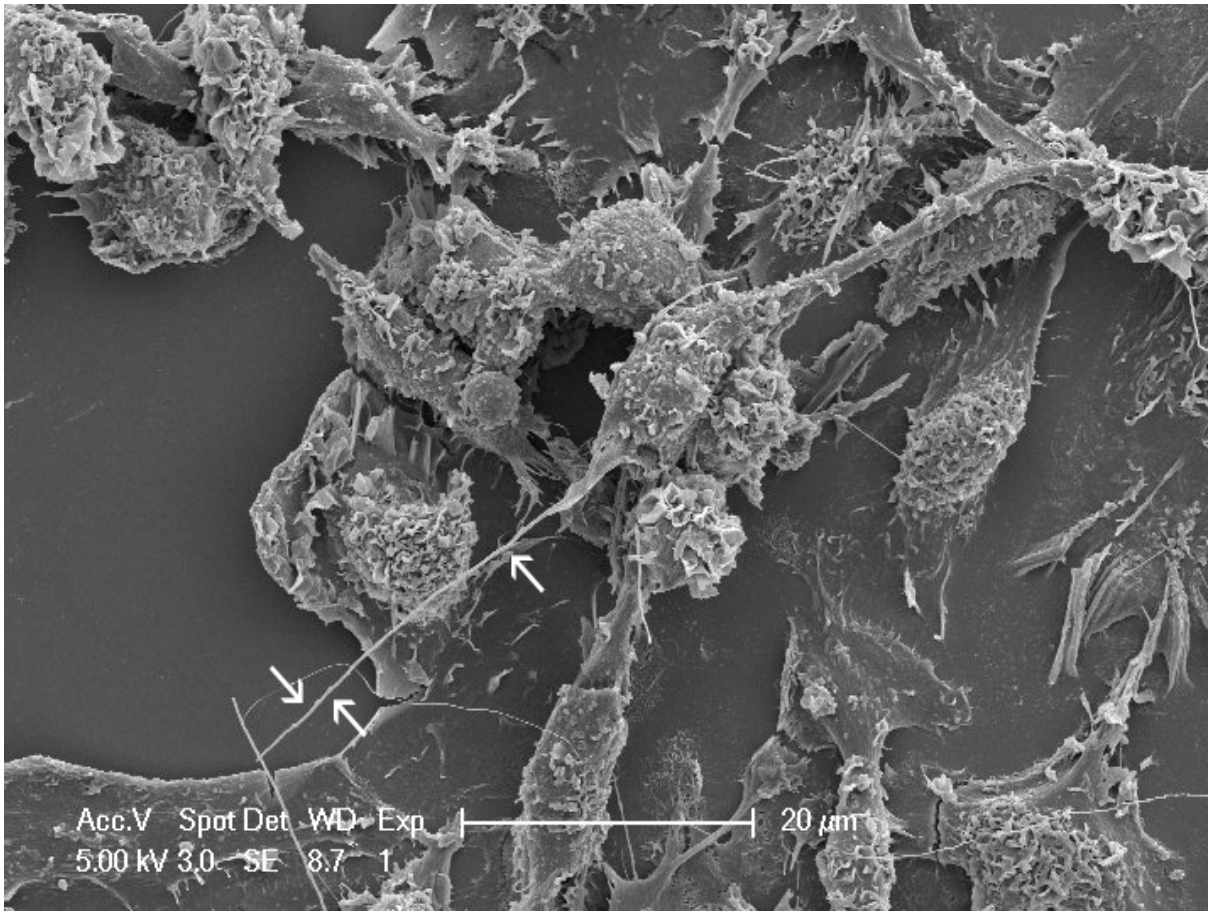

Figure 2.16: SEM image of an unpurified MWNT (white arrows) protruding from a cell after 4 hours at 37°C. Ragged and uneven cell surfaces were indicative of active cell processes; active cells were surrounded by membrane ruffles which, when quench frozen during sample preparation, were preserved as rough protrusions.

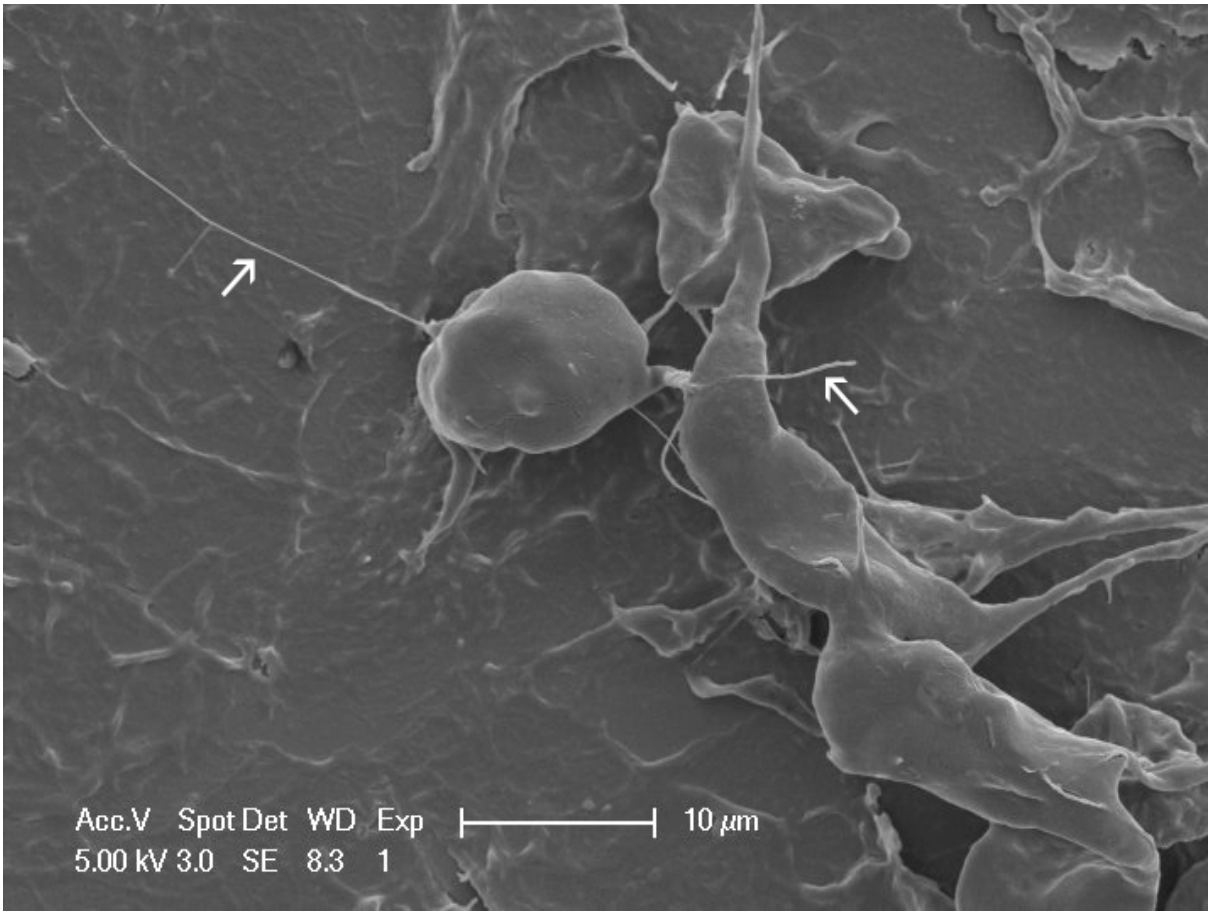

Figure 2.17: SEM image of an unpurified MWNT (white arrows) protruding from a cell after 4 hours at 4°C. Contrary to the previous figure (2.16), the cell surfaces appeared smooth; inactive cells were unable to produce membrane ruffles, which resulted in the observed smooth cell surfaces.

passive pathways. Viability assays were also performed to verify that no effects were caused by the refrigeration of cells (Figure 2.18).

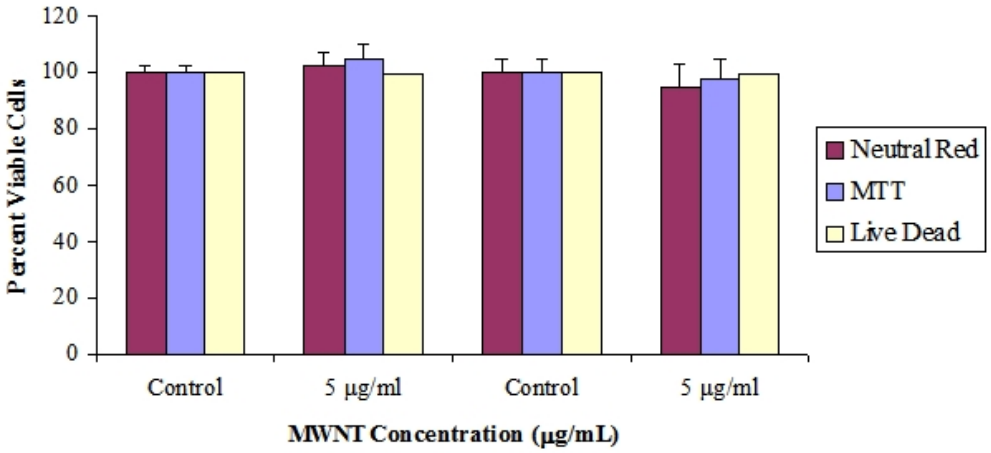

Figure 2.18: Cytotoxic response of HMM cells treated for 4 hours with unpurified MWNTs at 4°C and 37°C. NR and MTT values represented the mean ± SE of three experiments each performed in triplicates; live dead values were the mean ± SE of five individual experiments (ANOVA with LSD, $P < 0.01$, Analyse-it®). Cells treated under similar conditions but without unpurified MWNTs were used as controls. No significant differences between the treated conditions and the respective controls were observed.

2.3.6 Pulse chase

One of the main determinants of long term toxicity was DNA damage. ROS generation was a major contributor, although direct physical interactions between the CNTs and the proteins involved in division and DNA were also implicated [89]. As the MWNTs exhibited short term toxicity, long term toxicity was preliminarily assessed using a pulse chase. Cells were treated with the test substance at a non-toxic concentration for a short period of time (*pulse*) and subsequently cultured in culture medium alone for an extended period of time (*chase*). The effects of the substances internalised during the pulse could be assessed in the chase.

The HMMs were pulsed at 5 μg/mL for 1 day and chased for 14 days, the longest time period the primary cells could remain viable. Only the unpurified MWNTs were assessed as they were the most toxic in the cell viability assays. Figure 2.19 showed that the MWNTs did not cause any significant toxic effects during the 14 day chase. This suggested that the short

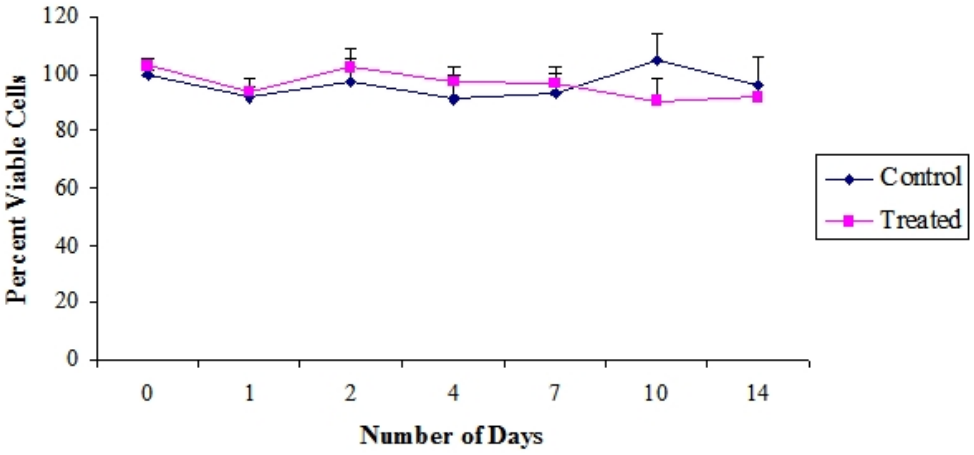

Figure 2.19: Toxicity of cells pulsed with unpurified MWNTs at 5 μg/mL for 1 day and chased for 14 days in culture medium alone. Cell viability was measured using NR. Control (cells treated under similar conditions but without MWNTs) values represented the mean ± SE of three experiments each performed in duplicates, while the treated cells represented the mean ± SE of three experiments each performed in quadruplicates (ANOVA with LSD, $P < 0.01$, Analyse-it®). No statistical significance was observed between the control and treated time points and between 0 day and all other days.

MWNT exposure did not cause any long term toxic effects. Several papers concluded otherwise. In another study by Muller et al. 2008b [89], the ground purified MWNTs (MWNTg) were found to induce both DNA damage and chromosome loss in rat lung epithelial (RLE) cells and human breast carcinoma cells (MCF-7) using a combination of a micronucleus assay and fluorescent in situ hybridization. This technique allowed discrimination between micronuclei containing a whole chromosome (indicating aneugenicity) and a chromosome fragment (indicating clastogenicity). The MWNTs were found to induce both events indicating the presence of DNA damage and chromosome loss. They disproved ROS as the contributor; instead, they suggested that the observed damage could result from physical interaction between cell proteins and the MWNTs or any metallic contaminants known to cause chromosome loss (e.g. cobalt). Zhu et al. [61] found that MWNTs induced p53 and increased the frequency of mutations; however, they implicated ROS as the contributor as they found MWNTs generated ROS based on Fe content. Different cell types (rat lung epithelial cells versus mouse embryonic stems cells), MWNTs dimensions (11.3 nm x 0.7 μm with < 2 wt% Co and Fe versus 9–30 nm x tens

of μm with < 0.49 wt% Fe), and treatment concentrations (10, 25, and 50 μg/mL versus 5 and 100 μg/mL) between the two studies may have caused the differing results. As this study only assessed the long term effects in terms of viability, direct analyses of DNA damage similar to these two studies are required.

2.4 Discussion

A variety of assays were used to help counter the possibility of NPs interfering with toxicity assays. Control experiments did not find unpurified MWNTs binding to the NR and MTT colorimetric dyes. However, the MTT results in this study consistently yielded higher cell death over the other assays. When Worle-Knirsch et al. [90] used the MTT assay to assess the cytotoxic effects of A549 cells treated with SWNTs, electron micrographs revealed that MTT formazan crystals had bound to the SWNTs which prevented their resolubilisation. Casey et al. [91] found that SWNTs could reduce the MTT into formazan without the presence of cells. They verified this observation by first incubating cells with the MTT dye and extracting the converted purple formazan crystals. SWNTs were then mixed with the crystals and found to convert the purple formazan crystals back to yellow, the colour of unconverted MTT dye. The interactions observed by these two studies would cause an inflated toxic response. Although control experiments in this study indicated that MWNTs did not lead to formazan production in the absence of cells, the consistently higher cell death observed with the MTT assay suggested that MWNTs may bind to the insoluble formazan product and prevent its resolubilisation. Further studies are required to confirm this observation. Nevertheless, a live dead assay and an ultrastructural analysis via TEM were used in this study to reduce sole reliance on spectrophotometric readings of NR and MTT dye accumulation.

All four methods concluded a dose and time dependent toxicity for unpurified and purified MWNTs. For the unpurified MWNTs, similar levels of toxicity were observed when compared to other studies. Both Hirano et al. [56] and Simon-deckers et al. [57] used pulmonary cell lines (J774.1 and A549) and found similar levels of cell death where time and concentration points corresponded. Both assessed higher concentrations and found even greater toxicity. If purity was considered, De Nicola et al. [58] assessed MWNTs with < 0.1 wt% Fe on Jurkat cells and found similar toxicities when treatment conditions corresponded. Although Pulskamp

et al. [63] found similar levels of cell death, they concluded that MWNTs exhibited no acute toxicity. No concrete conclusions could be drawn from any of these comparisons as the MWNT structural dimensions and cell lines were different; nonetheless, the similar cytotoxicities observed suggest that MWNTs were toxic *in vitro*.

Many papers have proposed the possibility of toxicity due to ROS generation from metal catalysts, the most pertinent being Fenton chemistry where Fe^{2+} could convert hydrogen peroxide (H_2O_2) into hydroxyl (OH^-) radicals and lead to lipid peroxidation or DNA damage. In this study, toxicity was observed only in the purified MWNTs and not the residual iron suggesting that the nanotubes themselves were the principle cause of cytotoxicity. The inactivity of iron should be confirmed in a future experiment via the DCFH-DA assay, for example, which measures the presence of H_2O_2. Another possible experiment is to analyse whether the increased brittleness of the purified MWNTs may have generated reactive sites along the outer structure, exposing electrons that could produce free radicals such as superoxide ($O_2^{\cdot -}$). Lastly, the effects caused by the length differences between the unpurified and purified MWNTs should also be assessed, potentially by comparing the original unpurified MWNTs with shortened ones.

Studies contradicted whether individual CNTs or aggregates caused greater toxicity. Wick et al. [92] found that well-dispersed CNTs were least toxic while Tian et al. [93] concluded the opposite. When Wick et al. compared the toxicity of two SWNTs with similar impurities (yittrium and nickel), the SWNTs dispersed with Tween-80 had fewer aggregates and were less toxic. The authors suggested that the higher toxicity of SWNT aggregates was caused by the stiffer and more solid nature. When Tian et al., however, compared the toxicity of unpurified and purified SWNTs, they found that the purified SWNTs were more toxic. The authors proposed that one possible reason for the difference in toxicity was contributed by the difference in aggregation as the unpurifed SWNTs tended to aggregate. The contradicting conclusions between these two studies could be explained by comparing the toxic effects of aggregates between *in vivo* and *in vitro* analysis. *In vivo*, aggregates would be lodged in the alveolar walls or glomerular capillaries causing granuloma formation. *In vitro*, however, the aggregates would be too large to cause any effects to cells: the reactive surface area decreased and the size could be too large for cell uptake. Instead, the individual CNTs would be able to enter cells more easily and cause more damage with their increased surface area. Even with the BSA, the MWNTs in this study still formed aggregates, and no analyses were made to

determine the aggregate size range. Future studies are required to determine the aggregating potential of the MWNTs and if there is a relationship between aggregation and toxic potential.

Imaging provided further clues to the active and passive cell uptake into the cytoplasm and nucleus by the MWNTs. Confocal microscpy and SEM confirmed that MWNTs could enter HMMs both actively and passively; and contrary to several papers, MWNTs longer than 3 μm were observed in cells, although the exact mechanisms for MWNT uptake remains to be identified. If the MWNTs can passively enter the cell by mechanically translocating through the lipid bilayer and create a nanopore as proposed by Lopez et al. [74], the MWNTs can damage membrane integrity or act as conduits for fluid and ion exchanges. Alternatively, MWNTs could mimic asbestos fibres and cause incomplete phagocytosis, where cells are unable to fully engulf particles. These activated macrophages may release ROS and attract additional macrophages; the surge in active macrophages can then lead to heightened ROS release. Additionally, digestive enzymes from the unsealed phagosome can enter the extracellular regions. Both the ROS and the digestive enzymes can lead to inflammation and may result in complications such as granuloma formation or fibrosis. Fibre ends protruding from macrophages caused by incomplete phagocytosis will prevent the macrophages from properly clearing the fibres from the lung and potentially lead to granuloma formation and fibrosis as well.

As MWNTs were observed in the nucleus, the reactive surfaces on the CNTs could generate free radicals and lead to DNA damage. CNTs can even bind to DNA and RNA [94]. Two studies confirmed that MWNTs damage DNA and chromosome, which could lead to genotoxic effects such as mutagenesis (formation of mutation) or carcinogenesis (formation of cancer). The pulse chase in this study found that MWNTs did not cause any long term effects to viability; however, further analyses are required to determine if the MWNTs may be damaging DNA or chromosome which the viability assays do not detect.

2.5 Conclusion

Both the unpurified and purified MWNTs exhibited dose and time dependent toxicity, and cell death mainly resulted from primary necrosis. The residual iron Fe_2O_3 yielded no toxicity. MWNTs were found to enter cells both actively and passively and were observed in the cytoplasm and nucleus. The results from this study contributed to the field in the following

ways:

- TEM was used to determine cell viability. This allowed differentiation between cell states (healthy, primary/secondary necrosis, apoptosis) and identification of MWNTs within cells. A relationship could then be proposed between the presence of MWNTs and cell states.
- The exposed residual iron was identified and its toxicological potential assessed directly on cells.
- Both active and passive uptake were visually confirmed using confocal microscopy and SEM.

The results from this study conclude that MWNTs can cause harmful effects to human cells, and the source appears to stem from the nanotubes themselves rather than the residual iron.

Chapter 3

SWNT

3.1 Introduction

SWNTs are very similar to MWNTs but with smaller dimensions. Structurally, they consist of only a single sheet of graphene rolled into a cylinder with diameters that can range from 0.4 to 2.0 nm [95]. The simpler structure has allowed researchers to determine whether SWNTs are metallic or semiconducting based on how the graphene sheet is "rolled up" (chirality). The circumference of the SWNT is defined as the chiral vector and can be drawn on a two-dimensional hexagonal lattice using the equation $C_h = n\ a_1 + m\ a_2$, where n and m are integers and a_1 and a_2 define the unit vectors. Depending on the location of the chiral vector, SWNTs can be labelled as armchair when $n = m$, zig-zag when $m = 0$, or chiral for all other types (Figure 3.1). SWNTs are metallic when $|n - m|$ is divisible by 3, while all other combinations are semiconducting [96].

As with MWNTs, applications of SWNTs are very broad. Their unique electrical conductivity make them ideal candidates for field-emission transistors, technology commonly used in computer circuits. Semiconducting SWNTs have been shown to switch between conduction and insulation, and such technology can be applied to the logic gates in computers that switch between binary "0" and "1" [51, 99]. SWNTs ($< 1\ \mu$m in length) make ideal probe tips for atomic force microscopy; their small diameter provides higher resolution, their high mechanical strength prevents breakage, and their surface reactivity allows functionalisation for studying electrochemical properties [100]. Biomedically, SWNTs have been explored as gene

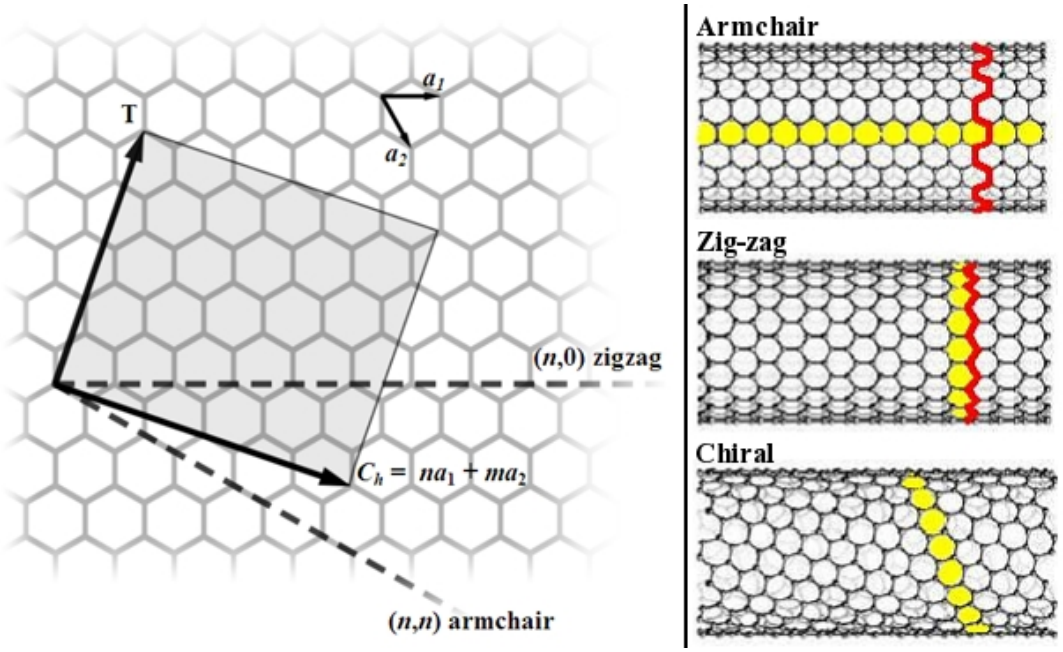

Figure 3.1: . Left: Two-dimensional hexagonal lattice structure with a chiral vector (C_h= n a_1+ m a_2), unit vectors a_1 and a_2 defined, tube axis (T), and chiral vectors for zig-zag and armchair nanotubes. Right: Three-dimensional structure of an armchair, zig-zag, and chiral SWNT. [97, 98]

and drug delivery vehicles, where SWNTs can be conjugated with various molecules such as amino acids, peptides, and DNA and transported into cells [101, 102]. SWNTs can also be conjugated with tumour markers and act as anti-tumour agents; an external near infrared laser source would heat the SWNTs internalised by the tumour cells and subsequently kill them [103]. However, their potential toxic effects to humans have similarly limited their development. Table 3.1 summarised the details of some of the papers discussed in this chapter.

Several studies found that SWNTs were the most toxic amongst the three carbon NPs C60, SWNTs, and MWNTs:

- De Nicola et al. [58] compared the toxicity of SWNTs to MWNTs in Jurkat cells treated with 25 or 100 μg/mL of each sample for up to 3 days. Cell death was calculated as a total of apoptotic and necrotic death. Apoptosis was identified as cells stained with Hoechst 33358 and containing fragmented nuclei, while necrosis was identified as cells stained with PI. A concentration and time dependent increase in cell death was observed with SWNTs exhibiting higher cytotoxicity in all concentrations and time points than

Table 3.1: Summary of experimental details of some of the SWNT papers discussed in chapter.

	Materials	Size	Impurity	Dispersant	Model	Conc	Time	Assay	Results
De Nicola	SWNT	L: 2-20 nm D: 5-9 nm	1% Co 1% Mo	Culture medium	Jurkat	25, 100 ug/mL	24, 48, 72 hrs	Hoechst, PI	Dose and time dependent apoptosis & secondary necrosis: SW > MW
	MWNT	L: 5-9 μm D: 110-170 nm	0.1% Fe						
Jia	SWNT	L: ~1 um D: ~1.4 nm	10%	Culture medium	Primary alveolar macrophages from guinea pigs	0, 1.41, 2.82, 5.65, 11.3, 28.2, 56.5, 113, 226 ug/cm2	6 hrs	MTT	Dose dependent toxicity: SW > MW > C60; SW toxic rate greater than MW
	MWNT	L: 0.5-40 um D: 10-20 nm	<5%						
	C60		<0.01%						
Zhang	SWNT	L: 5-15 um D: < 2 nm		Culture medium	Primary mice osteoblasts	0.1, 1, 10, 50, 100 ug/mL	24, 28, 72 hrs	MTT	Dose and time dependent toxicity: SW > MW
	MWNT	L: 5-15 um D: < 10 nm							
Cui				DMSO	Human embryo kidney (HEK293)	0.78, 1.56, 3.12, 6.25, 12.5, 25, 50, 100, 150, 200 ug/mL	1, 2, 3, 4, 5 days	MTT, centrifugation, morphology, DNA electrophoresis	Dose and time dependent toxicity, adhesion, and apoptosis; cell cycle arrest at G1 phase
Pacurari		L: 2-5 um D: 0.8-2.0 nm	10-30%	Culture medium + 1% fetal bovine serum	Normal & malignant mesothelial	12.5, 25, 125 ug/cm2	24 hrs	MTT, Trypan blue, Comet assay, H2DCFDA	Dose and time dependent toxicity, DNA damage, generate ROS (OH-, O2-, H2O2)
Shvedova	HiPco		30% Fe	Culture medium	Human bronchial epithelial (BEAS-2B)	60, 120, 240 ug/mL	18 hrs	Electron spin resonance	Detect formation of H2O2 and OH-
Pulskamp	Unpurified	L: < 100 um D: 1-2 nm	8%	Culture medium	Rat alveolar macrophage (NR8383) & A549	5, 10, 50, 100 ug/mL	24-96 hrs	WST-1, PI	< 20% cell death
	Acid treated		2.5%					DCF	4 (NR8383) and 8 fold (A549) ROS increase, purified no response
Wick	Agglomerates	Bundle size: micron range	2.9%	Culture medium	Human pleural mesothelioma (MSTO-211H)	7.5, 15, 30 ug/mL	3 days	Hoechst, MTT	Bundles (less aggregation) were less toxic than Agglomerates
	Bundles	Bundle size: 20 nm	6.2%	Tween-80					
Singh		L: 300-1000 nm D: 1 nm		PBS	Female BALB/c mice	60 ug/mice	30 min, 3 & 24 hrs	Radioactivity & gamma scintigraphy	Cleared from systemic circulation via renal excretion, half-life 3 hrs
Casey	HiPco		10% Fe	Culture medium				Absorption, fluroescence spectroscopy	SWNT bound to pH dye phenol red & riboflavin
Guo	Purified		10% Fe	Culture medium	Human hepatoma (HepG2)	0.01-10 mg/mL	24, 48, 72 hrs	UV, HPLC, MTS	Depletes 90% of phenol red dye from culture medium; binds to amino acids and vitamins; folate supplements recover decrease in viability

	Materials	Size	Impurity	Dispersant	Model	Conc	Time	Assay	Results
Davoren	HiPco	D: 0.8-1.2 nm	10% Fe	Culture medium	A549	1.56, 3.12, 6.25, 12.5, 25, 50, 100, 200, 400, 800 ug/mL	24 hrs	alamar Blue, Coomassie Blue, MTT	All assays yielded < 50% death
Jacobsen		L: < 1 um D: 0.9-1.7 nm	(0.3-2 ng/g)	Culture medium	Mouse lung epithelial (FE1-MML)	20, 40, 60, 80, 100, 200 ug/mL	24 hrs	LDH, NucleoCounter	No increase in cell death, attribute to decrease in proliferation
Zeni		L: 50 um D: 1.1 nm	< 10%	Culture medium	Primary human peripheral blood lymphocytes	5, 10, 25, 50 ug/mL	24, 48, 72 hrs	Trypan blue, LDH, Comet assay	Dose dependent decrease in cell growth; toxicity < 10%; no DNA damage
Herzog	HiPco	D: 0.8-1.2 nm	10% Fe	Culture medium	A549 & normal human bronchial epithelial (NHBE)	0.195, 0.38, 0.78, 1.56, 3.125, 6.25, 12.5, 25, 50 ug/mL	6, 24, 48 hrs	CellTiterBlue, ELISA	No cytotoxicity, decreased release of IL-8 & IL-6
Porter	HiPco	D: 0.9-1.2 nm	< 15%	THF	HMM	0-10 ug/mL	2, 4 days	TEM	SWNTs found in phagosome, lysosome, cytoplasm, nucleus

MWNTs. At the lowest concentration (25 μg/mL) and time point (24 hrs), SWNTs exhibited 12% cell death while MWNTs 8.5%; at the highest concentration (100 μg/mL) and time point (72 hrs), SWNTs exhibited 25% while MWNTs 22%.

- Jia et al. [104] compared the toxicity of C60s, SWNTs, and MWNTs in primary alveolar macrophages isolated from guinea pigs. 1.41–226 μg/cm^2 of each sample was added for 6 hours and MTT used to assess toxicity. At the lowest concentration, SWNTs caused 20% death, while MWNTs did not induce significant toxicity until 22.6 μg/cm^2(14% death). No toxicity was observed for C60 within the tested concentrations.

- Zhang et al. [105] compared the toxicity of SWNTs to MWNTs in primary mice osteoblast cells treated with 0.1–50 μg/mL of each sample for 1, 2, and 3 days. Cytotoxicity was similarly assessed with MTT and a concentration and time dependent toxicity for both samples observed. The SWNTs exhibited higher toxicity at the highest concentration for all time points: 30%, 37%, and 47% death for SWNTs versus 29%, 35%, 40% death for MWNTs.

All of these studies revealed the higher cytotoxic potential of SWNTs compared to other car-

bon NPs. Specifically, SWNTs were found to dose-dependently decrease cell viability, cell adhesion, and cell proliferation and to cause DNA damage:

- Cui et al. [106] assessed the effects of SWNTs on human embryo kidney cells treated with 0.78–200 μg/mL of SWNTs for 1–5 days. MTT was used for assessing viability. Cell adhesion was determined by first treating cells with fibrinogen and vitronectin, adding SWNT samples, and subsequently centrifuging to quantify spectrophotometrically the number of adherent cells. Apoptosis was identified morphologically as cells with condensed nuclei, chromatin condensation, and internucleosomal DNA fragmentation. A concentration and time dependent toxicity was observed for all three factors: viability, adhesion, and apoptosis. Further assessment with Western blot identified that SWNTs arrested the cell cycle at the G_1 phase, confirming the mechanism of death as apoptosis.

- Pacurari et al. [107] similarly observed that normal and malignant mesothelial cells treated with 12.5–125 μg/cm^2 of SWNTs for 24 hours caused concentration dependent toxicity as confirmed with the MTT and Trypan blue assays. DNA damage was identified using the comet assay.

Clearly, all six studies indicated that SWNTs were toxic. Several factors have been implicated as possible sources of toxicity, including ROS generation, dispersibility of the SWNTs, and interactions with the culture medium.

ROS generation. Two studies observed concentration dependent cell death correlated with ROS generation, and the addition of metal chelators reduced the cytotoxic response:

- Pacurari et al. [107] used electron spin resonance and H_2DCF-DA and identified presence of OH^-, O_2^-, and H_2O_2 with 12.5–125 μg/cm^2 of SWNT for 24 hours on both normal and malignant mesothelial cells. Deferoxamine, superoxide dismutase, and catalase—chelators of each of the respective ROS—all reduced the observed cytotoxic effects.

- Shvedova et al. [108] also used electron spin resonance on human bronchial epithelial cells (BEAS-2B) treated with 60–240 μg/mL SWNTs for 18 hours and observed similar

results. The ROS species OH^- and H_2O_2 were detected and treatment with deferoxamine and catalase both reduced ROS detection.

- A third study similarly observed ROS generation with SWNT treatments and correlated the ROS presence with metal contamination. Pulskamp et al. [63] detected up to 20% concentration and time dependent toxicity at the highest concentration and time point. Rat alveolar (NR8383) and epithelial cells (A549) were treated with 5–100 μg/mL unpurified and acid purified SWNTs for up to 8 days. The WST-1 and PI assays indicated up to 20% cell death at the highest concentration and time point. ROS generation was assessed using 2'7'-dichlorofluorescein (DCF) fluorescence and found to increase 4 fold in NR8383 cells and 8 fold in A549 cells for the unpurified SWNTs; the acid purified SWNTs yielded no response indicating that ROS was influenced by metal content.

Clearly, all three studies implicated that SWNTs could generate ROS. Although Pacurari et al. [107]and Shvedova et al. [108]did not compare their results with purified SWNTs, the presence of metal contaminants similar to Pulskamp et al. suggested their possible contribution.

Dispersion. Well-dispersed SWNTs were found to be less toxic than agglomerates. As discussed in the MWNT chapter, Wick et al. [92]found that SWNTs dispersed with the surfactant Tween-80 had fewer aggregates and were less toxic. Yet aside from surfactants, SWNT dispersion could be improved by attaching (or *functionalising*) functional groups (e.g. amines, esters) through covalent reactions between the surface of the SWNTs and the functional group [109]. Singh et al. [110] functionalised SWNTs with ammonium using the 1,3 dipolar cycloaddition reaction and found that they were excreted more quickly through the renal system in rats than unfunctionalised SWNTs, thereby decreasing toxicity. The functionalised SWNTs were radio-labelled with indium, 60 μg were injected into the tail vein of mice for 0.5–24 hrs, and the SWNTs traced using gamma scintigraphy. The functionalised SWNTs were found to exit the systemic circulation via renal excretion with a half-life of 3 hours. Additionally, the excreted SWNTs were still intact. These results indicated that SWNT dispersability could decrease their toxicity.

Interactions with culture medium. SWNTs have even been found to cause indirect toxic-

ity by binding to essential micronutrients in the culture medium, resulting in cell death due to nutrient starvation. Casey et al. **[91]** first confirmed that SWNTs bound to the pH indicator dye phenol red and riboflavin in culture medium using UV/visible spectroscopy. Guo et al. **[111]** assessed further and found that 80 μg/mL of purified SWNTs depleted 90% of the phenol red in culture medium. Using HPLC, the authors identified that the SWNTs most readily adsorbed to the amino acids tyrosine, phenylalanine, and methionine and vitamins folate, riboflavin, and thiamine at concentrations between 0.01–10 mg/mL. When nutrient depleted medium was replenished with folate, the majority of the observed cell death was recovered. The results from these studies indicated that the observed cytotoxicity of SWNTs may not be caused solely from interactions between the SWNTs and cells, but also from indirect reactions, such as the nutrient depletion by the SWNTs.

Although the previous studies indicated the cytotoxicity of SWNTs, a number of studies have concluded differently—that SWNTs were not acutely toxic:

- When three different assays (alamar Blue, Coomassie Blue, and MTT) were used in one study, all yielded less than 50% cell death in the concentration range tested (1.5–800 μg/mL) on A549 cells for 24 hours [112].

- In proliferating cell lines, two studies observed significant decreases in cell proliferation but no decrease in cell viability; no DNA damage was observed either. Jacobsen et al. [113] used the LDH and NucleoCounter live/dead assays to assess cell viability in mouse epithelial cells treated with 20-200 μg/mL of SWNTs. The cells were repeatedly seeded and treated with SWNTs for eight passages; and after each passage, the viability remained the same (90-99%), suggesting that the SWNTs were preventing proliferation rather than decreasing viability. Zeni et al. [114] used Trypan blue and LDH to assess the effects of 5–50 μg/mL of SWNTs on the proliferation of primary human peripheral blood lymphocytes (HPBL). The SWNTs concentration dependently decreased cell proliferation; however, cell death never exceeded 90%. Additionally, the comet assay did not yield any DNA damage.

- In a fourth study, 0.195–50 μg/mL of SWNTs dispersed in culture medium did not reduce cell viability; however, inflammatory markers such as IL-8 and IL-6 were suppressed,

potentially leading to a less responsive immune system [115].

Clearly, such contradicting results have made establishing the toxic potential of SWNTs difficult. This study sought to use the same cell viability assays and microscopy techniques applied to the MWNTs in an effort to draw a more definite conclusion. Additionally, by applying the same techniques, a comparison could be drawn between the MWNTs and SWNTs.

3.2 Materials and methods

3.2.1 HiPco SWNT production

HiPco SWNTs were purchased from Carbon Nanotechnologies Inc (CNI). Developed at Rice University for large-scale SWNT production, the HiPco process utilised gas-phase CVD by flowing CO gas with $Fe(CO)_5$ into a high pressure (30–50 atm) and high temperature (900–1100°C) reactor. The high temperature decomposed the $Fe(CO)_5$ into iron clusters that acted as nuclei for SWNTs to nucleate and grow [116].

3.2.2 Unpurified and purified SWNT production

Both the unpurified and purified SWNTs were synthesised by K. K. Koziol. The unpurified SWNTs were generated using thermal CVD heated to 1100°C for 30 minutes. Iron NPs were stabilised in magnesium oxide (MgO) to maintain the small sizes required for SWNT diameters (or the iron would aggregate and form MWNTs) and the substrate placed directly into the furnace. Methane was used as the carbon source.

The SWNTs were purified using concentrated hydrochloric acid (HCl) (35%). The unpurified SWNTs were placed in the HCl and mixed by hand for 10 minutes before being left alone for 24 hours. The HCl was then decanted and replaced with fresh HCl (repeated 3 times). The HCl was decanted one final time and replaced with DIW. The slurry was then filtered and washed with DIW several times via a vacuum-filter system before being dried.

3.2.3 SWNT characterisation methods

3.2.3.1 Raman spectroscopy

The diameter and I_D/I_G ratio were determined using Raman spectroscopy (refer to chapter 2.2.3 MWNT: MWNT characterisation). Spectra from four different areas were measured, and the following equation was used to calculate the diameters [117]:

$$\begin{aligned} \omega_{\text{RBM}} &= \frac{\text{A}}{\text{dt}} + B \\ where, \quad \omega_{\text{RBM}} &= wavelength\, determined\, from\, Raman\, spectrum \\ A &= 234\, cm^{-1} \\ B &= 10\, cm^{-1} \end{aligned}$$

The final diameter for each of the SWNT samples was calculated by averaging the four calculated diameters for each sample.

3.2.3.2 BET

The BET surface area was measured using the MicroMetrics TriStar 3000 (refer to chapter 2.2.3 MWNT: MWNT characterisation).

3.2.3.3 ICP-AES

The ICP-AES analyses for the unpurified and purified SWNTs were performed by K. K. Koziol (refer to chapter 2.2.3 MWNT: MWNT characterisation).

3.3 Dispersion

Similar to MWNTs, SWNTs are hydrophobic and tend to aggregate due to van der Waals forces. As described in the MWNT chapter (2.2.5 MWNT: Dispersion), uniform dispersion is desired in cell culturing. For this study, SWNTs were dispersed with BSA using the same protocol as the MWNTs and were compared to SWNTs dispersed in culture medium alone. The SWNTs were found to disperse better without BSA. As minimal manipulation was desired to mimic natural exposure conditions, all experiments were carried out by first sterilising the

SWNTs with ethanol, evaporating the ethanol, and then dispersing the SWNTs directly in the culture medium. The solutions were agitated prior to addition to cells as the SWNTs fell out of solution.

3.3.1 Cell viability assays

HMM cells were prepared according to chapter 2.2.4 (MWNT: HMM isolation), and three different assays were used to assess cell viability: NR, LDH, and live dead. Refer to chapter 2.2.6 (MWNT: Cell viability assays) for NR and live dead protocols.

For the LDH, HMM cells were grown on 48-well plates. The experimental control was prepared by culturing cells similarly but without any SWNT treatment. After treatment, the plates were centrifuged and 100 μL of the *sample* supernatants transferred to a 96-well plate. A *background control* was prepared by adding 100 μL of culture medium only to separate wells in the 96-well plate.The remaining sample supernatants from the 48-well plates were removed and 500 μL of 2% Triton X-100 in culture medium was added to lyse the cells. This provided the *high control*. The plates were incubated at 37°C for 25–30 minutes before being centrifuged and 50 μL of the supernatants transferred to the 96-well plates (different set of wells from the initial 100 μL of sample supernatants). A *high control background control* was prepared by adding 50 μL of 2% Triton X-100 only to separate wells in the 96-well plate. As the assay is light sensitive, all procedures henceforth were performed in the absence of light.

The LDH Cytotoxicity Kit from Roche Applied Science was used. The diaphorase/NAD^+ catalyst mixture was reconstituted with 1 mL DIW for 10 minutes. For 100 tests, a reaction mixture was prepared by adding 11.25 mL of the diaphorase/NAD^+ mixture to 250 μL of the ready-to-use Iodotetrazolium chloride (INT) and sodium lactate dye. 100 μL of this reaction mixture was added to the 100 μL of sample supernatants and 50 μL of high control supernatants. The 96-well plate was covered with aluminium foil and left at room temperature for 20–25 minutes. The presence of LDH caused the diaphorase to convert the dye into formazan which generated the color for the spectrophotometer to detect at 500 nm. The following formula yielded the % LDH released [39]:

$$\frac{(sample - background\,control)}{(sample - background\,control) + (high\,control - high\,control\,background\,control)} \times 100$$

3.3.1.1 Assessment of potential interactions between assay dyes and SWNTs

For the NR, the same protocol for the MWNTs was used for the SWNTs (chapter 2.2.6.1 MWNT: Assessment of potential interactions between assay dyes and unpurified MWNTs). Briefly, the SWNTs were incubated with the NR dye for 2–3 hours and washed twice with PBS (via centrifugation and removal of supernatant). The extracting solution of 50% ethanol and 1% glacial acid mixed in DIW was added to dissolve any existing dye. The solution was centrifuged and the supernatant placed in the plate reader and scanned at 540 nm.

For the LDH, 50 μL of the corresponding SWNT concentrations (0.31 to 20 μg/mL) was added to a 96-well plate. 50 μL of LDH enzyme at 0.05 U/mL concentration was added to the SWNTs (total of 100 μL solution in each well). Two time periods were tested: one immediate and the other with 24 hour incubation to assess whether any binding occurred between the LDH enzyme and SWNTs over a longer period of time. After the appropriate incubation time, the solutions were centrifuged and the supernatant transferred to a separate 96-well plate (100 μL/well). 100 μL of the reaction mixture (11.25 mL of the diaphorase/NAD^+ mixture with 250 μL of the ready-to-use Iodotetrazolium chloride (INT) and sodium lactate dye) was added to 100 μL supernatants and the 96-well plate scanned at 500 nm. There was no statistical analysis as the experiment was only performed once.

3.3.1.2 HiPco SWNTs

Once the HMMs seeded in 48-well plates were ready, the cells were treated with HiPco SWNTs. A stock solution was prepared for only the highest concentration (20 μg/mL). Subsequent concentrations (0.31 μg/mL to 10 μg/mL) were prepared from this stock solution by diluting 1:2 with culture medium. The old culture medium was removed from the cells, and 500 μL/well of the treatment solutions were added. The cells were treated with HiPco SWNTs for 1, 2 or 4 days. The treatment solutions were removed, and the cell viability was assessed using NR, LDH, and live dead. The controls were prepared by treating cells under similar conditions but without any HiPco SWNT treatments. NR and LDH assays were performed in triplicates and

repeated 3 times, and the live dead was repeated 8 times as singletons. Statistical analysis of ANOVA with LSD and $P < 0.01$ was performed using Analyse-it®.

3.3.1.3 Unpurified and purified SWNTs

For the unpurified and purified SWNTs, stock solutions for the highest concentration (20 μg/mL) were prepared. Subsequent concentrations for both chemicals were prepared from the stock solutions by diluting 1:2 with culture medium. For both samples, the NR and LDH assays were performed in triplicates and repeated 3 times and the live dead repeated 5 times as singletons. Statistical analysis of ANOVA with LSD and $P < 0.01$ was performed using Analyse-it®.

3.3.2 Pulse chase

The pulse chase was performed similar to the MWNTs (refer to chapter 2.2.11 MWNT: Pulse chase). HMM cells were seeded on 48-well plates and treated with 5 μg/mL of unpurified MWNTs for 1 day (*pulse*). The treatment solution was removed and the cells washed 2–3 times with PBS. Fresh culture medium was added and the cells cultured for up to 14 days (*chase*), renewing culture medium every 2–3 days. Cell viability was assessed using NR (refer to chapter 2.2.6 MWNT: Cell viability assays) at various time points after the initial *pulse*: 0, 1, 2, 4, 7, 10, and 14 day. For the 0 day, cells were not washed in PBS prior to NR incubation because PBS washing frequently yielded low spectrophotometric readings. Controls were cells treated under similar conditions but without the unpurified MWNT pulse. Controls were performed in duplicates and NR in quadruplicates. Each experiment was repeated 3 times and statistically analysed with ANOVA with LSD and $P < 0.01$ using Analyse-it®.

3.3.3 Live imaging

3.3.3.1 SWNTs filled with silver iodide (AgI@SWNTs)

As SWNTs were difficult to differentiate from cells under the microscope due to their carbon and single-layer structures, one method to improve recognition was by filling the core with a reflectant metal (Figure 3.2). In this study, silver iodide (AgI) was used. J. Bendall first

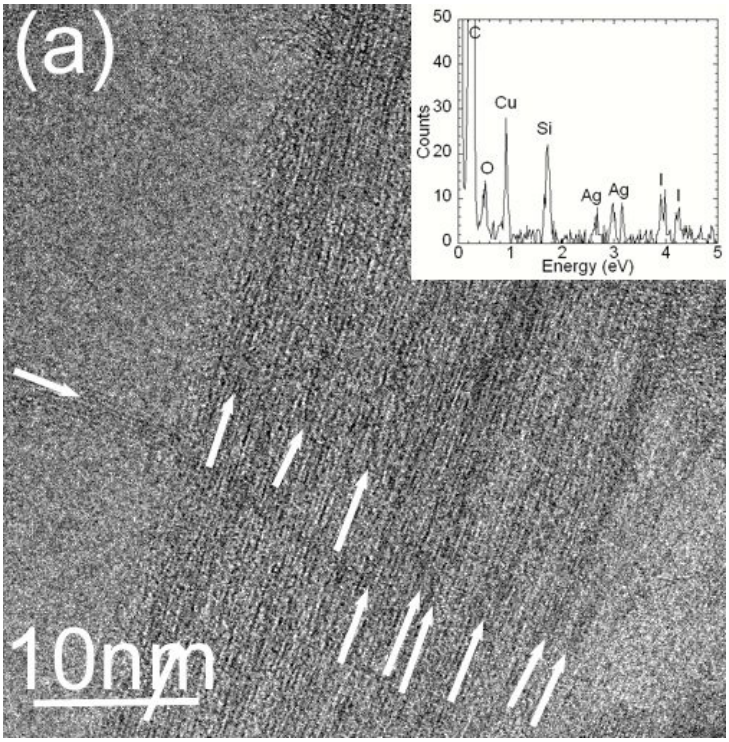

Figure 3.2: BF TEM image of HiPco SWNTs filled with AgI. The arrows indicated the individual SWNTs, and EDX confirmed the presence of AgI. (Image taken by J. Bendall [118])

purified the HiPco SWNTs (CNI) to remove unwanted material (e.g. amorphorous cafirst rbon, other carbon NPs, metal catalysts). The SWNTs were reflux-heated at 110°C in concentrated HNO_3 for 3 hours. They were then vacuum-filtered, washed and dried at 110°C for 6 hours, and allowed to oxidise in static air at 380°C for 2 hours. The sample was again reflux-heated at 110°C, but in concentrated HCl for 6 hours, vacuum-filtered, washed and dried at 110°C for 6 hours, and oxidised in static air at 400°C for 45 minutes. The SWNTs were ground together with the AgI using an agate mortar and pestle in order to mix the two substances together and to break them down into fine powders. The mixture was vacuum sealed in a quartz ampoule (backing pressure = 10^{-3} mbar) and placed in a tube furnace for 8 cycles of melting (650°C) and annealing (500°C) before a final cool down over 12 hours. The excess AgI was removed via bath-sonication as the mechanical motion caused the AgI to settle to the bottom, and the desired carbon material could be decanted from the liquid [118].

3.3.3.2 AgI@SWNTs dispersion

The AgI@SWNTs were first sterilised in ethanol and allowed to evaporate. When dispersed with BSA and PBS, many aggregates were present. Dispersing in PBS alone yielded better results. Chloroform and toulene were also assessed with chloroform yielding the best dispersion, but both solvents were extremely toxic to cells. Consequently, PBS alone was used to disperse the AgI@SWNTs. Although the SWNTs were not fully dispersed, the aggregates allowed easier identification in the confocal microscope.

3.3.3.3 Confocal microscope imaging

HMMs were seeded sparsely on 13 mm coverslips to allow imaging of individual cells rather than clusters. 6 μL/mL of Hoechst 33358 (from a 1 g/L stock solution made with PBS) was added 4–6 hours before imaging. The coverslips were then transferred to a lab-made Petri dish (refer to 2.2.6 MWNT: Cell viability assays) containing HEPES buffer to eliminate the need for CO_2. 5 μL/mL of FM4-64 (from a 3.025 μg/mL stock made with DMSO) was added. The Petri dish was placed in a temperature-controlled environment (37°C) with constant oxygen supply on a Leica SP2 confocal microscope using an HCX PL APO CS 63x 1.2 with correction lens. 5 μg/mL of AgI@SWNTs dispersed in PBS was added. Individual cells with AgI@SWNTs near the surface were located and Z-plane stacks were taken at various time intervals for 1 to 2 hours to create average projections. The AgI@SWNTs were identified using reflectance. The same protocol was used for the Leica SP1 multi-photon inverted microscope.

3.4 Results

3.4.1 SWNT characterisation

Table 3.2 summarised the characterisation of SWNTs. The average diameter of the HiPco SWNTs was slightly shorter than the unpurified and purified SWNTs. The unpurified and purified SWNTs had similar diameters which was expected as the purified SWNTs derived from the unpurified SWNTs. Unfortunately, length could not be accurately measured as the SWNTs formed bundles, causing difficulty in identifying where each nanotube began and ended.

According to the company (CNI), the HiPco SWNTs contained 5 wt% Fe. Figure 3.3 is

	Diameter (nm)	Surface Area (m^2/g)	Elemental Composition	I_D/I_G Ratio
HiPco	1.05 ± 0.16	644	5% Fe[a]	0.042
Unpurified	1.25 ± 0.23	250	30% Carbon, 70% Fe/MgO	0.092
Purified	1.24 ± 0.22	850–900	100% Carbon	0.076
Method	Raman	BET	ICP-AES	Raman

[a]Obtained from company (CNI)

Table 3.2: SWNT characterisation details as assessed by Raman spectroscopy, BET method, and ICP-AES.

a BF TEM image of individual HiPco SWNTs and bundles; EDX confirmed the presence of Fe as well as other minor contaminants. For the purified SWNTs, ICP-AES confirmed that no other contaminants were present. Figures 3.4 and 3.5 were BF TEM images of individuals and bundles of unpurified and purified SWNTs. The Fe/MgO contaminants could clearly be seen in Figure 3.4 as large round particles; EDX further confirmed their presence. Although the ICP-AES yielded 100% purity for the purified SWNTs, some Fe was still detected in the EDX (Figure 3.5).

The I_D/I_G ratios suggested increasing CNT purity as the ratio for the purified SWNTs decreased in value from 0.092 to 0.076. The higher BET value for the purified SWNTs was further confirmation as the contaminants in the unpurified SWNTs could substantially decrease BET readings. No changes in surface area or crystal structure were expected as acid-treatment was non-oxidising; any changes would require exposure to heat or nitric acid.

3.4.2 Assessment of cell viability assay interactions

Various studies have noticed that SWNTs seem to affect certain viability assays (e.g. NR, MTT, alamar Blue). For the MTT, SWNTs have been found to prevent the formazan crystals from resolubilising which inflates the toxic result and to convert the MTT into formazan without the presence of cells which deflates the toxic result [90, 91] (refer to chapter 2.4 MWNT: Discussion for details). Monteiro-Riviere et al. [36], as explained in the Introduction (chapter 1.4.1 Introduction: Cell viability assays), provided a graded system of effective viability assays and determined that the NR and an assay similar to the LDH (CytoTox One™ Homogeneous Membrane Integrity) were graded as failures. As a result, control experiments for the NR and LDH

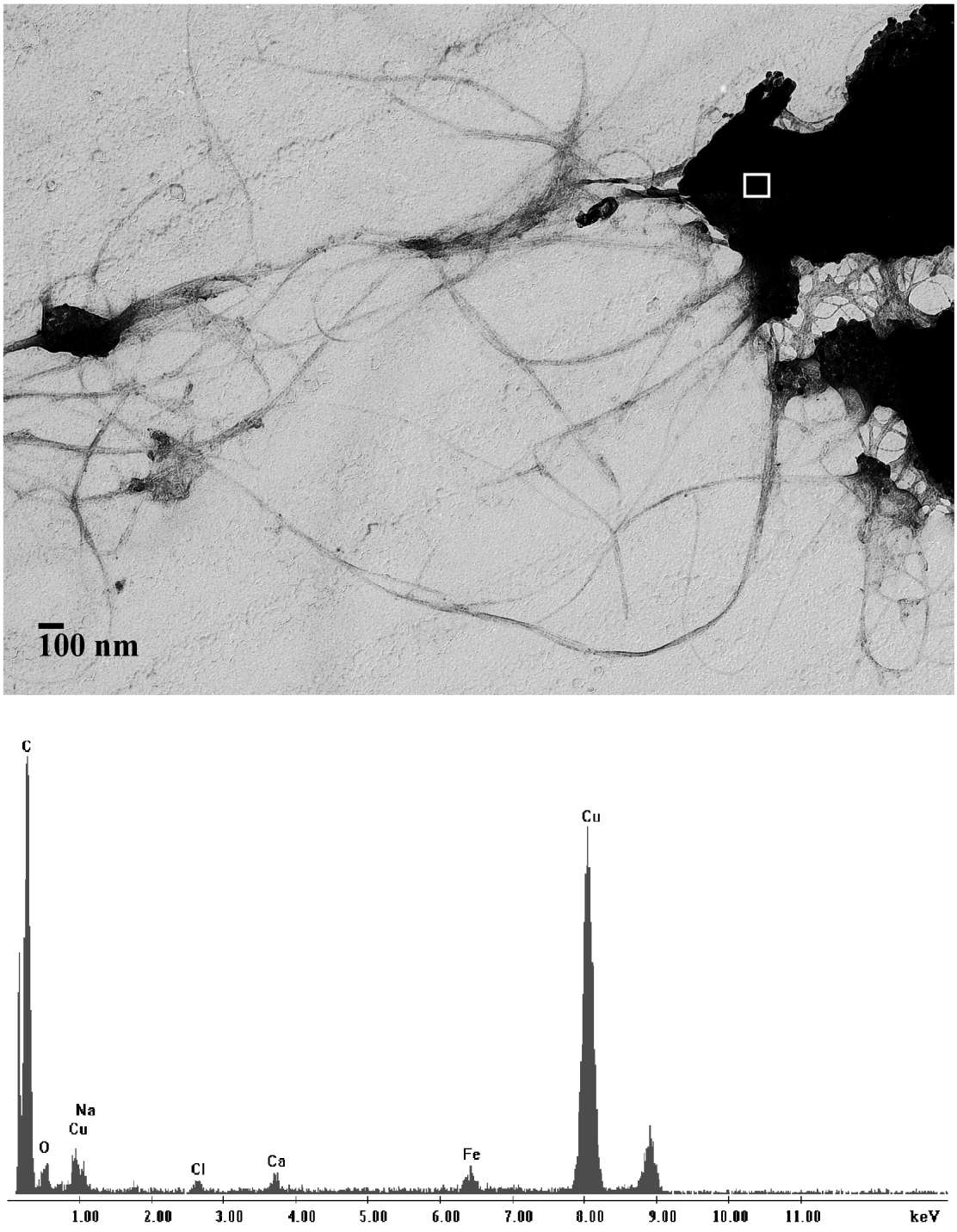

Figure 3.3: BF TEM image of HiPco SWNTs with EDX analysis. Large black areas in BF TEM image indicated bundles. A white box marked the area selected for EDX analysis. EDX analysis indicated presence of Fe and other minor contaminants. The low Fe reading was suggestive of the low Fe in the sample composition (5%) as specified by the company. The Cu was from the TEM column and imaging grid.

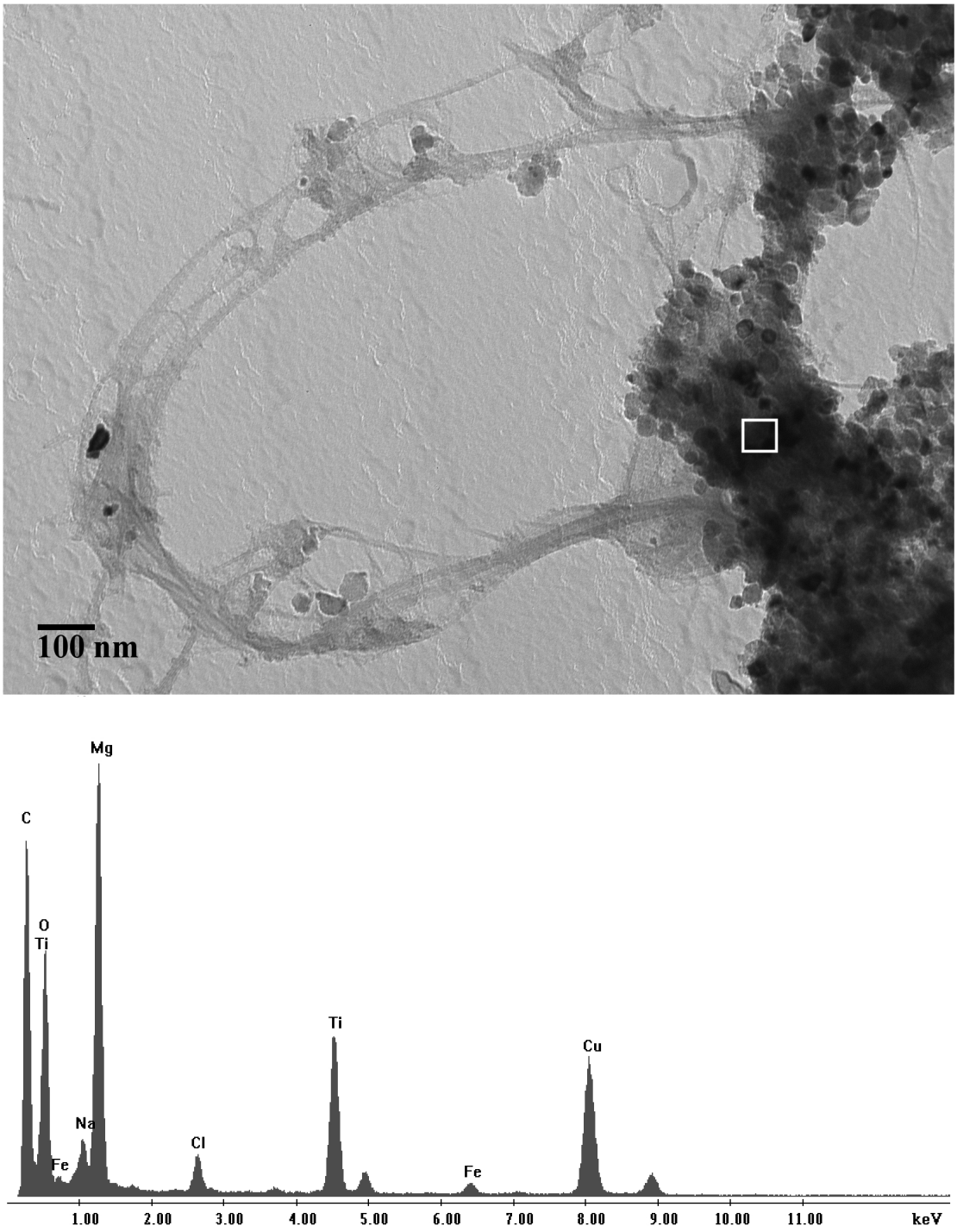

Figure 3.4: BF TEM image of unpurified SWNTs with EDX analysis. Round particles were the MgO and Fe contaminants as confirmed by the EDX analysis. A white box marked the area selected for EDX analysis. The Fe reading was lower in relation to the Mg and O because Fe NPs were surrounded by MgO. This maintained the small Fe NP size required to generate SWNTs, or else MWNTs would form from clustered Fe NPs.The Cu originated from the TEM column and imaging grid.

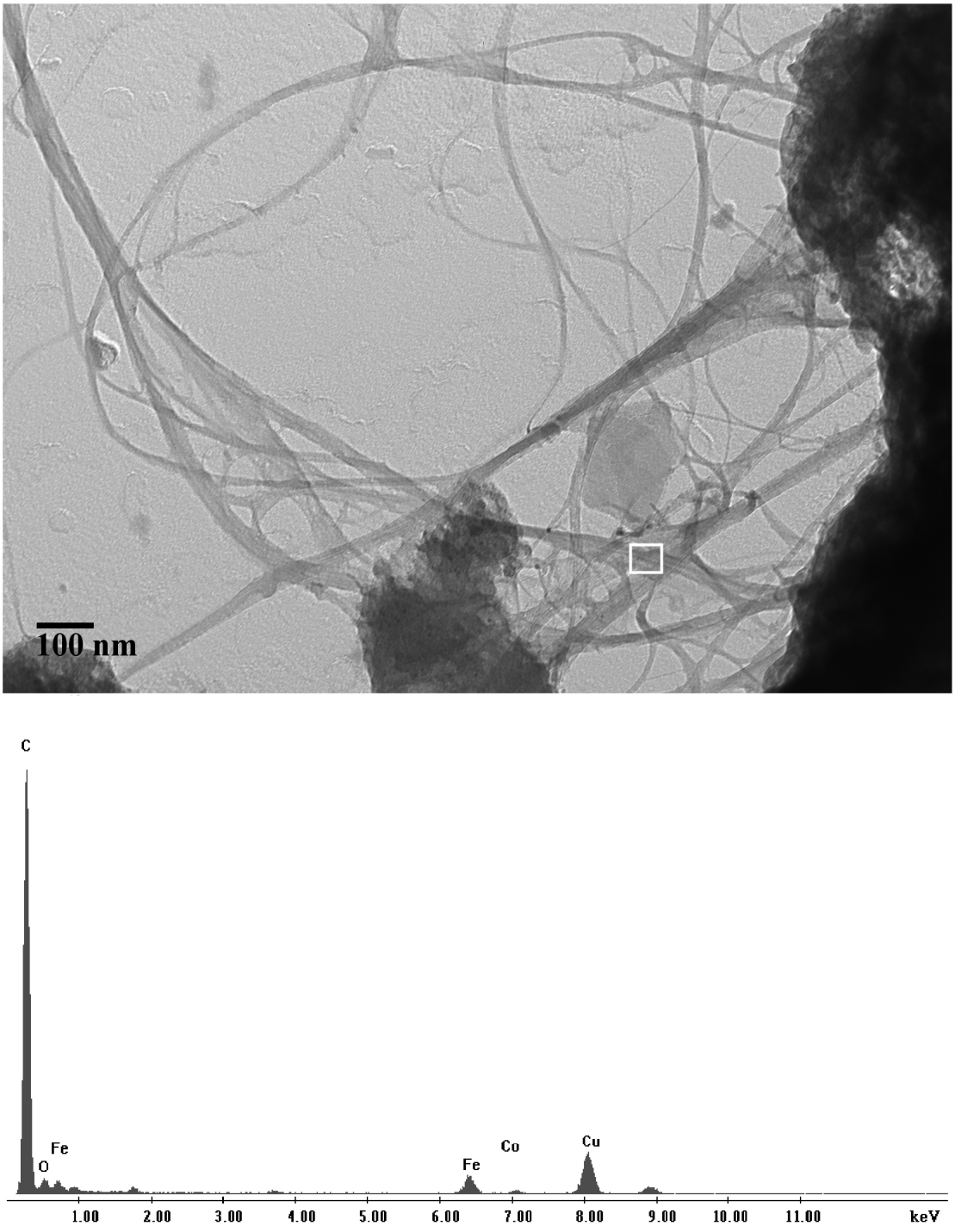

Figure 3.5: BF TEM images of purified SWNTs with EDX analysis. A white box marked the area selected for EDX analysis. Both the TEM and EDX analysis revealed evidence of some remaining Fe contaminants in the sample. The Cu in originated from the TEM column and imaging grid.

assays were performed on the HiPco and unpurified SWNTs using the same protocol as the experiments in this study but without cells present. No interactions were observed suggesting that the SWNTs had no direct effect with the assays (Figure 3.6). Purified SWNTs were not assessed as the unpurified SWNTs yielded no effects, and the purified SWNTs were derived from the unpurified SWNTs and were assumed to have similar properties. Consequently, NR and LDH were used to assess SWNT toxicity in this study, and a third assay, the live dead, which did not rely on colorimetric dyes, was used for comparison.

3.4.3 HiPco SWNTs toxicity

The HMMs were treated with HiPco SWNTs for 1, 2, and 4 days at concentrations ranging from 0.31 to 20 μg/mL. A concentration and time dependent toxicity was observed with significant toxicity found only at the highest concentration of 20 μg/mL (Figure 3.7). NR yielded 16% and 18% cell death after 2 and 4 days, respectively, while live dead yielded 7% and 14%. Significant toxicity was observed at the highest concentration of 20 μg/mL only for the NR and live dead assays. LDH enzyme release varied minimally from the control suggesting minimal damage to the plasma membrane. These results suggested that HiPco SWNTs were not acutely toxic to HMMs.

These results corresponded to the studies by Davoren et al. [112], Herzog et al. [115], and Casey et al. [119], all using HiPco SWNTs. Although the cell types (A549 human lung epithelial) and assays (CellTiterBlue, alamar Blue, Coomassie Blue, MTT) differed, none of the studies observed significant reduction in cell viability at similar concentrations.

3.4.4 Unpurified and purified SWNTs toxicity

For the unpurified and purified SWNTs, the HMMs were treated similarly for 1, 2, and 4 days at concentrations ranging from 0.31 to 20 μg/mL. No significant decrease in cell viability nor plasma membrane damage was observed for either (Figures 3.8 and 3.9). Rather, the NR assay revealed an increase in viability at various concentrations; one possible explanation was the increased uptake of NR dye due to lysosomal distension from SWNTs.

Pulskamp et al. [63] acquired similar non-cytotoxic results assessing CVD-produced SWNTs containing nickel/cobalt impurities and SWNTs that were purified with acetone. No loss of

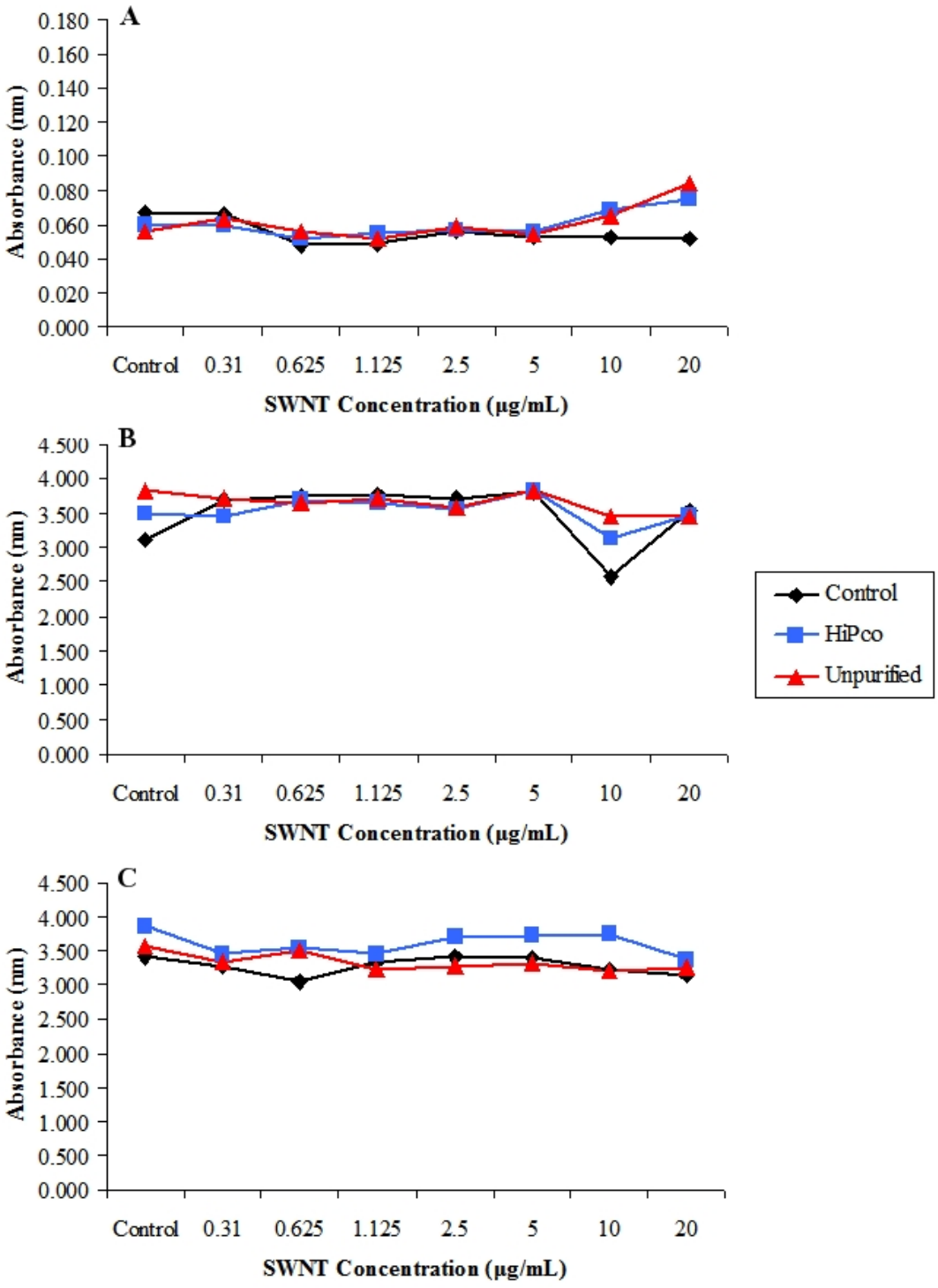

Figure 3.6: Effects of SWNTs on colorimetric dyes: A) NR, B) LDH, and C) LDH after 24 hour incubation of LDH enzyme with SWNTs. Minimal effects were observed.

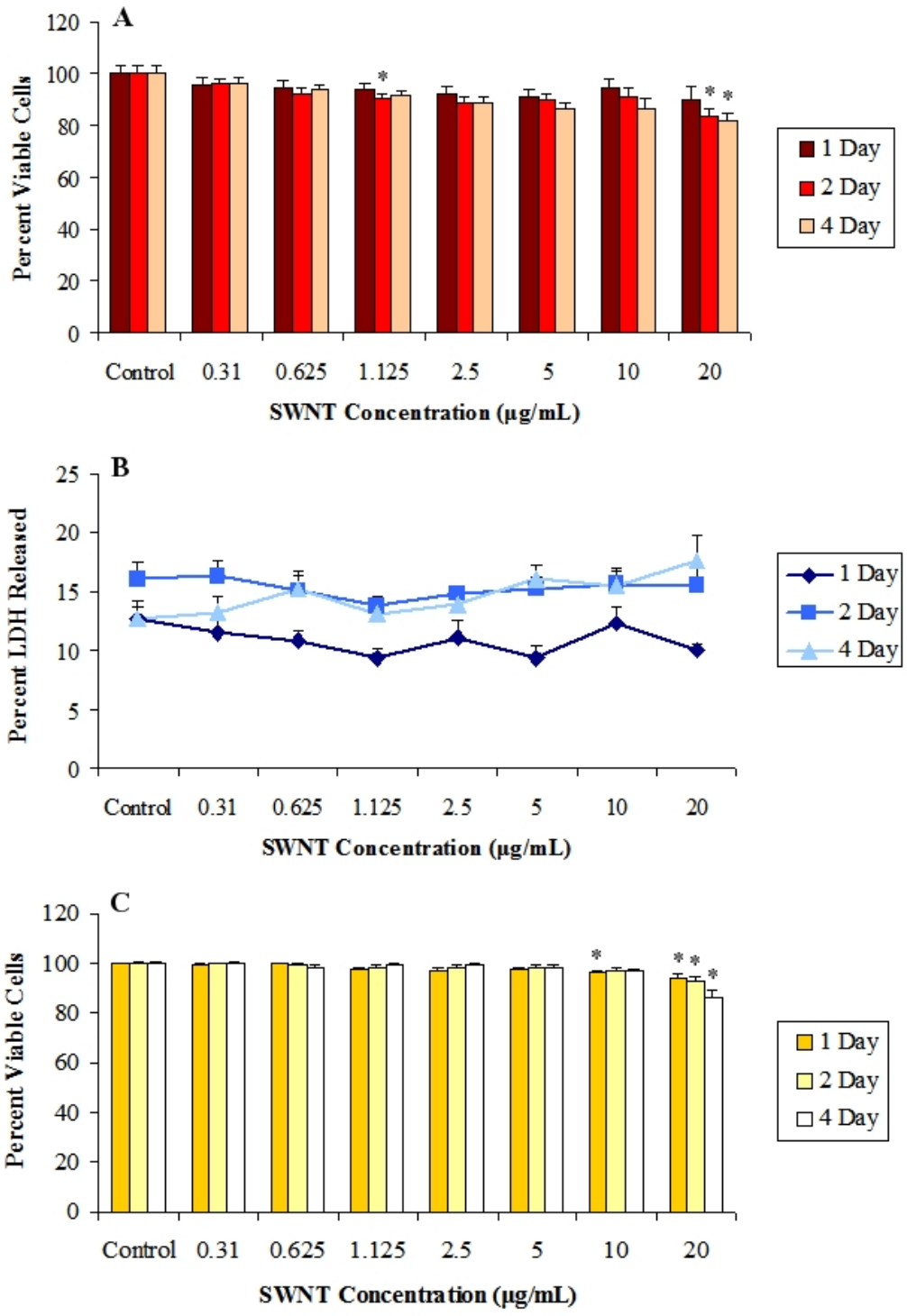

Figure 3.7: Toxicity of HiPco SWNTs after 1, 2, and 4 days based on three assays: (A) NR, (B) LDH, and (C) live dead. NR and LDH values represented the mean ± SE of three experiments each performed in triplicates; live dead values were the mean ± SE of eight individual experiments (ANOVA with LSD, $P < 0.01$, Analyse-it®). Cells treated under similar conditions but without SWNTs were used as controls. Statistical significance (*) was assessed between the concentrations and their respective controls.

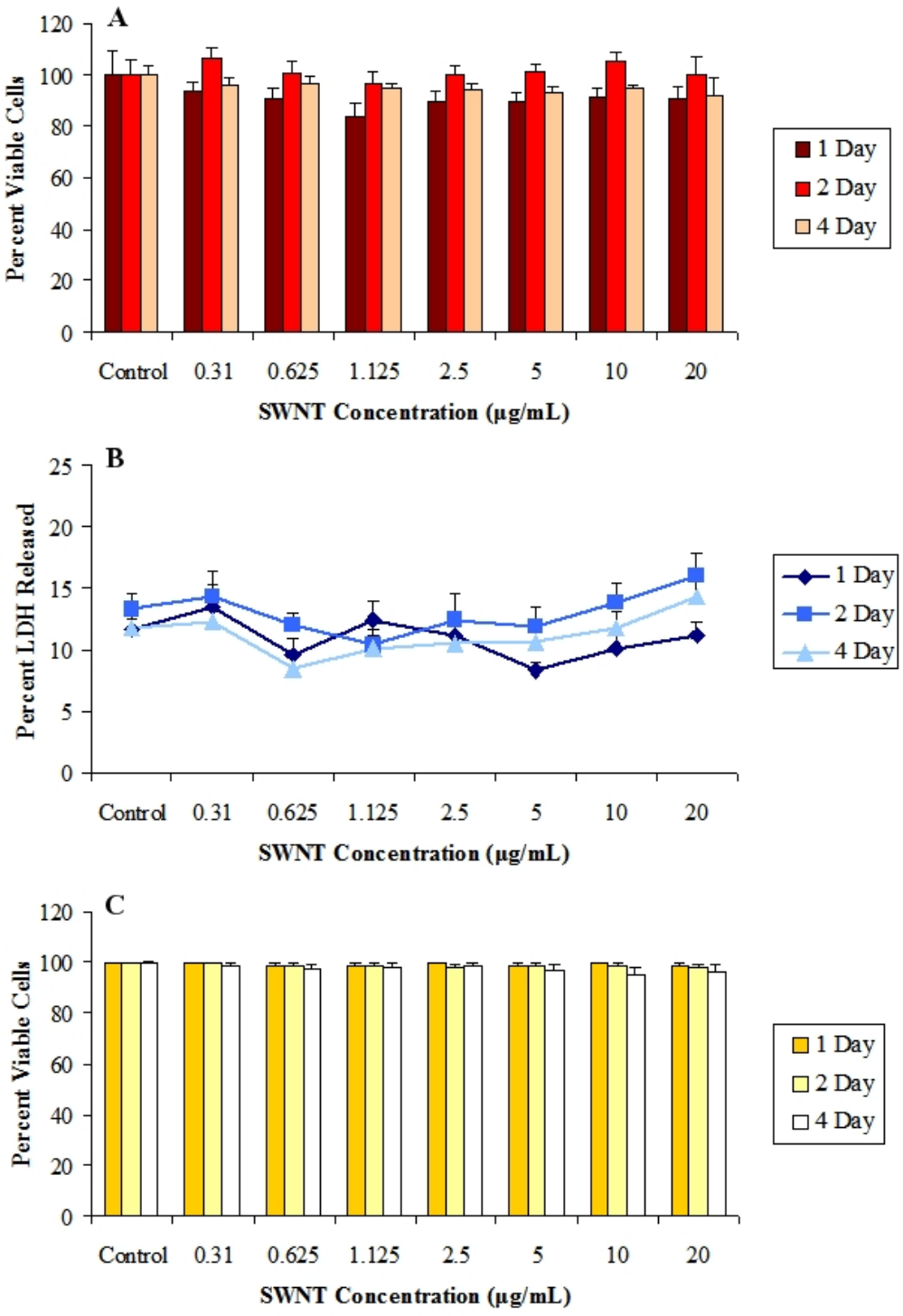

Figure 3.8: Toxicity of unpurified SWNTs after 1, 2, and 4 days based on three assays: (A) NR, (B) LDH, and (C) live dead. NR and LDH values represented the mean ± SE of three experiments each performed in triplicates; live dead values were the mean ± SE of five individual experiments (ANOVA with LSD, $P < 0.01$, Analyse-it®). Cells treated under similar conditions but without SWNTs were used as controls. No statistical significance was seen between the concentrations and their respective controls.

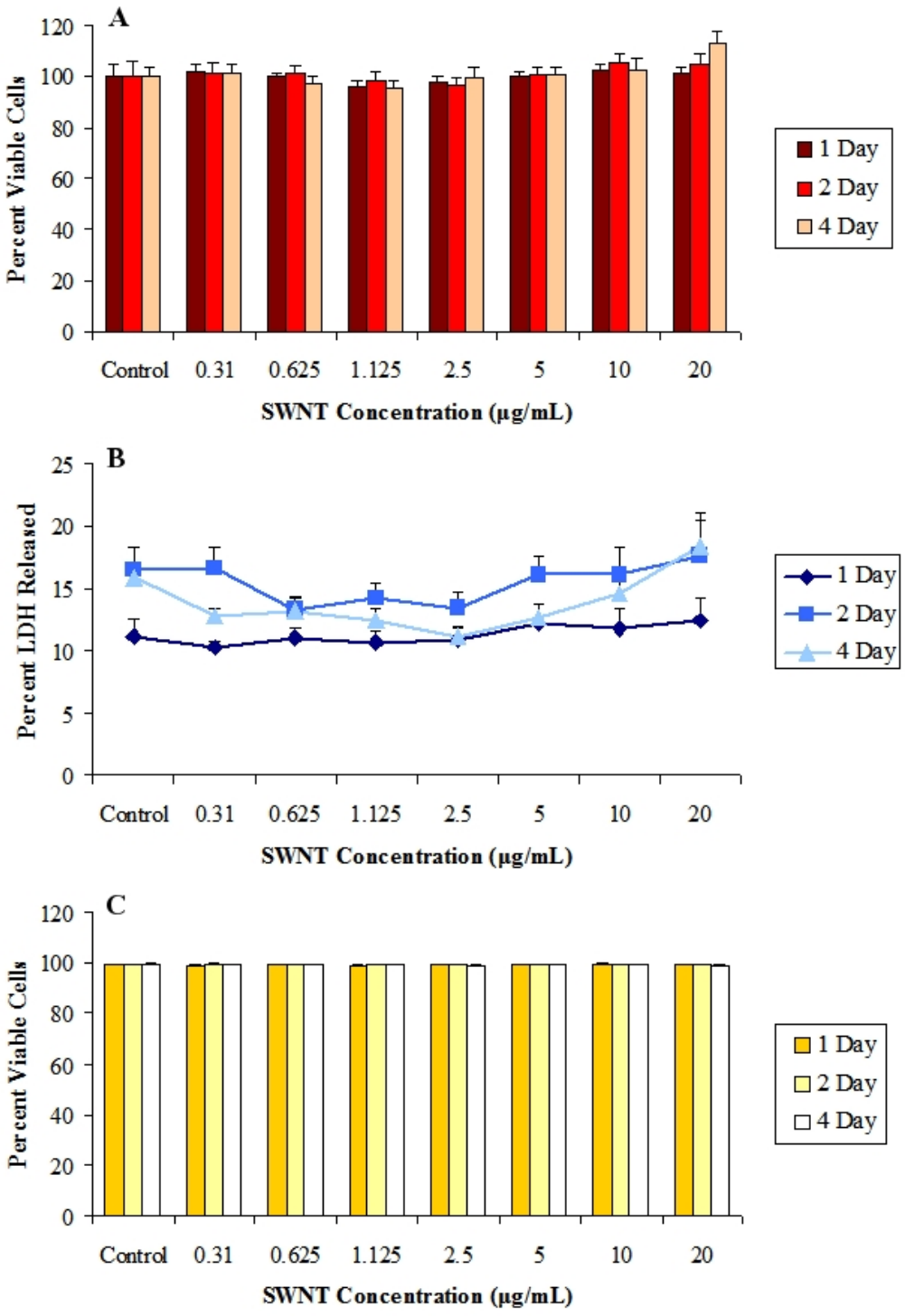

Figure 3.9: Toxicity of purified SWNTs after 1, 2, and 4 days based on three assays: (A) NR, (B) LDH, and (C) live dead. NR and LDH values represented the mean ± SE of three experiments each performed in triplicates; live dead values were the mean ± SE of five individual experiments (ANOVA with LSD, $P < 0.01$, Analyse-it®). Cells treated under similar conditions but without SWNTs were used as controls. No statistical significance was seen between the concentrations and their respective controls.

viability nor significant decrease in cell membrane integrity was observed; however, ROS generation was correlated with the presence of metal impurities. Shvedova et al. [108] found a similar correlation when assessing SWNTs with 30% iron, and the addition of a metal chelator reduced the observed toxicity. In this study, the unpurified SWNTs contained 70% Fe/MgO contaminants, and neither the unpurified nor purified SWNTs yielded significant cell death. It could be concluded that the SWNTs did not cause acute cell death, but no conclusions regarding ROS could be drawn as it was not assessed.

3.4.5 Pulse chase

Similar to the MWNTs, long term toxicity was assessed using a pulse chase. Cells were pulsed for 1 day at 5 μg/mL with HiPco, unpurified, or purified SWNTs and chased for 14 days. No significant effects were observed for any of the three types of SWNTs (Figure 3.10). This suggested that a short exposure to the SWNTs did not cause lingering effects. This could correspond to the lack of DNA damage observed by Zeni et al. [114], although Pacurari et al. [107] determined the opposite. Unfortunately, accurate comparisons between the studies were

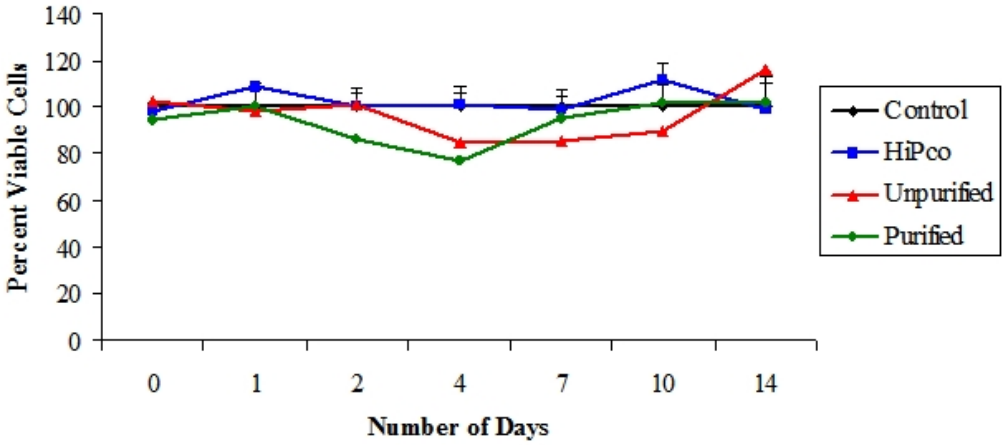

Figure 3.10: Toxicity of cells pulsed with all three SWNTs (HiPco, unpurified, and purified) at 5μg/mL for 1 day and chased for 14 days in culture medium alone. Cell viability was measured using NR. Control (cells treated under similar conditions but without SWNTs) values represented the mean ± SE of three experiments each performed in duplicates, while the treated cells represented the mean ± SE of three experiments each performed in quadruplicates (ANOVA with LSD, $P < 0.01$, Analyse-it®). No statistical significance was observed between the control and treated time points and between 0 day and all other days.

complicated by the different concentration units used (μg/mL versus μg/cm^2, respectively). Further studies into the metabolic processes are required to make any conclusive statements on the effects of SWNTs on long term toxicity.

3.4.6 Live imaging

Confocal microscopy preparation is quicker and simpler than the TEM, and cells can be kept alive during imaging. The cells can be imaged live for an extended period of time, allowing the possibility of capturing whether CNTs cross the cell membrane, where they migrate to within the cell, and if the cell remains alive or not afterwards. One complication for SWNTs is that individual and small aggregates are not visible in the confocal microscope as they are much smaller than the microscope resolution allows. Filling the SWNTs with a reflectant metal improves their visualisation although individual SWNTs are still not visible. The ability to visualise the AgI@SWNTs in the confocal microscope was confirmed by imaging the AgI@SWNTS alone using reflectance mode.

Preliminary imaging trials yielded one cell with AgI@SWNTs already present near or within the cell at the start of imaging that later died by necrosis. An influx of FM4-64 dye could be seen near the AgI@SWNTs. This suggested that the SWNTs could comprise the plasma membrane; however, this was inconclusive as the imaging resolution and dye fluorescence were fairly poor (Figure 3.11). Several other imaging trials yielded cells with no significant reactions to AgI@SWNTs at the plasma membrane barrier throughout the imaging time period, and no SWNTs were observed entering the cell. Additionally, many of the cells were in an unhealthy state before the start of imaging, possibly due to the sparse cell seeding on the coverslips.

All the preliminary trials were imaged with a Leica SP2 confocal microscope; however, the multi-photon confocal microscope was better suited for live imaging. The Leica SP2, a single photon confocal microscope, excited the fluorescent particles above and below the plane of focus while a multi-photon confocal microscope only excited at the plane of focus. This significantly reduced phototoxicity (cellular damage caused by fluorophore excitation) and photobleaching (degradation of fluorophores from excitation), allowing cells and the fluorescent particles to be imaged for an extended period of time [48]. The live imaging was trialed

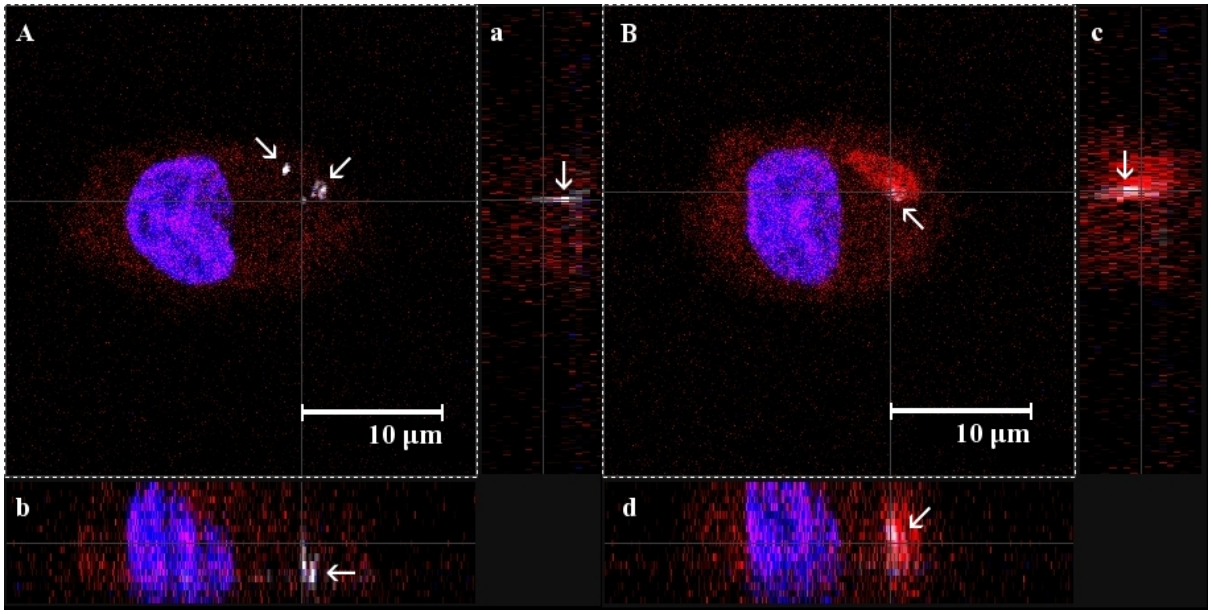

Figure 3.11: Confocal microscope average projection of a stack of images of AgI@SWNTs in HMMs: A) t = 0 min, B) t = 30 min. White arrows indicated the AgI@SWNTs. Inset A and B were XYZ axes projection with gray cross-sections pinpointing the location for the YZ (inset a and c) and XZ (inset b and d) axes projections. White reflectance in insets a–d (white arrows) showed that the AgI@SWNTs were located within the cell (blue = nucleus, red = plasma membrane, white = AgI@SWNTs).

on the Leica SP1 multi-photon confocal microscope; however, the near infrared laser source caused the SWNTs to heat and subsequently kill the cells, making the multi-photon confocal microscope unusable. With the lack of any successful trails on the single photon confocal microscope, technical difficulties such as the imaging view drifting out of focus, and inability in visualising individual SWNTs, live imaging was not pursued further. Future experiments using the TEM could be performed as the reflectant metal filling in the AgI@SWNTs should make it easier to differentiate the SWNTs from cell components.

3.5 Discussion

The characterisation data suggested that HiPco SWNTs would yield a higher BET value than the purified SWNTs since surface area increases with decreasing diameter; however, the bundle sizes could affect the BET value because larger bundles would prevent the nitrogen gas

from accessing individual nanotubes properly and lower the surface area adsorption readings. Secondly, the purified SWNTs were expected to yield the lowest I_D/I_G ratio since decreasing ratios suggest increasing purity. Several factors could have contributed to the unexpected results. The G-peak value could be affected by nanotube orientation; if a substantial amount of nanotubes were aligned parallel to the polarised direction of the Raman laser, the G-peak would increase, thereby decreasing the I_D/I_G ratio. Although length could not be determined for any of the SWNTs, the unpurified and purified SWNTs might be shorter than the HiPco since the catalyst for the unpurified and purified SWNTs was designed to produce 1 μm long SWNTs. Shorter SWNTs signified more nanotube ends which would increase defective sites if they were not properly capped; such defects would yield higher I_D/I_G ratios. Additionally, the different methods of SWNT synthesis could affect the outcome of the ratio.

As Worle-Knirsch et al. [90] and Casey et al. [91] found that SWNTs interfered with the MTT assay, the LDH assay was used instead. However, two later studies found that SWNTs could also affect the LDH assay. Pacurari et al. [107] used the same LDH assay as this study in which LDH release was measured via the enzymatic conversion of tetrazolium salt INT into formazan and found that SWNTs adsorbed the LDH enzyme; this caused the LDH release to decrease with increasing concentration. The assay used by Monteiro-Riviere et al. [36] measured LDH release by the enzymatic conversion of reasuzurin to resorufin; no direct interaction between the SWNTs and the assay was indicated, but results yielded large error bars indicating highly variable results. Although these two studies observed that SWNTs could influence the LDH assay, control experiments in this study found no direct interferences; further trials were required for statistical analysis to determine variability. As Monteiro-Riviere et al. suggested, several assays were used in this study to assess the toxicity of the SWNTs; the live dead assay provided a form of viability assessment that did not rely on colorimetric dyes. All three assays correlated fairly well, although the NR and LDH did show greater variability than the live dead.

Of the three SWNT NPs, only the HiPco SWNTs exhibited an observable dose and time dependent toxicity. No significant toxicity was found for the unpurified or purified SWNTs. These results suggested that SWNTs were not acutely toxic. Furthermore, as the LDH assay assessed plasma membrane leakage, no significantly different values suggested that SWNTs did not cause plasma membrane damage. The percentages of cell death correlated with several other studies [63, 106, 112], but higher concentrations were also used, and toxicity increased

with increasing concentration. As the concentration range used in this study was chosen to compare with the MWNTs, higher concentrations could determine whether toxicity would also increase as observed in the other studies.

For the unpurified SWNTs, 70% of the sample was composed of Fe and MgO while the purified SWNTs contained no contaminants. The lack of toxicity observed for both the unpurified and purified SWNTs suggested that neither the Fe and MgO nor the SWNTs themselves caused cell death. Contrarily, the HiPco SWNTs, which contained up to 5 wt% Fe, yielded greater toxicity. Two studies compared cell death with ROS generation from metal contaminants and drew opposing conclusions. Shvedova et al. [108] observed significant ROS generation but comparable levels of cell death, while Herzog et al. [120] found no significant ROS generation and no correlation with cell death. Herzog et al. proposed that the iron contaminants in HiPco SWNTs were enclosed within the nanotube tips and were not bioavailable. They further suggested that the fetal bovine serum (FBS) used in the culture medium induced a protective effect against oxidative stress. The higher iron content and treatment concentrations used by Shvedova et al. might explain the ROS generation observed. Furthermore, Shvedova et al. used electron spin resonance to determine free radical presence, chemiluminescence for antioxidant response against peroxyl radicals, and 2-thiobarbituric acid for lipid peroxidation while Herzog et al. only used the carboxy-DCFDA assay which assessed the presence of hydrogen peroxide, peroxyl radicals, and peroxynitrite anions. As this study did not assess ROS generation, it would be interesting to determine whether ROS were generated by using similar assays as these two studies and if any differences existed between the SWNTs.

Aggregates could be observed when the SWNTs were dispersed in culture medium alone. As mentioned in the MWNT chapter (2.4 MWNT: Conclusion), conclusions contradicted as to whether aggregates increased or decreased toxicity. *In vivo*, large aggregates trapped along alveolar walls or capillaries could cause granuloma formation while *in vitro*, they may be too large to affect the cells. Instead, individual CNTs would be able to enter cells more easily and cause more damage. No analyses were made on the degree of dispersion between the three different SWNTs in this study. Although little to no cytototoxicity was observed, further studies could determine whether dispersion had an effect on SWNT cytotoxic potential. Additionally, the lack of toxicity suggested that no interactions existed between the SWNTs and the nutrients in the culture medium. No significant changes in medium colour were observed which was

contrary to the results by Guo et al. [111]; however, the SWNT concentration used (80 μg/mL) was much higher than this study (20 μg/mL) and the type of culture medium (RPMI) was different. The lack of medium interaction can be confirmed in the future using HPLC as assessed by Guo et al.

Even though SWNTs were found to be not toxic, analysing their localisation and interaction within the cell could further explain their effects toward cells. An attempt was made using confocal microscopy; however, the SWNT size was below the resolution limitation, and only bundles could be seen. BF TEM was not sufficient as SWNTs were difficult to discern from cell components. Porter et al. [121] reported that energy filtered TEM (EFTEM) and high angle annular dark field scanning TEM (HAADF-STEM) were effective in observing SWNTs in HMM cells. Future studies using these techniques are required to determine if and where SWNTs are internalised, the mechanism of uptake, and what happens after internalisation in order to fully understand the interaction between SWNTs and cells.

In the study by Porter et al. [121], HMM cells were treated with 0–10 μg/mL of SWNTs for 2 or 4 days, and SWNTs were observed in the nucleus, suggesting that SWNTs could cause genotoxicity if they interact with the DNA. The pulse chase in this study indicated that the SWNTs did not cause long term effects to viability; however, as with the MWNTs, further studies directly assessing whether SWNTs damage DNA or chromosomes are required to determine if SWNTs do cause genotoxicity.

3.6 Conclusion

HiPco SWNTs yielded a dose and time dependent toxicity with significant toxicity only at the highest concentration (20 μg/mL). The unpurified and purified SWNTs yielded no toxicity. This was the first time that SWNTs filled with a reflectant metal were used to enhance their identification in the confocal microscope (as opposed to SWNTs functionalised with fluorescent probes). At these concentrations, the results concluded that SWNTs were not acutely cytotoxic.

Chapter 4

ZnO

4.1 Introduction

Zinc is a naturally-occurring metal found in the Earth's crust, rocks, minerals, and soil. It is commonly used in alloys, paint coatings, and as protective coatings for other metals. Zinc is also an essential nutrient for humans with a recommended daily allowance of 15 mg/day [122]. It acts as a catalyst for over 300 enzymes as well as structural or regulatory ions for enzymes, proteins, and transcription factors [123]. In the brain, zinc maintains normal neurological functions as it regulates synaptic transmissions and memory formation [124]. Additionally, zinc contributes to DNA synthesis, membrane metabolism, and cell growth and division. Deficiencies can result in infections, skin disease, delayed wound healing, impaired immune function, growth retardation, and cancer whilst over-exposure can lead to gastrointestinal damage, anemia, pancreatic damage, and a decrease in high-density lipoprotein (HDL) [122].

In nanotechnology, zinc oxide (ZnO) has gained significant interest with its semiconducting property, high surface area, transparency, resistance to radiation, and unique electrical, optical, and photonic properties. Potential applications include field-effect transistors [125], liquid crystal displays [126], light emitting diodes [127], solar cells [128], biological and gas sensors [129], and pollutant filters in air and water [130]. Its broad ultraviolet (UV) absorption spectrum (covering both UV A and B radiation) and low refractive index has contributed to its extensive application in cosmetics and sunscreens [131, 132]. Additionally, ZnO has been found to protect against intestinal diseases, promote healing, and resist against bacterial

infection promoting its application in many antimicrobial products [133, 134].

In industrial applications, workers exposed to ZnO have developed the flu-like illness "metal fume fever," a pulmonary inflammatory response caused by inhaling metal oxide fumes. This has been characterised by coughs, thirst, a metallic taste, salivation, fever, headache, myalgia, fatigue, dyspnea, and neutrophil leucocytosis (higher than normal level of neutrophil leukocytes in the blood), although symptoms are reversible within 1 to 4 days after cessation of exposure [122, 135]. The US has set the permissible exposure limit to 5.0 mg/m^3[136], although one study has still found cases of metal fume fever within this limit when thirteen human subjects were exposed to 5.0 mg/m^3 of ZnO fume for 2 hours [137]. Table 4.1 summarised the details of some of the papers discussed in this chapter.

Following the addition of ZnO into cosmetics and sunscreen, studies investigated whether topical exposure can lead to health effects. A number of earlier studies found that ZnO could penetrate the skin. Hallmans et al. [138] detected zinc in the blood and tissues of rats after ZnO application to their skin. Zinc was found mainly in the dermis and panniculus carnosus (muscle tissue) with the greatest concentration around the epidermis and hair follicles. Agren et al. [139] applied ZnO via an occlusive dressing for 2 days on human skin and detected zinc in the epidermis, blister fluid, and dermis. Despite evidence of zinc penetration from these earlier studies, more recent studies indicated that ZnO remained in the stratum corneum and hair follicle roots and did not penetrate into the deeper layers of the skin. Gamer et al. [140] was able to retrieve all of the zinc that was applied onto porcine skin for 48 hours. Zvyagin et al. [8] found that the ZnO NPs remained on the stratum corneum, collecting mainly in the skin folds and hair follicles. Although results were contradictory, the prevailing lack of evidence of ZnO skin penetration suggested that topical exposure was not a likely source of toxicity.

In vitro, studies assessed the toxic potential of ZnO and compared it with other metal NPs (TiO_2, Fe_2O_3, Al_2O_3, CrO_3) only to discover that ZnO appeared to be the most toxic:

- Jeng et al. [141] found that 10–100 μg/mL of ZnO treated on mouse neuroblastoma (Neuro-2A) cells for 48 hours caused concentration dependent cell death (50% at the highest concentration), concentration dependent mitochondrial damage (80% at the highest concentration), and significant LDH release (nearly 100% after 70 hours at 50 μg/mL).

- Lin et al. [142] concluded that human lung epithelial cells treated with 8–25 μg/mL of

Table 4.1: Summary of experimental details of some of the ZnO papers discussed in chapter.

	Materials	Size	Dispersant	Model	Conc	Time	Assay	Results
Fine	ZnO fume			Humans	5 mg/m3	2 hrs		Fever, myalgias, cough, fatigue, and increased IL-6
Hallmans				Rat skin	125 ug/mL Zn			Found in dermis & panniculus carnosus; most concentrated near epidermis and hair follicles
Agren	ZnO (25%) occlusive dressing			Humans	5 ug/cm2/hr	48 hrs		Found increased Zn in epidermis, blister fluid, and dermis
Gamer		< 160 nm (mean 80 nm)	Oil/water emulsion	Pig skin	400 ug/cm2	24 hrs	Tape strip	Recovered all of applied zinc
Zvyagin		20-30 nm		In vivo human skin			Multiphoton, SEM, EDX	Remained in stratum corneum, accumulated in skin folds & hair follicles
Jeng		50-70 nm	DIW	Mouse neuroblastoma (Neuro-2A)	10, 25, 50, 100 ug/mL	24 hrs	Trypan blue, MTT, LDH	ZnO most toxic: dose dependent cell death, dose dependent mitochondrial damage, significant LDH release; gradual rate of cell death
Lin		70±13 nm	Culture medium	A549	8, 10, 18, 25 ug/mL	6, 12, 24 hrs	Sulforhodamine B, LDH	ZnO most toxic: dose and time dependent, steep decline between 10-18 ug/mL; rate of death increases with longer exposure
		420±269 nm						
Dani			Culture medium	Neuro-2A	10, 50, 100, 300 uM	4, 12, 24 hrs	DCDHF	Increased DCDHF fluorescence = ROS
Xia	ZnO	13 nm	Culture medium	Mouse leukemic macrophage (RAW 264.7), human bronchial epithelial (BEAS-2B)	25 ug/mL	24 hrs	DCF, JC-1 fluorescence	Induce H2O2 & O2-, decrease mitochondria membrane potential
							ICP-MS	190-225 uM maximum dissolved zinc in culture media, >80% zinc dissolution in 3 hrs
	ZnSO4				12.5, 25, 50 ug/mL	6 hrs	PI	Toxicity due to ZnO dissolution & solid NPs
Sharma		30 nm	Culture medium	Human epidermal (A431)	0.008-20 ug/mL	6 hrs	Comet assay	Dose dependent DNA damage
						3, 6, 24, 48 hrs	MTT, LDH, NR	Dose and time dependent toxicity; concentration of accelerated death lowers with longer exposure

	Materials	Size	Dispersant	Model	Conc	Time	Assay	Results
Franklin	nanopart-iculate	30 nm	Teric N30		100 mg/L	up to 72 hrs	Dialysis	19% of maximum dissolved zinc possible
	bulk							
	ZnCl2			*P. subcapitata*	10, 50, 100 mg/mL	20, 40, 60, 80 hrs	Cell counting via FACS	Toxicity due to dissolved zinc
Heinlaan	NP	50-70 nm	Culture medium	*V. fischeri*	0.2, 0.4, 0.6, 0.8 ug/mL	2 hrs	Flash assay, Sensor bacteria	Toxicity partially from zinc dissolution (affected by limited solubility); zinc dissolution similar for NP and bulk; toxicity of both 6 times < ZnSO4
	bulk							
	ZnSO4							
Deng		10 nm	Culture medium	Mouse neural stem (NSC)	3, 6, 12, 18, 24 ug/mL	24 hrs	WST-8	Dose dependent toxicity with accelerated death after 12 ug/mL
		30 nm						
		60 nm						
		200 nm						
Yang	NP	L: 200 nm D: 50 nm	Simulated uterine solution		2 mg	up to 850 hrs	Absorbance	ZnO NP (95% @ 50 hrs) released Zn2+ faster than microparticle (85% @ 250 hrs)
	micropart-icle	1 um						

ZnO for 6–24 hours yielded a concentration and time dependent toxicity (85% at the highest concentration) with a steep increase in cell death between 8 and 10 μg/mL.

The observed dose dependent toxicity has been attributed to ROS oxidative stress, and mitochondrial damage, and DNA damage:

- Daniels et al. [143] observed increased DCDHF fluorescence in mouse neuroblastoma (Neuro-2A) cells treated with 10–300 μM ZnO indicating presence of ROS.
- Xia et al. [144] identified the ROS species as H_2O_2 and O_2^- in mouse leukemic macrophages cells treated with 25 μg/mL of ZnO for 24 hours. They also detected decreased mitochondria membrane potential.
- Sharma et al. [145] found that human epidermal cells treated with 0.008–20 μg/mL of ZnO for 6 hours caused a concentration dependent increase in DNA damage.

Clearly, all these studies indicated that ZnO was highly toxic. One potential source implicated for the observed toxicity was ZnO dissolution:

- Franklin et al. [146] proposed that cell death was mainly contributed by the dissolved zinc. They first determined the dissolution rate and percentage of zinc from bulk and

nanoparticulate ZnO using dialysis and found that, after 72 hours, only 19% of the maximum concentration of zinc was dissolved for both samples. The bacteria *P. subcapitata* was treated with 10–100 μg/mL of ZnO for up to 80 hours and the toxic curve compared to $ZnCl_2$, a chemical known to readily dissolve into Zn^{2+} and Cl^{2-}; the graphs nearly corresponded fully, implicating the role of dissolved zinc.

- Heinlaan et al. [147], on the other hand, suggested that zinc dissolution only contributed partially to the observed toxicity. They similarly concluded that both bulk and nanoparticulate ZnO released comparable levels of Zn^{2+}, although it was ~83% release (a recombinant sensor bacteria was used rather than dialysis). Both ZnO particles were compared with $ZnSO_4$, another chemical known to readily dissolve into Zn^{2+} and $SO_4{}^{2-}$, in *V. fischeri* bacteria and found to be 6 times less toxic than the reference substance $ZnSO_4$. The authors proposed that the difference was due to the limited solubility of ZnO NPs, which would decrease the amount of dissolved zinc ions.

- Xia et al. [144] similarly used $ZnSO_4$ but suggested that ZnO toxicity was due to both dissolved zinc and solid ZnO NPs. The maximum concentration of dissolved zinc from ZnO in culture media—190 μM for BEGM (BEAS-2B cells) and 225 μM for DMEM (RAW 264.7 cells)—was determined to be lower than $ZnSO_4$. ZnO reached > 80% zinc dissolution in culture media within 3 hours, suggesting that using < 80% of the 190–225 μM maximum dissolved zinc concentration should result in only zinc and oxide particles and no solid ZnO NPs. At such lowered concentrations, ZnO yielded less toxicity than $ZnSO_4$, and at higher concentrations where both dissolved zinc and ZnO solid NPs were present, ZnO exhibited an acceleration in cell death. Such contradictory results led the authors to conclude that solid ZnO NPs may contribute to cell death.

All three studies determined that ZnO released less Zn^{2+} ions than the reference chemicals that readily released their Zn^{2+} ions ($ZnCl_2$ and $ZnSO_4$). Franklin et al. detected the least release from ZnO, although different assessment methods were used in each study. Regardless of the differences, these studies implicated the contribution of zinc dissolution to ZnO toxicity. The extent of its contribution, however, remained uncertain.

As the potential applications for ZnO continue to grow, deducing the seemingly toxic implications becomes essential. With nanotechnologists using ZnO as building blocks for other

nanostructures such as ZnO nanowires, assessing how ZnO itself causes cellular effects may help in understanding any possible toxic effects of ZnO nanostructures. This study seeks to use similar experimental techniques as the CNTs in the previous two chapters in analysing ZnO nanopowders in hopes of contributing to the assessment of ZnO nanowire toxicity for future comparison with the CNTs.

4.2 Materials and methods

4.2.1 ZnO nanopowder production

Two types of 100 nm-sized ZnO nanopowders were purchased from Meliorum Technologies, Inc: uncoated and PVA (polyvinyl alcohol) coated. PVA is a copolymer that can dissolve in aqueous solutions and has been developed into a coating agent [148]; therefore, the PVA coating should improve ZnO nanopowder dispersion. According to the company, the nanopowders were produced by a combination of wet chemistry and flame spray pyrolysis. For the wet chemistry, zinc ions were reduced from $ZnCl_2$ using ammonia or sodium borohydride. The zinc ions were then oxidized into ZnO precipitates in an oxygen-rich environment (e.g. water or oxygen gas). The ZnO precipitate (*precursor*) was dispersed into the flame spray pyrolysis as micron-sized droplets. The flame evaporated the droplets and ignited the combustion with an oxidant to generate ZnO nanopowders [149, 150].

4.2.2 ZnO characterisation methods

4.2.2.1 Length

BF TEM images were taken by evaporating a few droplets of uncoated or PVA-coated ZnO nanopowders dispersed in ethanol on TEM grids. The long and short dimensional lengths were determined by individually measuring 2000 NPs for each ZnO nanopowder sample using ImageJ.

4.2.2.2 ICP-AES

ICP-AES analysis was performed by Warwick Analytical Services.

4.2.2.3 Aggregation

Analysis on the Malvern Nanosizer (Malvern Instruments Ltd) was performed by E. Thompson. 50 μg/ml of both samples were dispersed in de-ionised water, and 1 mL of each sample was placed in a disposable curvette for analysis. After an intial analysis, the samples were centrifuged at 1500 x g for 5 minutes to remove aggregates and the supernatant measured.

For the SEM, both ZnO nanopowders were dissolved in de-ionised water and allowed to evaporate on Formvar-coated copper grids. The grids were attached onto SEM stubs and coated with a thin layer of gold. 100 aggregates for each of the uncoated and PVA-coated ZnO nanopowders were individually measured using ImageJ.

4.2.2.4 Raman spectroscopy

Each nanopowder was placed on a coverslide and the Raman spectrum taken by J. Bendall with an excitation of 633 nm.

4.2.2.5 Photoluminescence

Each nanopowder was dispersed in ethanol and sonicated for 15 minutes. Solution was placed on a silicon wafer and allowed to evaporate before analysation in a HORIBA Jobin Yvon FluoroLog®-3 spectrofluorometer was performed by J. Bendall.

4.2.3 Cell viability assays

HMM cells were prepared according to chapter 2.2.4 (MWNT: HMM isolation), and three different assays were used to assess cell viability: NR, LDH, and live dead. Refer to chapter 2.2.6 (MWNT: Cell viability assays) for NR and live dead protocols and chapter 3.3.1 (SWNT: Cell viability assays) for LDH protocol.

4.2.3.1 Assessment of potential interactions between assay dyes

For the NR, the same protocol as the MWNTs was used (refer to chapter 2.2.6.1 MWNT: Assessment of potential interactions between assay dyes and unpurified MWNTs), and for the LDH, the same protocol as the SWNTs was used (refer to chapter 3.3.1 SWNT: Assessment of potential interactions between assay dyes and SWNTs).

4.2.3.2 ZnO nanopowder toxicity

HMM cells were grown in 48-well plates. Both ZnO nanopowders were first sterilised in ethanol and the ethanol allowed to evaporate. Stock solutions in culture medium were prepared for only the highest concentration (50 μg/mL). Subsequent concentrations (1.56 μg/mL to 25 μg/mL) were prepared from this stock solution by diluting 1:2 with culture medium. The old culture medium was removed from the cells, and 500 μL/well of the treatment solutions were added for 24 hours. The treatment solutions were removed, and the cell viability was assessed using NR, LDH, and live dead. The controls were prepared by treating cells under similar conditions but without any ZnO nanopowder treatments. NR and LDH assays were performed in triplicates and repeated 3 times, and the live dead was repeated 5 times as singletons. Statistical analysis of ANOVA with LSD and $P < 0.01$ was performed using Analyse-it®.

4.2.4 ZnO dissolution

$ZnCl_2$ toxicity was assessed by K. H. Müller. HMM cells were seeded in 48-well plates and treated with concentrations of $ZnCl_2$that contained equivalent amounts of Zn^{2+} as the ZnO nanopowder concentrations (i.e. 65 μg/mL $ZnCl_2$ for 50 μg/mL ZnO—both concentrations contained 40 μg/mL Zn^{2+}). The old culture medium was removed from the cells, and 500 μL/well of the treatment solutions were added for 24 hours. The treatment solutions were removed, and the cell viability was assessed using NR. The controls were prepared by treating cells under similar conditions but without any $ZnCl_2$ treatments. The experiments were performed in triplicates and repeated 3 times. Statistical analysis of ANOVA with LSD and $P < 0.01$ was performed using Analyse-it®. The NR results for the uncoated and PVA-coated ZnO nanopowders were taken from the toxicity assays (refer to section 4.2.3.2 ZnO nanopowder toxicity).

ICP-OES (or ICP-AES) analysis was performed by M. Motskin. Extracellular, intracellular, and lysosomal buffers were made according to Table 4.2; culture medium was also used in the comparison. Both uncoated and PVA-coated ZnO were dispersed in the various buffers for 24 hours at a concentration of 200 μg/mL. Solutions were then compared to zinc calibration standards to determine the amount of zinc present in each buffer. Refer to chapter 2.2.3 MWNT: MWNT characterisation for ICP-AES details.

	$CaCl_2$	$MgCl_2$	KCl	NaCl	Glucose	Buffer (25 mM)	pH
Extracellular	1 mM	1 mM	5.8 mM	141.8 mM	5.6 mM	HEPES-KOH	7.2
Intracellular		1 mM	142 mM	5 mM	5.6 mM	HEPES-NaOH	7.2
Lysosomal	500 μm	1 mM	200 mM			Mes-NaOH	5.0
Culture Medium							7.4

Table 4.2: Ingredient composition of cellular buffers used for the ICP-OES analyses of ZnO nanopowder dissolution. No ingredient compositions for the culture medium were included as the company (Invitrogen) did not provide any. Information synthesised from M. Motskin.

4.2.5 Confocal microscopy

HMM cells were grown on 13 mm coverslips and treated with 6 μg/mL of uncoated ZnO nanopowder at 37°C for 1 day. The treatment solution was removed, coverslips washed with 2–3 times with PBS, and fresh culture medium added prior to imaging. The coverslip were transferred to a lab-made petri dish (refer to chapter 2.2.6 Cell viability assays). 6 μL/mL of Hoechst 33358 (from a 1 g/L stock solution made with PBS) was added 4–6 hours and Calcein AM (1 μL/mL from a stock of 50 μg diluted in 100 μL DMSO) immediately prior to confocal microscope imaging to identify the nuclei and cytoplasm of living cells, respectively. The uncoated ZnO nanopowders were identified via reflectance imaging. Z-plane stacks were taken with a Leica SP2 confocal microscope using a HCX PL APO CS 63x 1.2 with coverslip thickness correction lens to create an average projection.

4.2.6 TEM

Chapter 2.3.3.1 (MWNT: Results and Discussion) provided the detailed embedding protocol, although one change was made: cells were treated with 1% osmium tetroxide only (without 1.5% potassium ferricyanide and 2 mmol/L calcium chloride) as it was difficult to differentiate between the potassium ferricyanide and ZnO nanopowders. To summarise, HMM cells were seeded on 6-well plates. Following ZnO nanopowder exposure, the cells were washed 3 times with saline and then fixed with 4% glutaraldehyde in PIPES buffer (0.1 M, pH 7.4) for 1 hour at 4°C. Without removing the glutaraldehyde, the cells were scraped and transferred to a polypropylene tube to be centrifuged. The supernatant was removed, saline added, and the

mixture centrifuged again. This washing process was repeated for a total of 4 times to remove the glutaraldehyde while minimising cell loss. The cells were then incubated in suspension in 1% osmium tetroxide only at pH 7.4 for 1 hour at 4°C. They were washed 4 times in de-ionised water (DIW) before bulk staining with uranyl acetate for 1 hour at room temperature and covered with aluminium foil. Samples were washed twice in DIW followed by graded solutions of ethanol (70, 95, and 100%) and 100% acetonitrile at three times for each solution. Samples were then infiltrated under vacuum in quetol resin (Agar Scientific, UK) for 3 days and finally cured in fresh quetol resin for 24 h at 60°C. The fixed and embedded cells were sectioned with an ultramicrotome at 70 nm for BF TEM.

4.2.6.1 Mitochondria stereology

For the stereology, HMM cells seeded in 6-well plates were treated with either uncoated or PVA-coated ZnO nanopowders at 6 and 12 μg/mL for 24 hours. Control samples were prepared by culturing cells in similar conditions but without any ZnO nanopowder treatment. After sample embedding and ultramicrotome sectioning at 70 nm, forty BF TEM images were taken for every treatment. Only cells with recognisable mitochondria were imaged; this included healthy and unhealthy cells. A grid was superimposed over each image, and only grid intersections that fell within cell parts and mitochondria were counted. Each image was assessed for the normal and abnormal mitochondrial states (swollen cristae, pyknotic (electron-dense matrix with dilated electron-lucent cristae [151]), electron translucent matrices, cristae rearrangement). "Total Mitochondria" was determined by dividing the total number of intersections over mitochondria by the total number of intersections over cell parts. The "Normal Mitochondria" and "Abnormal Mitochondria" were determined by dividing the total intersections over normal or abnormal mitochondria by the total number of intersections over cell parts. Each treatment (Control, uncoated and PVA-coated ZnO nanopowders each at 6 and 12 μg/mL) was repeated a total of four times. No association was made between the mitochondrial states and different cell states (e.g. healthy, apoptotic, or necrotic). Statistical analysis of ANOVA with LSD and $P < 0.01$ was performed using Analyse-it®.

4.2.6.2 EDX

As the uranyl acetate used in bulk staining was found to replace the zinc, EDX cell samples were neither osmicated nor bulk stained. Thus, after the gluteraldehyde was removed, samples were directly treated in graded solutions of ethanol and acetonitrile before being infiltrated with quetol resin. Embedded samples were sectioned at 150–200 nm thick to increase the elemental counts available for EDX acquisition. All samples were carbon-coated to eliminate sample charging. The EDX was calibrated using an aluminium grid on copper foil.

4.2.6.3 Cryo-immobilisation by freeze-drying

HMM cells were seeded on Formvar-coated 100-meshTEM gold grids attached to 13 mm coverslips. Cells were treated with 3 μg/mL uncoated or PVA-coated ZnO nanopowder for 24 hours. The gold grids with the treated cells were removed from the coverslips, briefly rinsed twice in cold de-ionised water, and quench frozen in melting propane cooled in liquid nitrogen. They then were transferred into a brass block which was placed in an Edwards 360 vacuum coating unit and brought to room temperature over 24 hours at a vacuum of $< 1 \times 10^{-5}$ mbar. Samples were carbon-coated before EDX analysis.

4.2.6.4 Cryo-immobilisation by fixation then freeze-drying

HMM cells were seeded on Formvar-coated 100-meshTEM gold grids attached to 13 mm coverslips. Cells were treated with 3 μg/mL uncoated or PVA-coated ZnO nanopowder for 24 hours. The treatment solutions were removed and the coverslips washed 3 times with saline and refrigerated with 4% glutaraldehyde at 4°C overnight. They were then washed 3 times in DIW at 10 minutes each. The gold grids with the treated cells were removed from the coverslips, briefly rinsed twice in cold de-ionised water, and quench frozen in melting propane cooled in liquid nitrogen. They then were transferred into a brass block which was placed in an Edwards 360 vacuum coating unit and brought to room temperature over 24 hours at a vacuum of $< 1 \times 10^{-5}$ mbar. Samples were carbon-coated before EDX analysis.

4.2.6.5 Anhydrous preparation

HMM cells were seeded on 6-well plates and treated with 3 μg/mL uncoated or PVA-coated ZnO nanopowders for 24 hours and washed with saline before being fixed with 10% acrolein in polypropylene glycol for at least 1 hour. Samples were then scraped and washed with 100% ethanol at least 3 times followed by 2 washes in 100% acetonitrile. Samples were then infiltrated under vacuum in quetol resin for 3 days and finally cured in fresh quetol resin for 24 h at 60°C. The fixed and embedded cells were sectioned to 70 nm for BF TEM and 200 nm for EDX analysis. Samples for EDX analysis were carbon-coated.

4.2.7 Pulse chase

HMM cells were seeded on 6-well plates and treated with 3 μg/mL uncoated or PVA-coated ZnO nanopowders for 24 hours (*pulse*). The treatment solution was removed and the cells washed 2–3 times with PBS. Fresh culture medium was added and the cells cultured for 1 hour, 2 days, and 7 days (*chase*), renewing culture medium every 2–3 days. For the short pulse short chase, the cells were treated at 50 μg/mL for 1 hour and chased for 0, 5, 15, and 60 minutes.

After the appropriate chase time points, cells were washed and fixed with 4% glutaraldehyde according to section 4.2.6 TEM. Once the cells were scraped and cleaned of the gluteraldehyde, each sample was further divided into two separate samples: one for normal TEM imaging where cells were osmicated with 1% osmium tetroxide only and one for EDX analysis where cells were neither osmicated nor bulk stained. Embedded samples were sectioned to 70 nm for BF TEM and 200 nm for EDX analysis. EDX analysis samples were carbon-coated.

4.3 Results

4.3.1 ZnO Characterisation

Table 4.3 summarised the characterisation of both ZnO nanopowders. 100 nm-sized nanopowders were ordered; however, analysis yielded extremely variable size distributions. BF TEM images (Figures 4.1 and 4.2) showed the wide range of nanopowder size and shapes. Figure 4.3 revealed that the uncoated ZnO nanopowders had long dimensional lengths that ranged from 10 to 705 nm and short dimensional lengths from 7 to 359 nm. For the PVA-coated, the

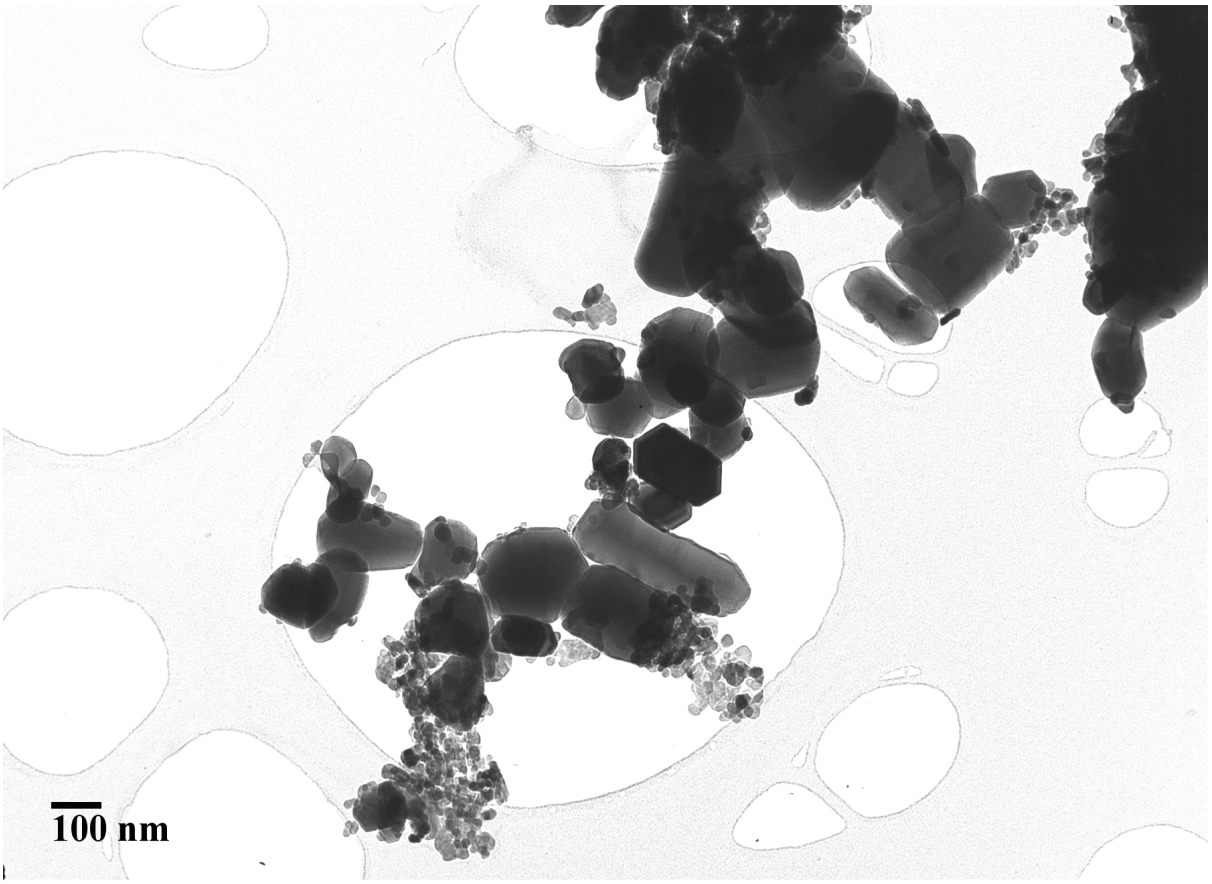

Figure 4.1: BF TEM image of uncoated ZnO nanopowders. Nanopowders ranged in all shapes and sizes with the very tiny NPs considered as ZnO nanopowders as well. Holes in the background were from the holey carbon support film on the TEM grid.

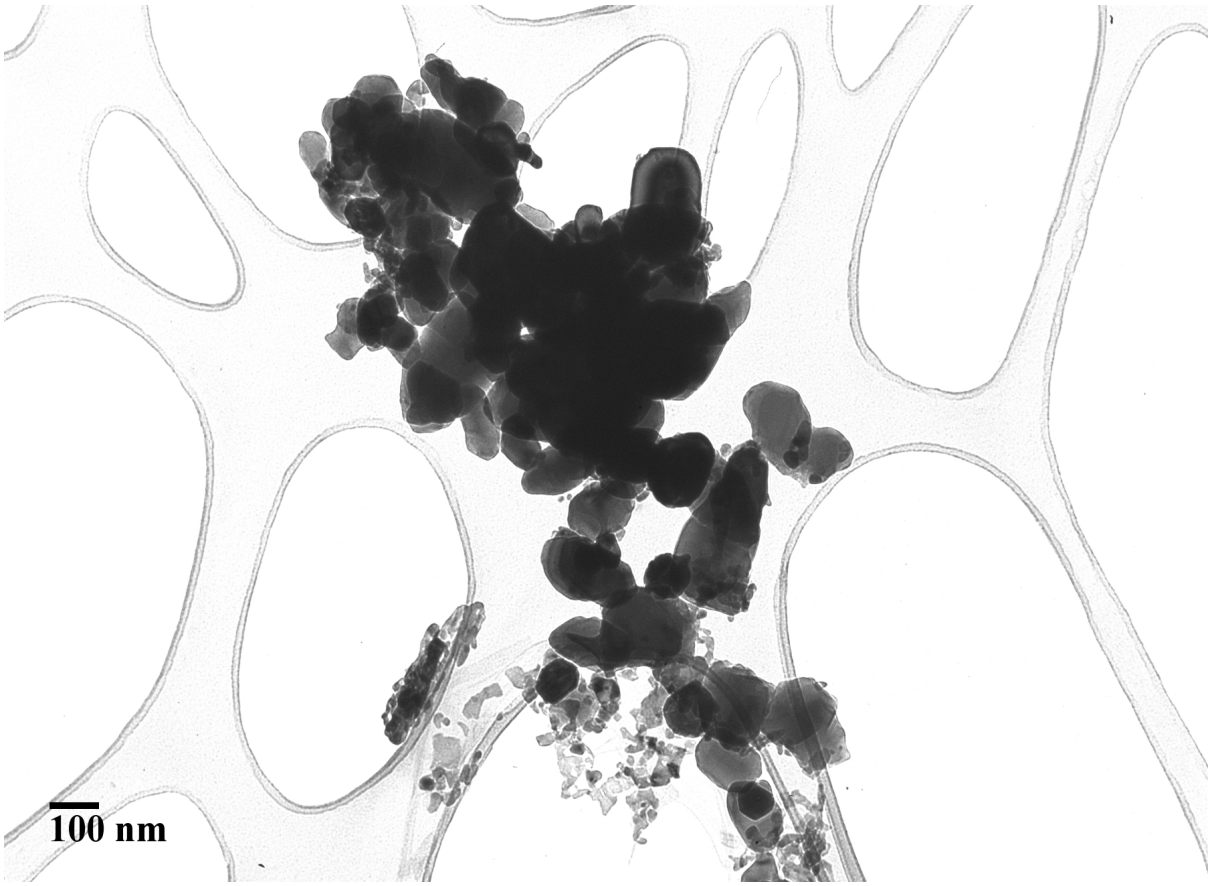

Figure 4.2: BF TEM image of PVA-coated ZnO nanopowders. Nanopowders ranged in all shapes and sizes with the very tiny NPs considered as ZnO nanopowders as well. Holes in the background were from the holey carbon support film on the TEM grid.

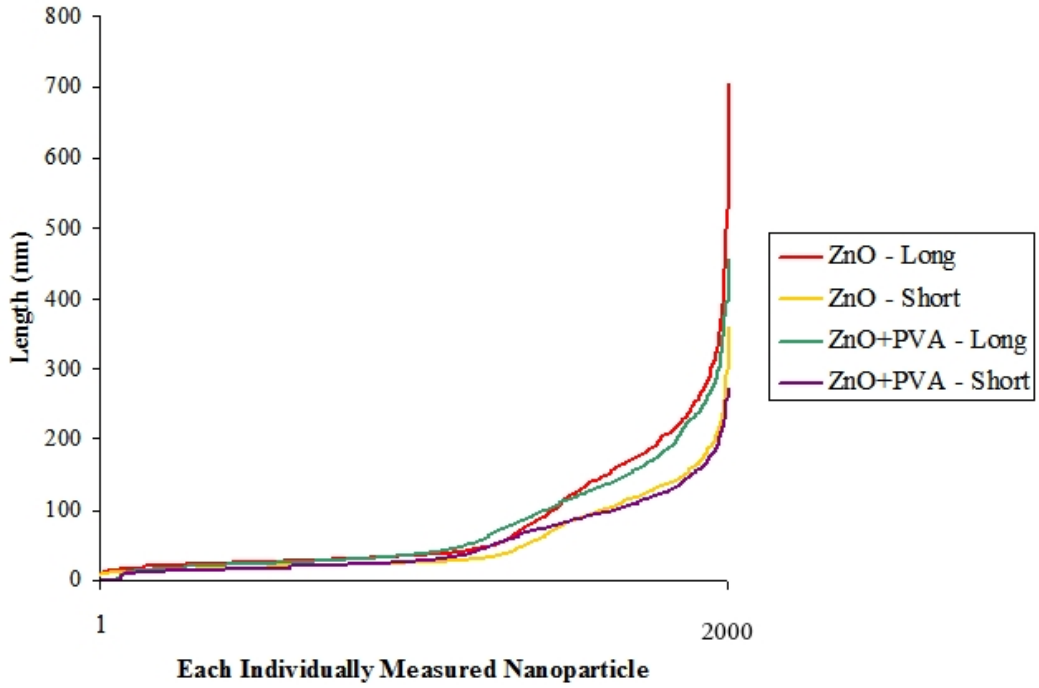

Figure 4.3: Size frequency distribution of the long and short dimensions of uncoated (ZnO) and PVA-coated (ZnO+PVA) ZnO nanopowders. 2000 NPs for each of the ZnO nanopowder samples were individually measured using ImageJ for the analysis.

	Dimension Long (nm)	Dimension Short (nm)	Aspect Ratio	Surface Area (m^2/g)	Composition
ZnO	80.3 ± 85.6	52.3 ± 52.8	1.6 ± 0.7	13.7	0.0292 wt% Ca
ZnO+PVA	76.1 ± 75.3	52.0 ± 49.6	1.5 ± 0.6	13.2	0.0307 wt% Ca
Method		TEM		BET	ICP-AES

Table 4.3: Characterisation details of the uncoated and PVA-coated ZnO nanopowders as assessed by TEM, BET method, and ICP-AES. 2000 NPs for each of the ZnO nanopowder samples were individually measured using ImageJ to determine the long and short dimensions and aspect ratio.

long dimensional lengths ranged from 0.161 to 455 nm and the short dimentional lengths from 0.109 to 271 nm. ICP-AES analysis determined that both the uncoated and PVA-coated ZnO nanopowders were fairly pure. Although numerous elements were identified in the samples, only calcium registered a substantial amount (all were < 0.01 wt%).

4.3.1.1 Aggregation

As PVA is soluble in aqueous solutions, the PVA-coated ZnO was expected to remain in solution better than the uncoated ZnO. Both samples were analysed in a Malvern Nanosizer (Malvern Instruments Ltd) in hopes of confirming this aspect. A Malvern Nanosizer measures the size of particles by analysing the rate that laser light scattered from the particles diffuses across the aqueous solution. Contrary to expectations, the results suggested that both were aggregating. The initial analysis of the uncoated ZnO yielded an average aggregate size of 400 nm. If the nanopowders formed a true solution, they would remain dissolved even after centrifugation. Consequently, the solution was centrifuged to remove aggregates, and particles from the supernatant were measured. Subsequent analysis yielded an average diameter range of 26.5–115 nm. For the PVA-coated ZnO, an initial reading yielded an average diameter range of 30.4–181 nm. After centrifugation, no readings could be generated. This suggested that the PVA-coated ZnO may have completely aggregated and none were left in solution. Unfortunately, analysis from a Malvern Nanosizer was limited as it did not directly measure the aggregate sizes; moreover, the average could be skewed by the presence of extremely large or small aggregates [152]. Additionally, if either the uncoated or coated ZnO nanopowders dissolved into ions, it would not be detected as the Malvern Nanosizer required at least 2 nm in size.

With the inconclusive results from the Malvern Nanosizer, both nanopowders were further analysed in the SEM to determine aggregation (Figure 4.4 and Table 4.4). Both nanopowders formed aggregates. Although the PVA-coated ZnO nanopowders seemed to yield slightly smaller aggregates, the differences were fairly minor.

4.3.1.2 Raman spectroscopy

Raman spectroscopy was measured to assess the crystalline structure of the ZnO nanopowders. Figure 4.5 contained the spectra for both the uncoated and PVA-coated ZnO nanopowder. Both

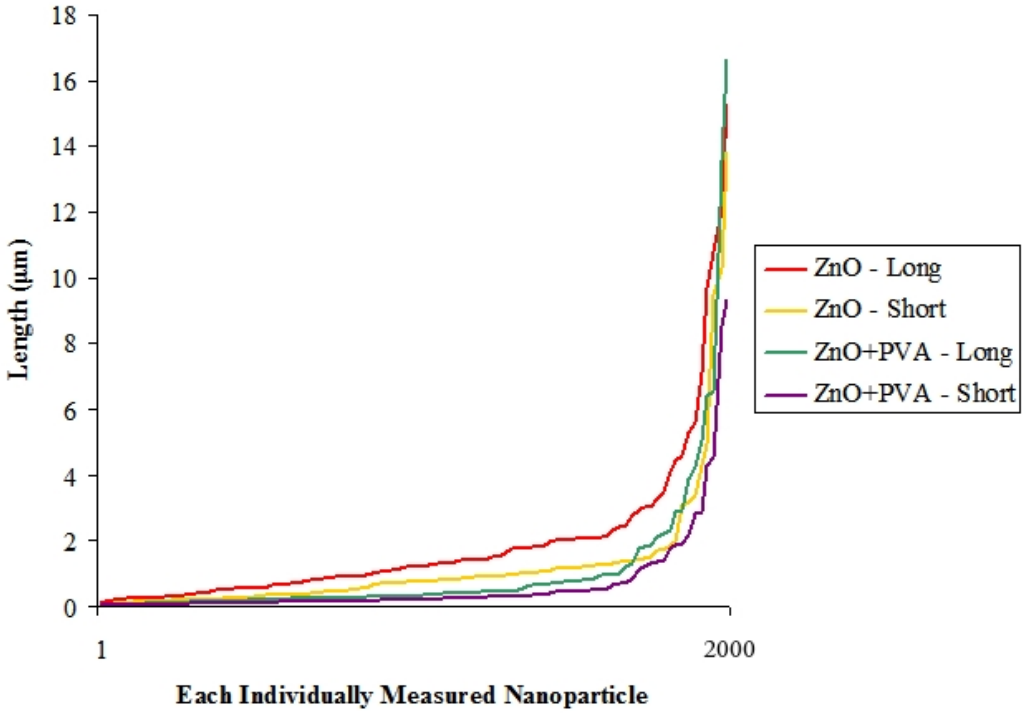

Figure 4.4: Size frequency distribution of the long and short dimensions of uncoated (ZnO) and PVA-coated (ZnO+PVA) ZnO nanopowder aggregates. 100 aggregates for each of the ZnO nanopowder samples were individually measured using ImageJ for the analysis. Most aggregate lengths were < 2 μm with the exception of a few outliers that were > 9 μm for both nanopowder aggregates.

	Dimension Long (μm)	Mean(μm)	Dimension Short (μm)	Mean (μm)	Aspect Ratio	Mean
ZnO	0.134 – 15.2	1.9 ± 2.6	0.059 – 10.8	1.1 ± 1.8	1.04 – 7.22	1.9 ± 0.8
ZnO+PVA	0.050 – 16.6	1.0 ± 2.3	0.031 – 9.34	0.6 ± 1.4	1.00 – 3.89	1.7 ± 0.6

Table 4.4: Characterisation of uncoated and PVA-coated ZnO aggregates via SEM. 100 aggregates for each of the ZnO nanopowder samples were individually measured via ImageJ. The PVA-coated ZnO nanopowders resulted in slightly smaller aggregates.

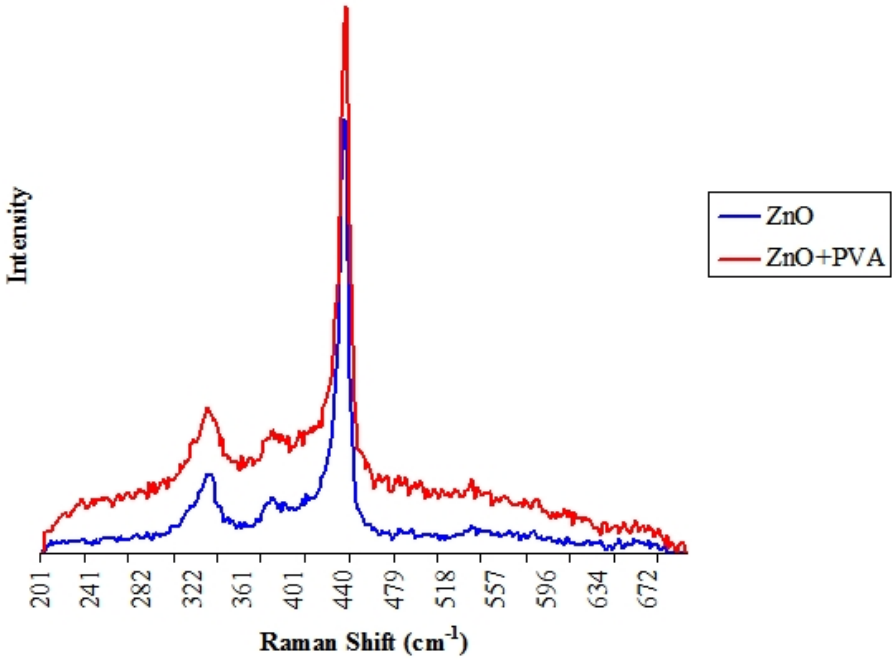

Figure 4.5: Raman spectra of uncoated (ZnO) and PVA-coated (ZnO+PVA) ZnO nanopowders using the excitation wavelength 633 nm. Both spectra were nearly identical. The high intensity peak at 439 cm^{-1} indicated good crystalline structures. No apparent peak near 580 cm^{-1} suggested no obvious defects.

spectra were nearly identical. A larger sample quantity or higher background noise might have caused the higher intensity spectra for the PVA-coated. The high intensity peaks near 439 cm^{-1} for both spectra indicated good crystallinity while no apparent peaks near 580 cm^{-1} signified a lack of defects in the crystalline structure, such as oxygen vacancies or zinc interstitials caused by missing oxygen atoms. These defects could yield unpaired zinc ions which might generate ROS [153, 154].

4.3.1.3 Photoluminescence

As ZnO was found to excite at the UV and violet light range (360–385 nm), photoluminescence was performed to confirm the excitation wavelength for the uncoated and PVA-coated ZnO nanopowders. Figure 4.6 confirmed that the peak excitation wavelength for both ZnO nanopowders was 379 nm. The PVA-coated ZnO nanopowder yielded a lower intensity spectrum, suggesting that the PVA-coating might affect the emission intensity of ZnO nanopow-

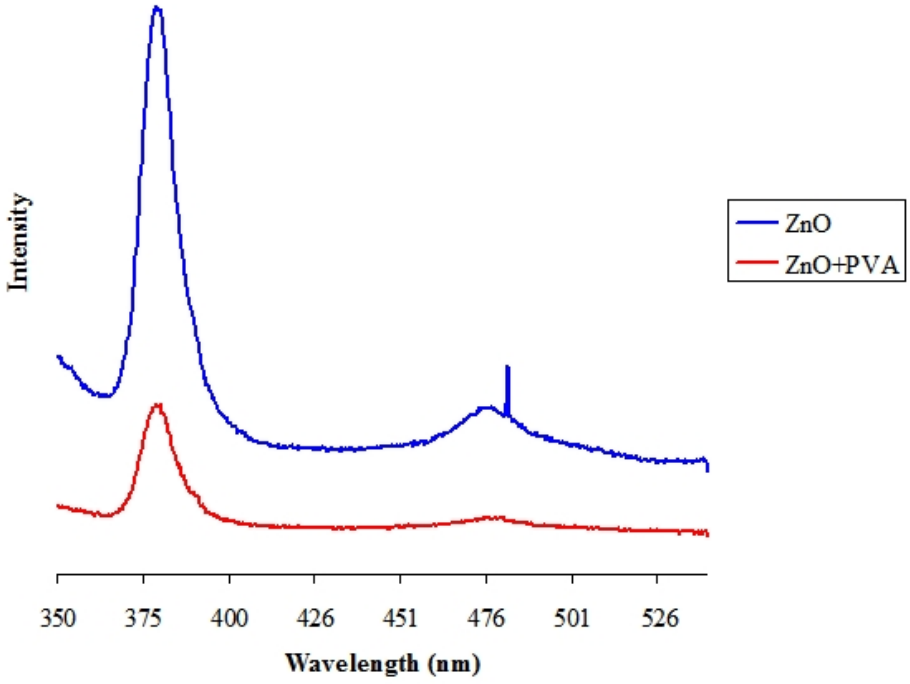

Figure 4.6: Photoluminescence spectra of uncoated (ZnO) and PVA-coated (ZnO+PVA) ZnO nanopowders using the excitation wavelength 320 nm. Main emission peak was at 379 nm for both nanopowders. The small emission peak at 476 nm resulted from defects in the nanopowders. The emission intensity was lower for the PVA-coated ZnO nanopowder.

ders. Contrary to the Raman spectra, the small peaks at 476 nm suggested possible defects. As Raman spectroscopy only assessed the crystalline structure, the defects noted in photoluminescence included those that would affect the generated luminescence by the ZnO nanopowders. These defects could include oxygen vacancies, zinc interstitials, surface defects, or surface impurities (e.g. hydrogen, hydroxyl, carboxylate, alkane) [155]. The exact defect(s) and their effects on cells would require further analysis.

4.3.2 Assessment of cell viability assay interactions

As no current literature exists assessing whether ZnO NPs interact with viability assays, control experiments for the NR and LDH were performed similarly to the MWNTs and SWNTs to investigate this possibility. A different set of concentrations were used: only two coincided with the actual cell viability assays with one additional high concentration. This was to provide a broader spectrum in case interactions only occurred at higher concentrations. The NR revealed

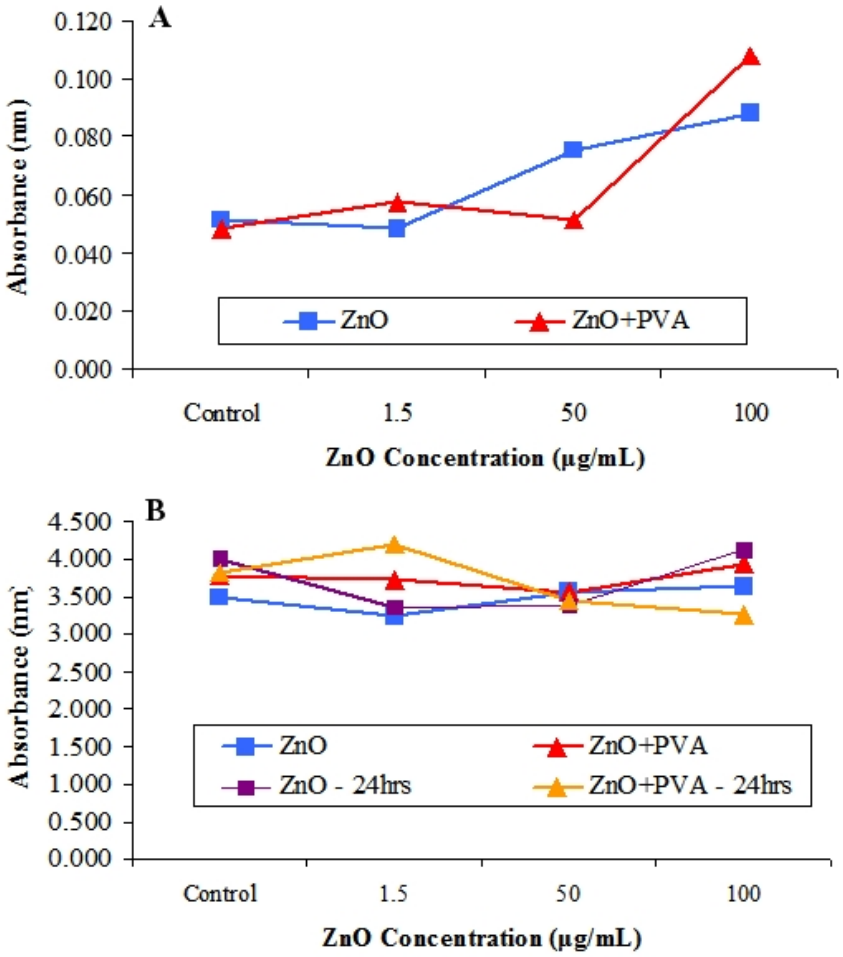

Figure 4.7: Effects of uncoated (ZnO) and PVA-coated (ZnO+PVA) ZnO nanopowders on colorimetric dyes: A) NR and B) LDH without and with 24 hour incubation of LDH enzyme with ZnO nanopowders. Potential binding effects were observed in the NR assay while minimal effects were seen with the LDH.

some interactions at the higher concentrations, although interactions remained minimal at 50 μg/mL, the highest concentration used in the viability assays in this study (Figure 4.7). Little to no interactions were observed in the LDH. Consequently, the NR and LDH assay, in addition to the live dead assay, were used in this study.

4.3.3 ZnO nanopowder toxicity

HMMs were treated with both nanopowders at concentrations ranging from 1.563 to 50 μg/mL for only 24 hours as significant death was already present. The ZnO nanopowders exhibited a concentration dependent toxicity with a sudden increase in cell death between 12.5 and 25 μg/mL; all three assays reflected this threshold (Figure 4.8). Significant toxicity was observed for the uncoated ZnO in all three assays at 12.5 μg/mL and above, while only the live dead assay yielded similar results for the PVA-coated. Significant toxicity for the PVA-coated was only observed at 25 μg/mL and above for the NR and LDH. No clear distinction in toxicity could be differentiated between the uncoated and PVA-coated ZnO nanopowders, although the slight difference in significant toxicity suggested that the uncoated was slightly more toxic.

Several papers similarly observed the sudden increase in cell death (Table 4.5). Lin et al. [142] found that both 70 and 420 nm ZnO NPs yielded accelerated cell death between 10–18 μg/mL (length of exposure used not indicated). Deng et al. [156] concluded similarly when comparing 10, 30, 60, and 200 nm ZnO NPs in mouse neural stem cells for 24 hours and observed the acceleration after 12 μg/mL. On the contrary, Jeng et al. [141] found that mouse neuroblastoma cells exhibited a gradual increase in cell death when 50–70 nm ZnO NPs were treated at 10–200 μg/mL for 24 hours. One explanation may be the homeostatic mechanisms in neurons as proposed by Vallee et al. [123]. As zinc was involved in neurological processes, a large concentration existed in the brain; up to 300 μM zinc could be found in the synaptic vesicles of neurons. Although toxic effects were observed in neuronal cells *in vitro*, the existence of such high concentrations of zinc in the brain suggested that a different metabolic strategy may exist. Another factor may be the length of treatment. Both Sharma et al. [145] and Lin et al. [142] revealed that increasing the ZnO NP treatment time increased the rate of cell death after the threshold point. When Sharma et al. exposed A431 cells to ZnO for 3, 6, 24, or 48 hours, no sudden acceleration in cell death was observed until 24 and 48 hour exposure

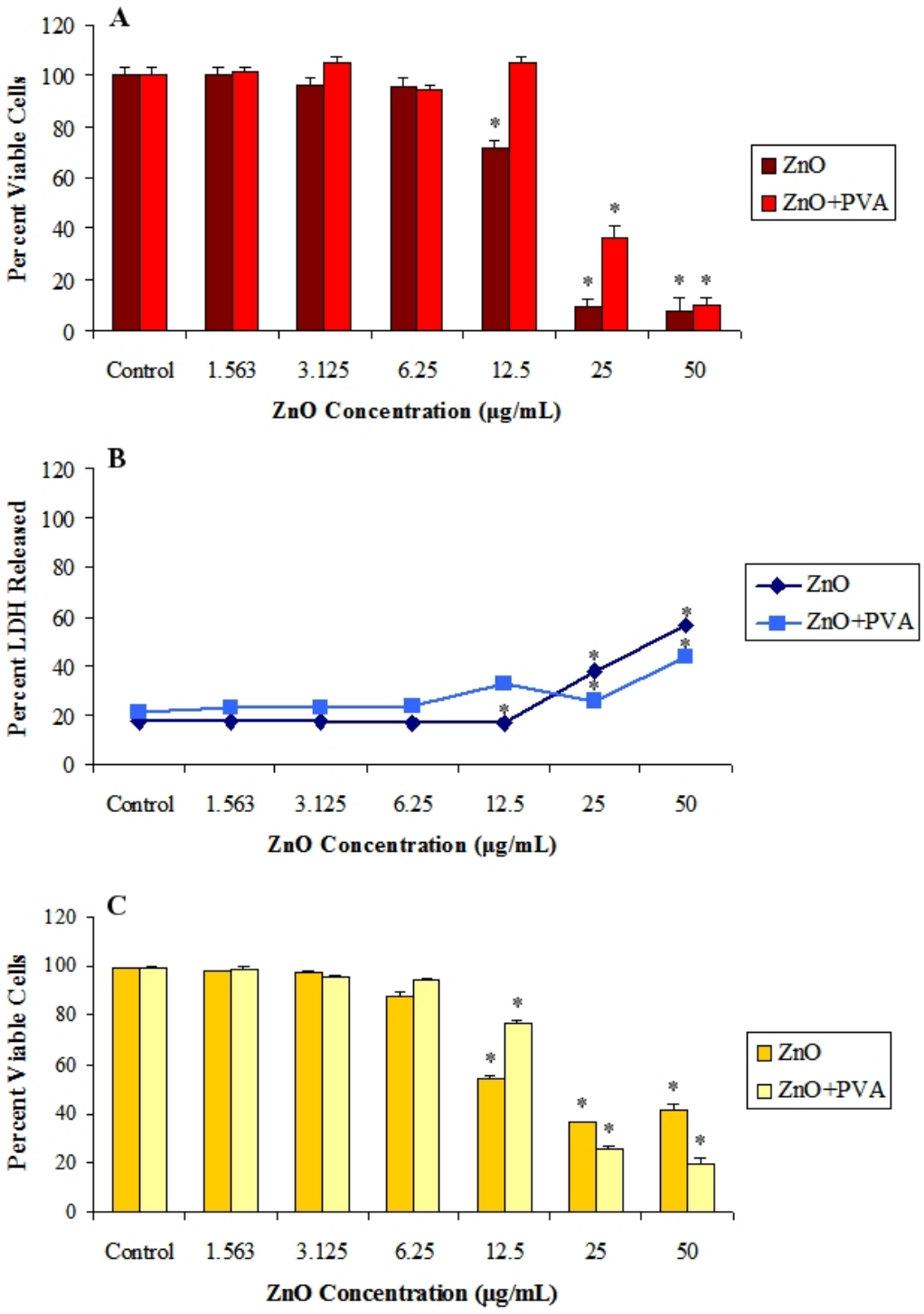

Figure 4.8: Toxicity of uncoated (ZnO) and PVA-coated (ZnO+PVA) ZnO nanopowders after 24 hours based on 3 assays: (A) NR, (B) LDH, and (C) live dead. NR and LDH values represented the mean ± SE of three experiments each performed in triplicates; live dead values were the mean ± SE of five individual experiments (ANOVA with LSD, $P < 0.01$, Analyse-it®). Cells treated under similar conditions but without either ZnO nanopowders were used as controls. Statistical significance (*) was assessed between the concentrations and their respective controls.

(at 0.8 μg/mL). For Lin et al., exposing ZnO to A549 for 6, 12, and 24 hours yielded gentle-sloped rate of toxicity for the 6 hour exposure (highest death of ~20%), medium-sloped rate of toxicity for the 12 hours (highest death of ~40%), and steep-sloped rate of toxicity for the 24 hours (highest death of ~80%). All these studies indicated that ZnO toxicity could be affected by factors such as size, cell line, and length of exposure and should be taken into consideration when determining their cytotoxic potential.

	Particle size (nm)	Cell Type	Conc. μg/mL	Time (hrs)	Assay	Threshold point
Xia et al [159]	13	RAW 264.7 murine macrophage	25	1–16	MTS	4 hrs
Sharma et al [160]	30	A431 human epithelial	0.008–20	3–48	NR, MTT, LDH	0.8 μg/mL, most apparent after 24 hrs
Lin et al [158]	70, 420	A549 human alveolar	8–18	6–24	LDH	8 μg/mL, rate of death increases with longer treatment
This study	80x52	HMMs human macrophage	1.5–50	24	NR, LDH, live dead	12.5 μg/mL

Table 4.5: Comparison of studies that observed sudden acceleration of ZnO-induced cell death

4.3.4 ZnO dissolution

Zinc is known to exist in aqueous solutions as Zn^{2+} cations, and acidic conditions can further promote ZnO dissolution [122]. Xia et al. found that ZnO dissolved more readily in culture medium (Dulbecco's modified eagle medium) than water, although the dissolution was less complete than $ZnSO_4$, which readily dissolved into Zn^{2+} cations [144]. Franklin et al. [146] compared $ZnCl_2$ toxicity in freshwater alga to ZnO and found the concentration-response curve for Zn^{2+} for both $ZnCl_2$ and ZnO corresponded suggesting that ZnO toxicity resulted from the Zn^{2+} cations. Both Xia et al. [144] and Heinlaan et al. [147] compared $ZnSO_4$ to ZnO and found that $ZnSO_4$ caused greater toxicity than ZnO. The difference in result may be caused by the different reference Zn^{2+} cation source chemicals; however, all concluded that ZnO disso-

lution contributed to the observed toxicity. Consequently, a similar assessment was performed comparing the toxicity of $ZnCl_2$ with the uncoated and PVA-coated ZnO nanopowders (Figure 4.9). As $ZnCl_2$ readily dissociates into Zn^{2+} + 2 Cl^-, any toxicity caused by $ZnCl_2$ could be attributed to Zn^{2+} cations. The uncoated ZnO nanopowder yielded a curve similar to $ZnCl_2$ with no significant differences implicating the role ZnO dissolution may have in the resulting cell death. The PVA-coated ZnO nanopowder resulted in a slightly less toxic curve with significant differences at the 10 and 20 μg/mL to both the $ZnCl_2$ and uncoated ZnO. This suggested that the PVA-coating might have decreased the effects of Zn^{2+}.

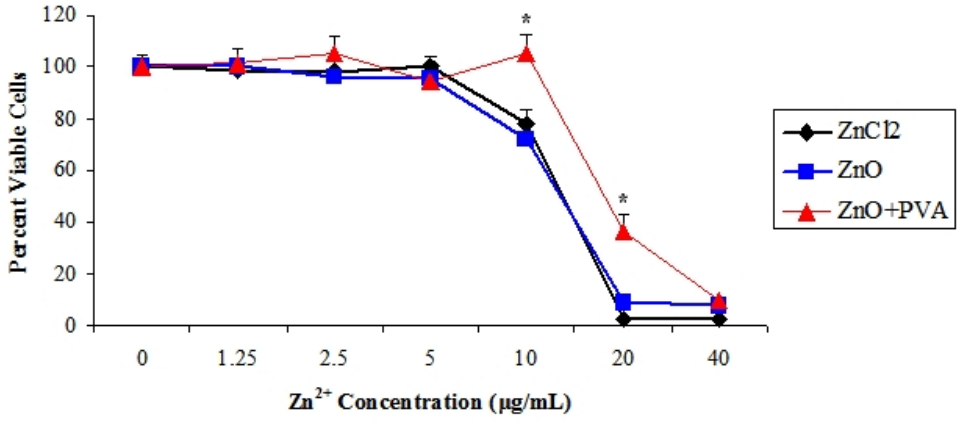

Figure 4.9: Toxicity of $ZnCl_2$ and uncoated (ZnO) and PVA-coated (ZnO+PVA) ZnO nanopowders using NR to determine the possible effects of ZnO dissolution. NR values represented the mean ± SE of three experiments each performed in triplicates for each of the three samples (ANOVA with LSD, $P < 0.01$, Analyse-it®). $ZnCl_2$ experiments were performed by K. H. Müller. Cells treated under similar conditions but without chemicals were used as controls. Statistical significance was assessed between the three chemicals; the * indicated significant difference between the PVA-coated ZnO (ZnO+PVA) and both $ZnCl_2$ and uncoated ZnO.

As the pH varied within the cell (Table 4.2), ZnO dissolution was further analysed using ICP-OES (or ICP-AES) to determine if the concentration of dissolved zinc varied amongst the various cell compartments. Results revealed that ZnO dissolved the greatest in lysosomal buffer, the buffer with the lowest pH (5.0) amongst all 4 buffers (Figure 4.10). This confirmed that acidic conditions promote ZnO dissolution, which may affect the amount of Zn^{2+} cations exposed to cells depending on where the ZnO nanopowders access the cells. As the ICP-OES only assessed the presence of zinc particles, direct analysis of the type of zinc ion(s) dissociated

is required to determine if only Zn^{2+} cations are present or if other ion species exist as well (e.g. $Zn(OH)^{+}$, $Zn(OH)_2$, $Zn(OH)_3^{-}$ and $Zn(OH)_4^{2-}$).

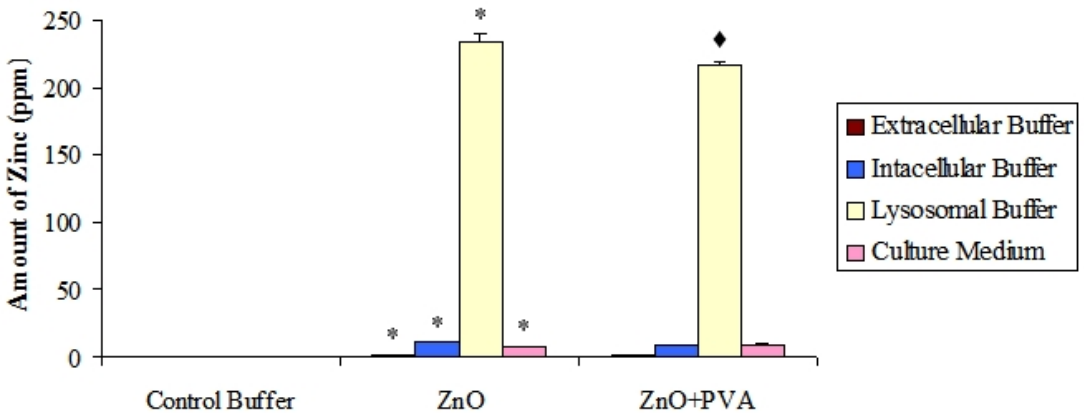

Figure 4.10: Uncoated and PVA-coated ZnO nanopowder dissolution in different cell buffers according to ICP-OES. All readings were performed three times, each in duplicates, for a total of six readings per sample. Data presented as mean ± SE of the six readings (ANOVA with LSD, $P < 0.01$, Analyse-it®). Symbols (*, ♦) indicated statistical significance between buffers within each nanopowder. For the uncoated ZnO (ZnO), zinc presence in all four buffers were statistically significantly different. For the PVA-coated ZnO (ZnO+PVA), only the lysosomal buffer was statistically different from all the other buffers. Additionally, for the intracellular buffer, lysosomal buffer, and culture medium, dissolution was statistically significantly different between the control, ZnO, and ZnO+PVA (not shown on graph to reduce confusion). Control buffers were respective buffer solutions without either ZnO nanopowders added. Experiments were performed by M. Motskin.

4.3.5 Microscopy

The ZnO nanopowders were first imaged in the confocal microscope to determine visibility (refer to chapter 2.3.5 MWNT: Active/Passive Uptake for protocol). None of the lasers used caused the ZnO to fluoresce; as a result, they were imaged using the 488 nm laser in reflectance mode. Figure 4.11 showed indications of a HMM phagocytosing a cluster of ZnO nanopowders. As only large clusters could be seen in the confocal microscope coupled by the possibility of ZnO dissolution, all imaging was directed to the TEM.

Preliminary morphological analysis on the TEM of HMMs treated with 6, 12, and 25 μg/mL

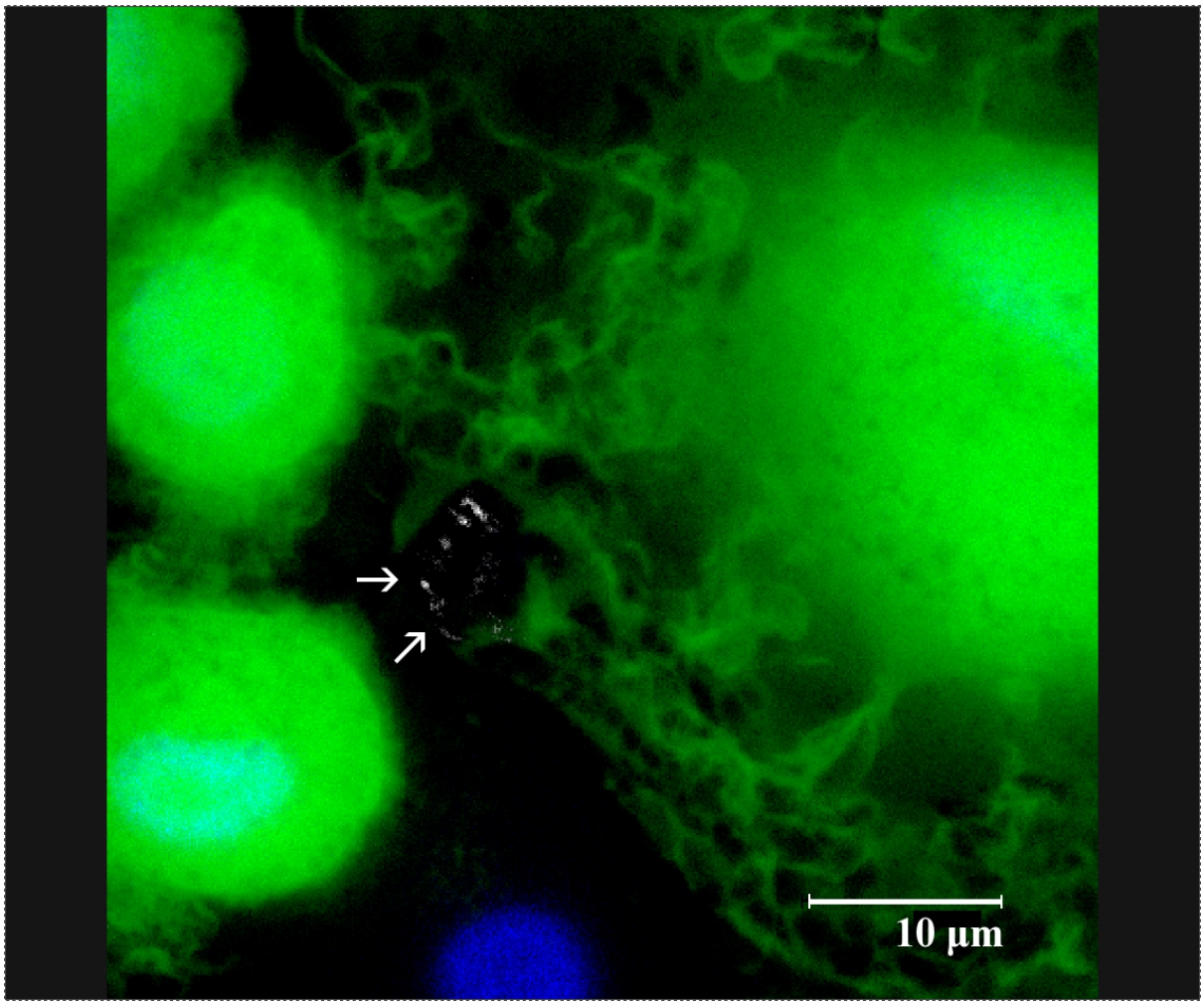

Figure 4.11: Confocal microscope average projection of an image stack of a HMM phagocytosing ZnO nanopowders (green = cytoplasm, blue = nucleus, white = ZnO). White arrows indicated the ZnO nanopowders and site of phagocytosis.

uncoated and PVA-coated ZnO nanopowders for 24 hours suggested that treated cells died mainly via apoptosis and exhibited pronounced microfilaments (Figures 4.12 and 4.13) and pyknotic mitochondria (Figure 4.14) more frequently than control cells.

Mitochondrial damage has been associated with Zn^{2+} neurotoxicity, including disruption of the mitochondrial electron transport chain, loss of mitochondrial membrane potential, reduced ATP production, and increase in mitochondrial ROS production [157]. Sensi et al. [158] found that Zn^{2+} could enter mitochondria through the Ca^{2+}-permeable α-amino3-hydroxy-5-methyl-4-isoxazolepropionic-acid/kainate channels and cause ROS generation and subsequent mitochondrial damage. Marin et al. [159] concluded that Zn^{2+} inhibited mitochondrial respiration which led to depleted ATP production. Because of this relationship, a stereological analysis of the abnormal mitochondrial states (pyknotic, swollen cristae, or electron translucent) was carried out (Figure 4.15). Table 4.6 summarised the results. The total mitochondria

		ZnO		ZnO+PVA	
	Control	6 μg/mL	12 μg/mL	6 μg/mL	12 μg/mL
Total Mitochondria	3.95 %	3.69 %	3.16 %	3.94 %	3.59 %
Normal Mitochondria	3.55 %	3.10 %	2.36 %	2.87 %	2.94 %
Abnormal Mitochondria	0.40 %	0.60 %	0.79 %	1.07 %	0.65 %

Table 4.6: ZnO mitochondria stereology results. No statistical significance between any of the treatment conditions were found (ANOVA with LSD, $p > 0.01$, Analyse-it®).

present were similar between the control and treated conditions. The number of abnormal mitochondria in the 6 μg/mL uncoated ZnO increased by 50% and 12 μg/mL by 100%; the PVA-coated ZnO yielded a slightly different result with 6 μg/mL increasing by 168% and 12 μg/mL by 63%. Although the actual percentages were relatively small, the increase observed in both the uncoated and PVA-coated ZnO treated cells indicated that ZnO may indeed affect the mitochondrial condition.

Foreign NPs indicative of uncoated and PVA-coated ZnO nanopowders could be seen in the TEM images; however, it was uncertain if they were actual ZnO nanopowders or debris. EDX was used in an attempt to identify ZnO nanopowder presence in the cells. Although many cells were found with ZnO-like nanopowders, very few registered positively as zinc on the EDX (Figure 4.16). With evidence that ZnO nanopowders can dissolve into Zn^{2+} cations, we

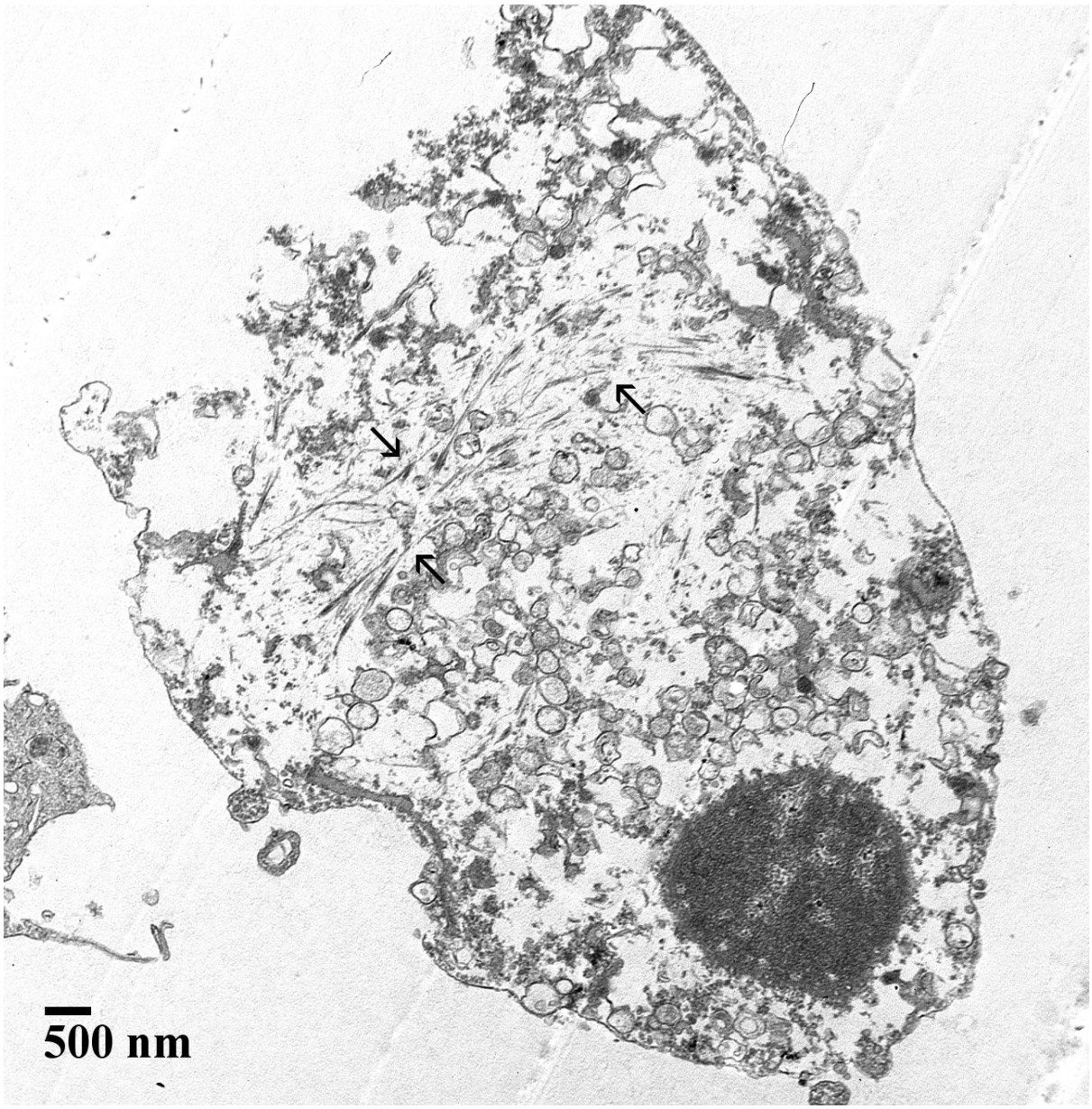

Figure 4.12: BF TEM image of a cell treated with uncoated ZnO nanopowder (12 μg/mL ZnO for 24 hours). Morphology indicative of secondary necrosis, although the condensed nucleus appeared atypical and no apoptotic bodies were present. Pronounced microfilaments could be seen in the cytoplasm (black arrows).

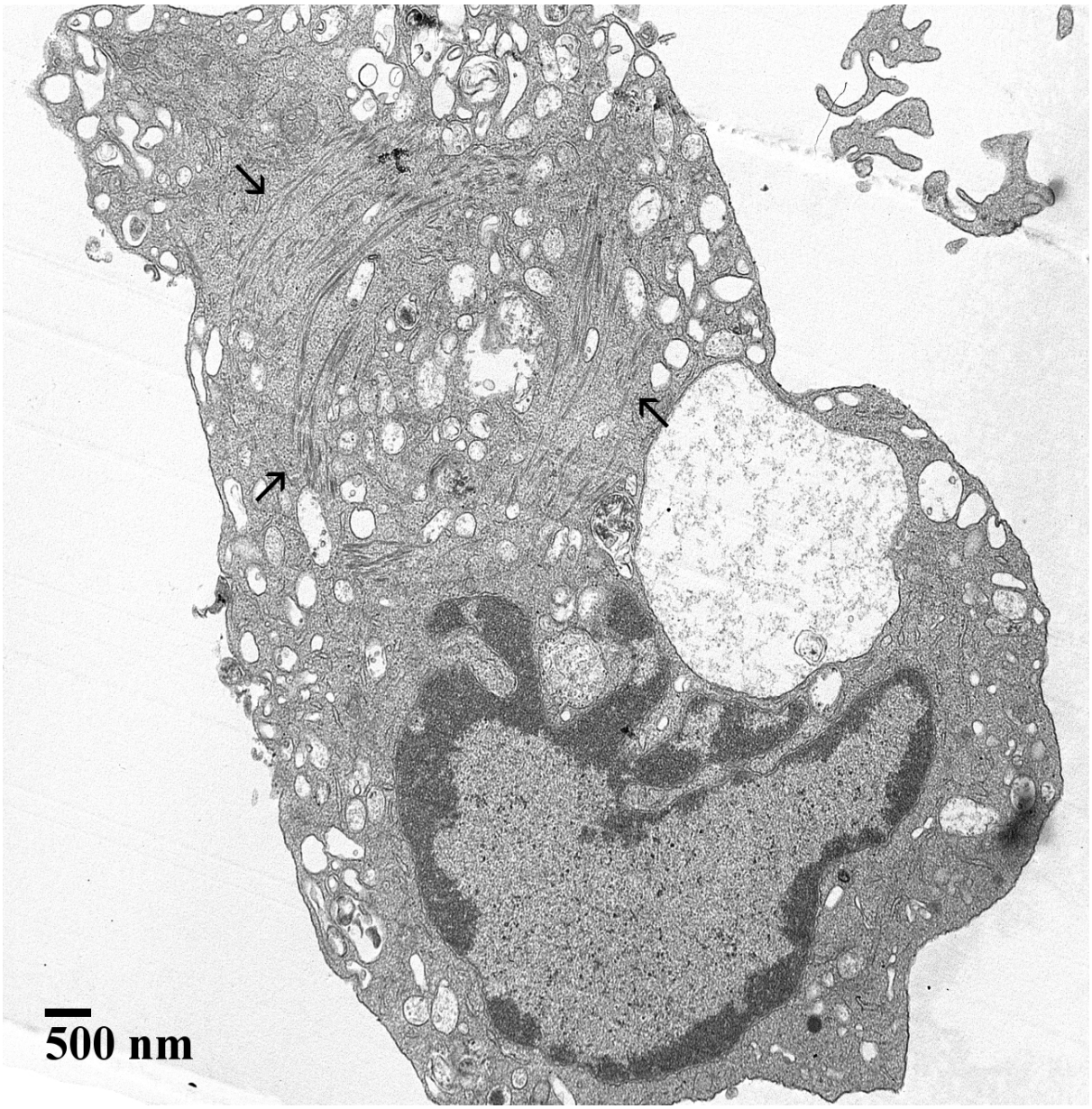

Figure 4.13: BF TEM image of a cell treated with uncoated ZnO nanopowder (25 μg/mL ZnO for 24 hours). Cell appeared unhealthy as no pseudopodia (projections along the plasma membrane) were present. Pronounced microfilaments were observed in the cytoplasm (black arrows). A large vacuole was also present containing, most likely, only debris.

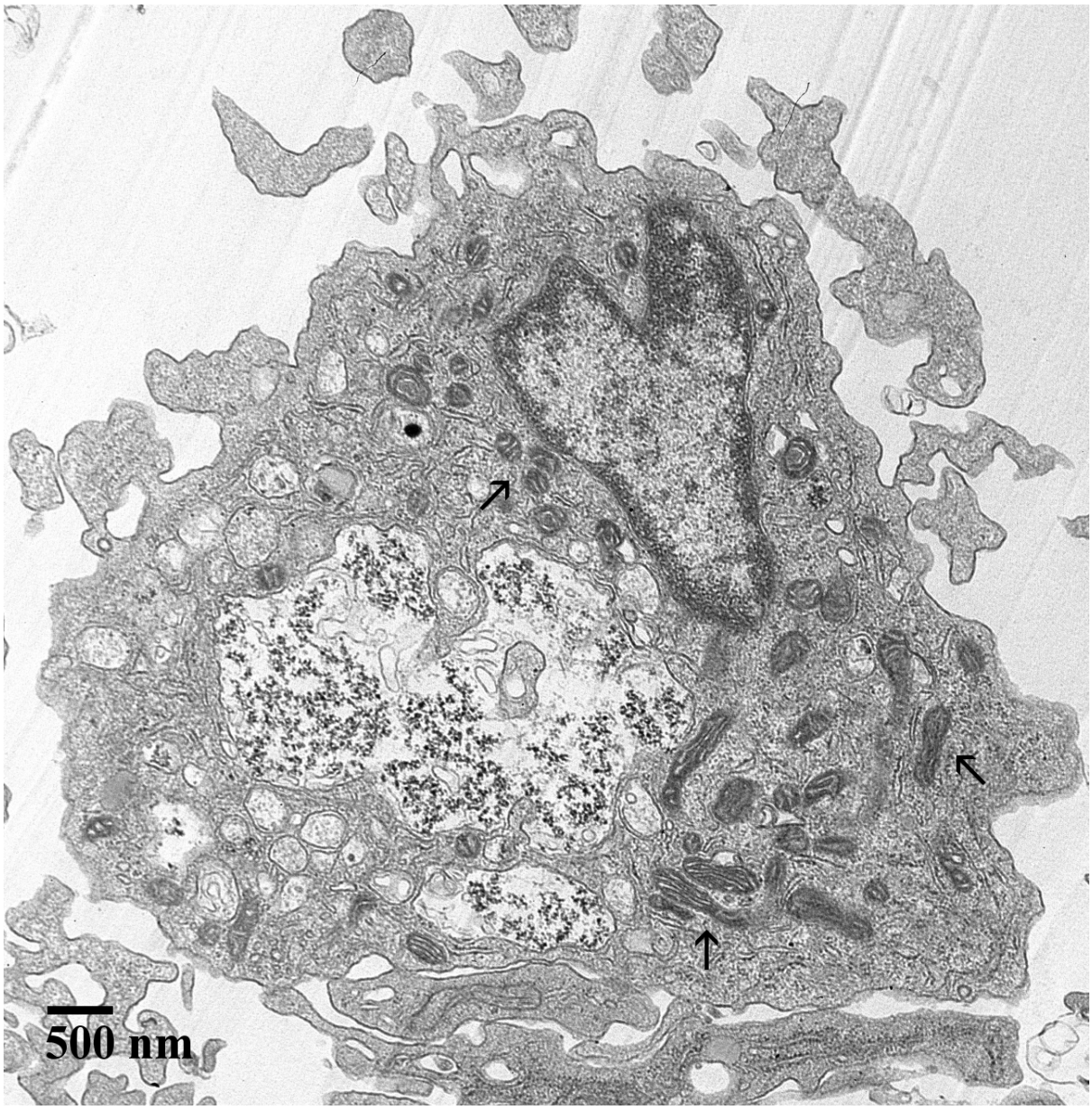

Figure 4.14: BF TEM image of a cell treated with uncoated ZnO nanopowder (6 μg/mL ZnO for 24 hours). Cell appeared unhealthy as pseudopodia had disappeared and blebbing (budding of cell parts along plasma membrane) was present. Mitochondria exhibited pyknosis (black arrows). A large vacuole was present, but it could not be confirmed whether the dark NPs were ZnO nanopowders or debris.

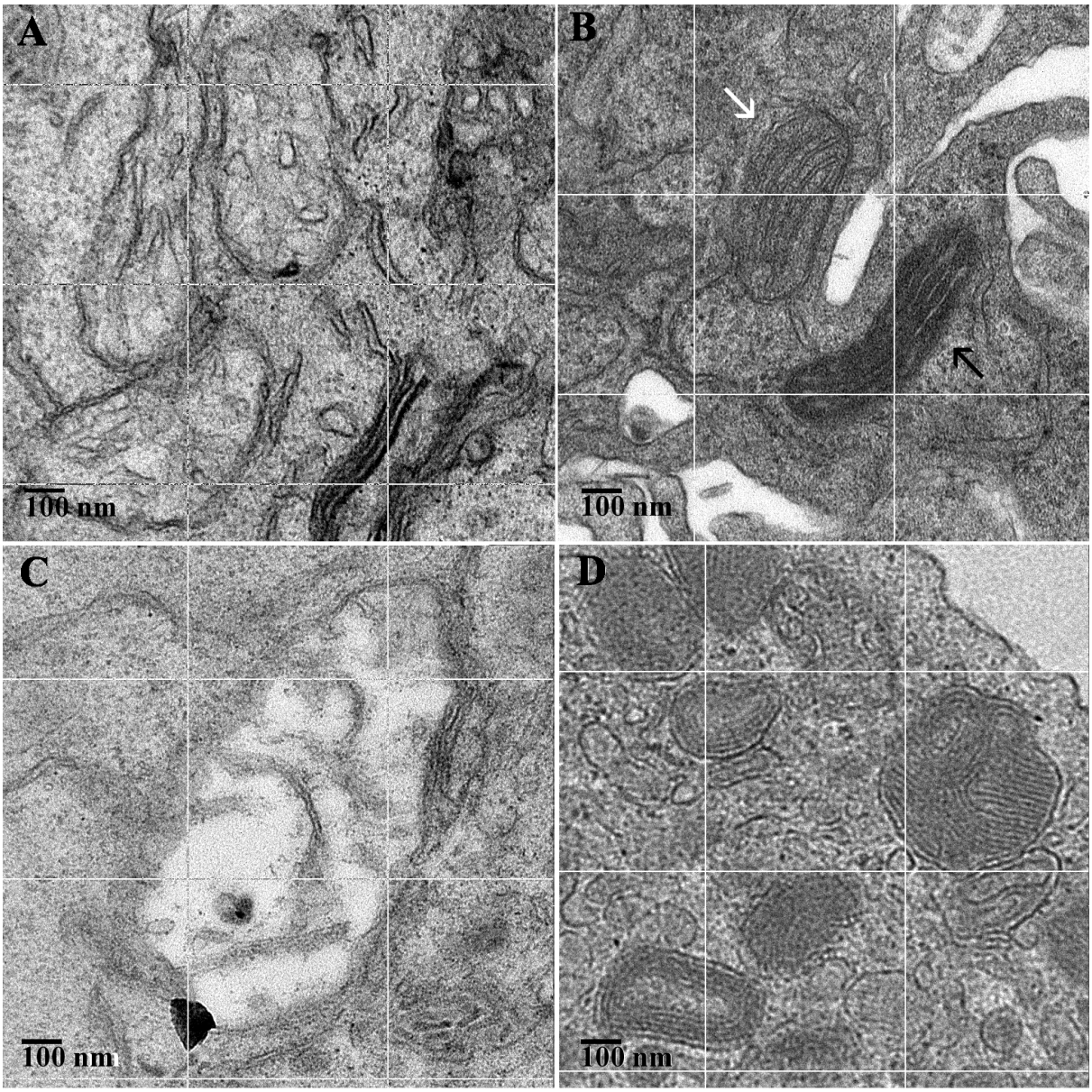

Figure 4.15: BF TEM images of abnormal mitochondria: A) Mitochondria with swollen cristae, B) Pyknotic (electron dense matrix with lucent cristae) (black arrow), C) Electron translucent matrices, and D) Cristae rearrangement. White lines were the grid lines superimposed for mitochondria stereology. A normal mitochondria could be seen in inset B indicated by a white arrow.

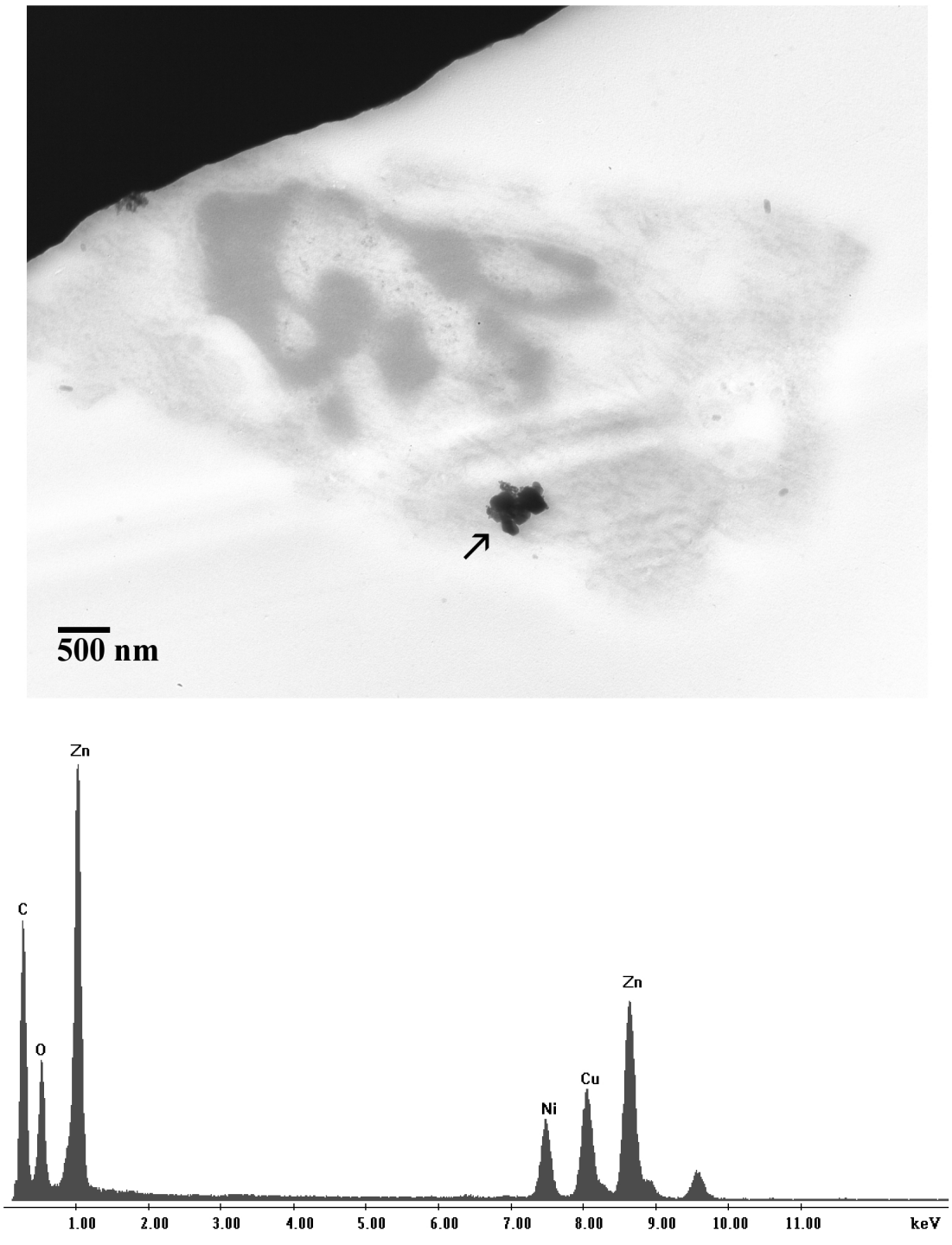

Figure 4.16: BF TEM image of uncoated ZnO nanopowder in a HMM with EDX confirming presence of ZnO. The black arrow indicated the identified ZnO nanopowder selected for the EDX analysis.

hypothesised that the uncoated and PVA-coated ZnO nanopowders may have dissolved during treatment or sample preparation resulting in the lack of detection in the TEM and EDX. Various methods were undertaken to address this possibility: cryo-immobilisation followed by freeze-drying, cryo-immobilisation by fixation then freeze-drying, and anhydrous preparation.

Cryo-immobilisation by freeze-drying and cryo-immobilisation by fixation then freeze-drying could help identify whether ZnO dissolved into zinc ions. When cells are freeze-dried, both ZnO nanopowders and zinc ions are retained while fixed cells become permeable and release the zinc ions; this affirms whether any ZnO nanopowders remain or all are dissolved into zinc ions. As the freeze-dried cells should retain the most zinc, the freeze-dried gold grids were quantitatively analysed first with the EDX; unfortunately, no zinc registered.

Since all previous sample preparations involved aqueous solutions, an anhydrous protocol which eliminated the use of water was employed to prevent any remaining uncoated or PVA-coated ZnO nanopowders from dissolving. Black NPs indicative of ZnO NPs were seen in the treated cells and not in the control cells; however, when analysed in the EDX, no zinc registered. We concluded that the amount of ZnO present may be too low for the detector to detect.

4.3.6 Pulse chase

As the toxicity assays revealed that both uncoated and PVA-coated ZnO nanopowders were acutely toxic, pulse chase experiments were performed to assess long term toxicity. Cells were pulsed at a less toxic concentration of 3 μg/mL for 24 hours to ensure that cells could survive the longer chase time points. Cells were initially chased for 1 hour (Figure 4.17), 2 days (Figure 4.18), and 7 days (Figure 4.19). BF TEM yielded similar images as the preliminary morphological analysis (i.e. pronounced microfilaments and mitochondrial pyknosis). Black NPs suggestive of ZnO nanopowders were observed; however, EDX analysis could not confirm the presence of ZnO in the cells. A short pulse at high concentration followed by short chases was attempted to try and reduce ZnO nanopowder dissolution. HMMs were pulsed at 50 μg/mL for 1 hour and chased at 0, 5, 15, and 60 minutes. BF TEM revealed few dead cells suggesting that the uncoated and PVA-coated ZnO nanopowders were not exceedingly acutely toxic. No EDX was performed as the ZnO present was too low for the detector to detect.

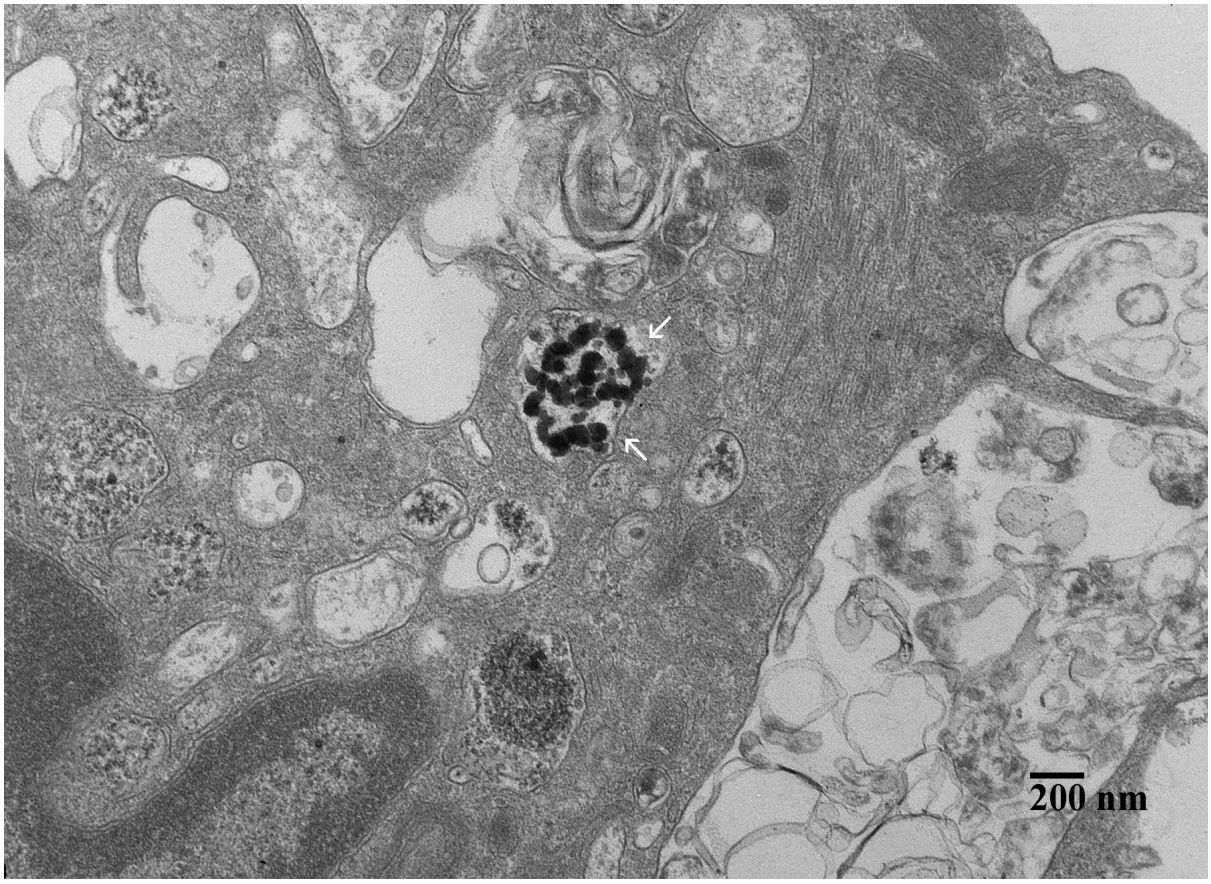

Figure 4.17: BF TEM image of a cell with unconfirmed NPs after a 3 μg/mL pulse with uncoated ZnO nanopowders for 24 hours and a 1 hour chase. White arrows indicated NPs suggestive of uncoated ZnO nanopowders, but EDX analysis could not confirm. The cell was in a healthy state (determined from a separate less magnified image).

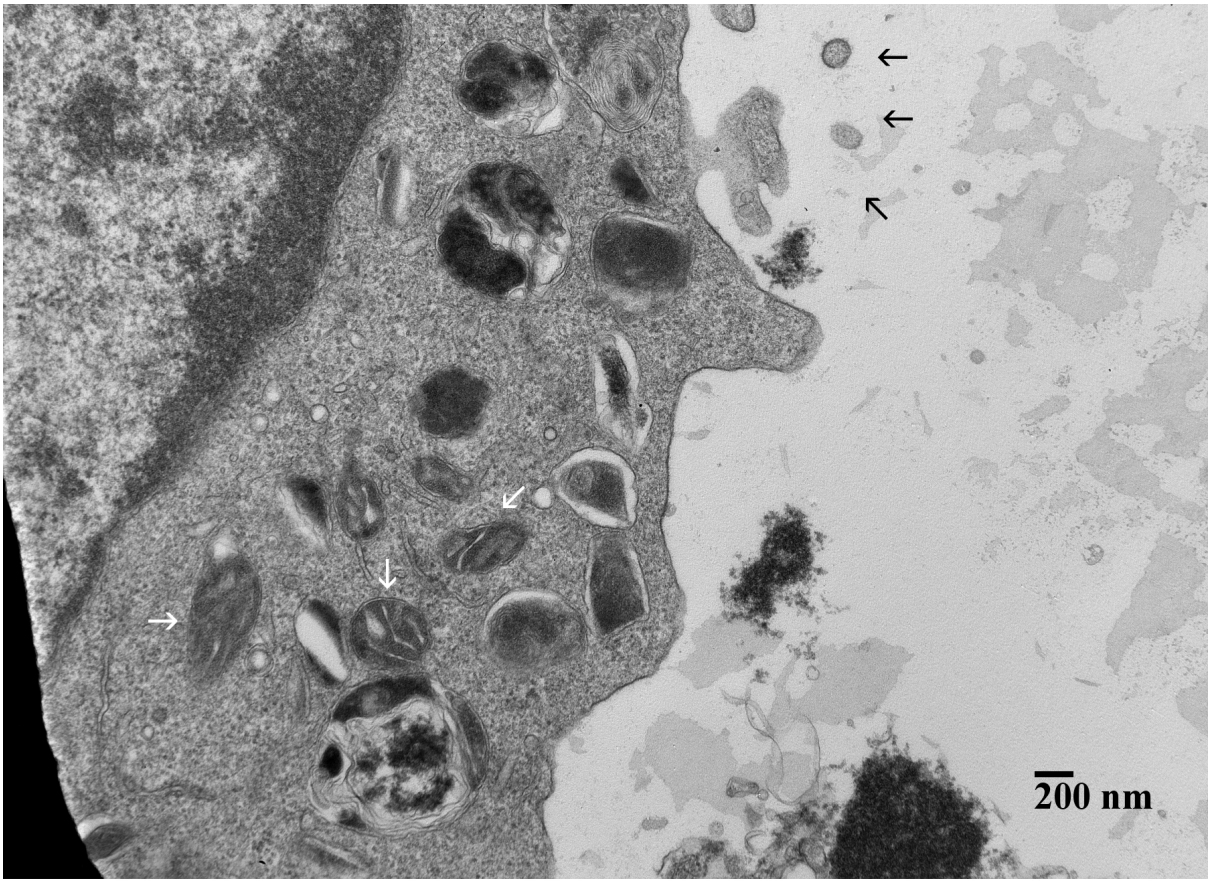

Figure 4.18: BF TEM image of a cell with pyknotic mitochondria (white arrows) after a 3 μg/mL pulse with uncoated ZnO nanopowders for 24 hours and a 2 day chase. The remaining blackened organelles/vacuoles could not be clearly identified. Presence of blebbing (black arrows) indicated an unhealthy cell state.

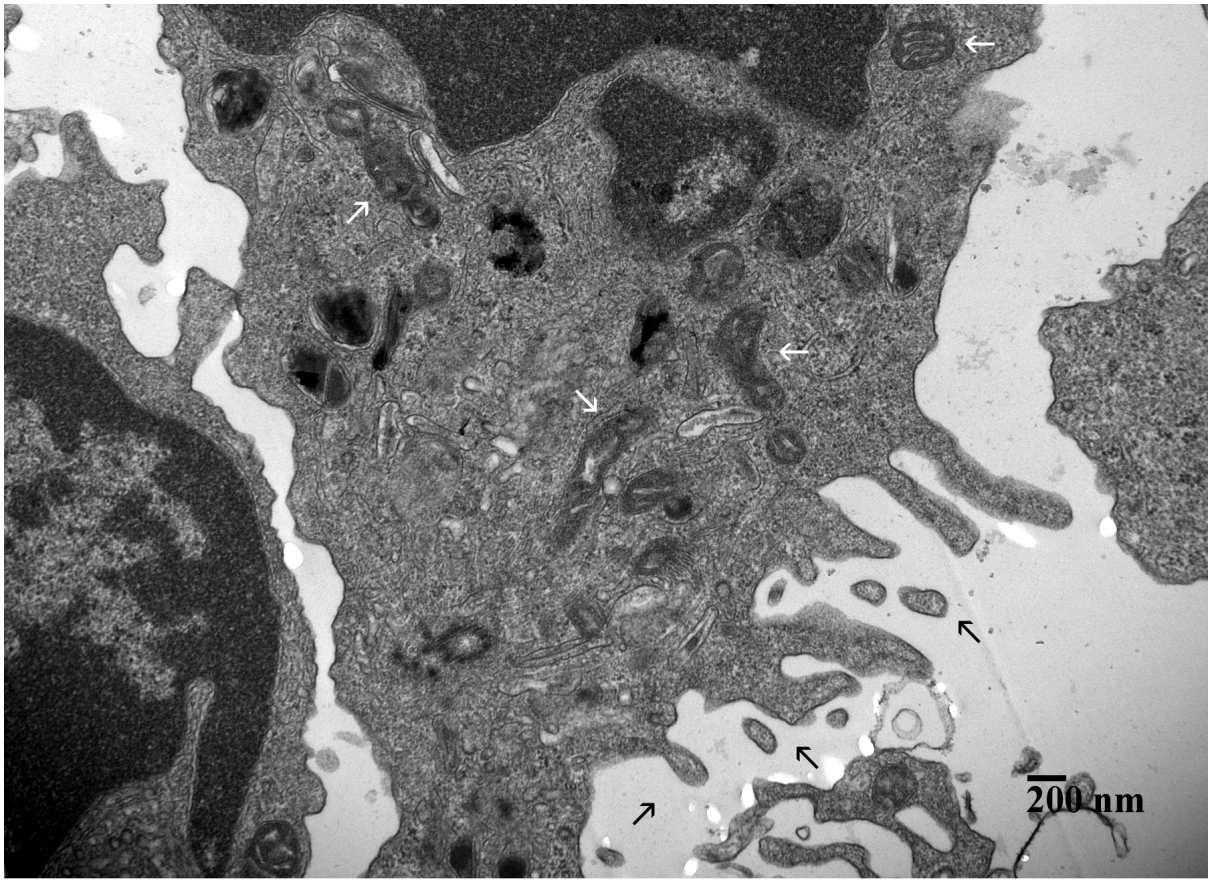

Figure 4.19: BF TEM image of a cell with pyknotic mitochondria (white arrows) after a 3 μg/mL pulse with PVA-coated ZnO nanopowders for 24 hours and a 7 day chase. The remaining blackened organelles/vacuoles could not be clearly identified. Presence of blebbing (black arrows) indicated an unhealthy cell state.

4.4 Discussion

According to the U.S. Department of Health and Human Services, zinc toxicity was mainly manifested as metal fume fever and copper deficiency. No confirmable evidence existed that zinc causes significant dermal, reproductive, developmental, or carcinogenic effects [122]. However, zinc was associated with many neurological disorders, such as Alzheimer's, Menkes, Wilson's, Pick's, and Parkinson's disease; amyotrophic lateral sclerosis; dementia; stroke; and seizures [160]. Substantial amounts of zinc were found in the brain, whether in synaptic vesicles, as free ions in the cell cytoplasm, or bound to proteins or membranes; and exogenous zinc was implicated in cell death for both *in vivo* and *in vitro* environments [161]. The results in this study combined with several other studies confirmed that ZnO was acutely toxic *in vitro* and was marked by a sudden acceleration in cell death after a certain threshold concentration. The corresponding cell death curve with $ZnCl_2$, inability to detect ZnO NPs despite various efforts to retain any remaining undissolved ZnO NPs, and evidence of mitochondrial damage as observed in Zn^{2+} neurotoxicity confirmed that ZnO dissolution contributes to the toxic response.

ZnO dissolution was affected by pH and protein. According to Degen et al. [162], ZnO formed a stable solution at pH 7.2. Figure 4.20 revealed that ZnO dissolution increased with decreasing pH, beginning at about pH 10. Depending on the starting pH of the solvent, the addition of ZnO could potentially decrease the final pH: when ZnO was added to a pH 9.9 solution, the final pH decreased to 7.6 after 3 days when it stabilised. Yang et al. [163] found that human serum albumin caused an initial increase in Zn^{2+} release before precipitation resulted in a decrease in Zn^{2+} presence. In this study, ZnO dissolution was found to be dependent on the pH within the various cell compartments (extracellular, intracellular, and lysosome). ZnO dissolution was greatest in the lysosome where pH is 5.0, while the pH of 7.2 in the extracellular and intracellular compartments resulted in significantly less dissolution. Direct analysis of the zinc ion species produced in the dissolution were required to determine if only Zn^{2+} cations were present or if other ion species as presented in Figure 4.20 were produced as well. Nonetheless, pH and the presence of protein could impact the toxic effects of Zn^{2+} cations. As other cell compartments had pH < 7.2 (e.g. Golgi apparatus pH = 6.4, endosomes pH = 6, lysosomes pH < 5 [164, 165]), the impact of Zn^{2+} toxicity was significant. Additionally, the potential decrease in pH after ZnO addition might result in suboptimal pH for certain cell parts.

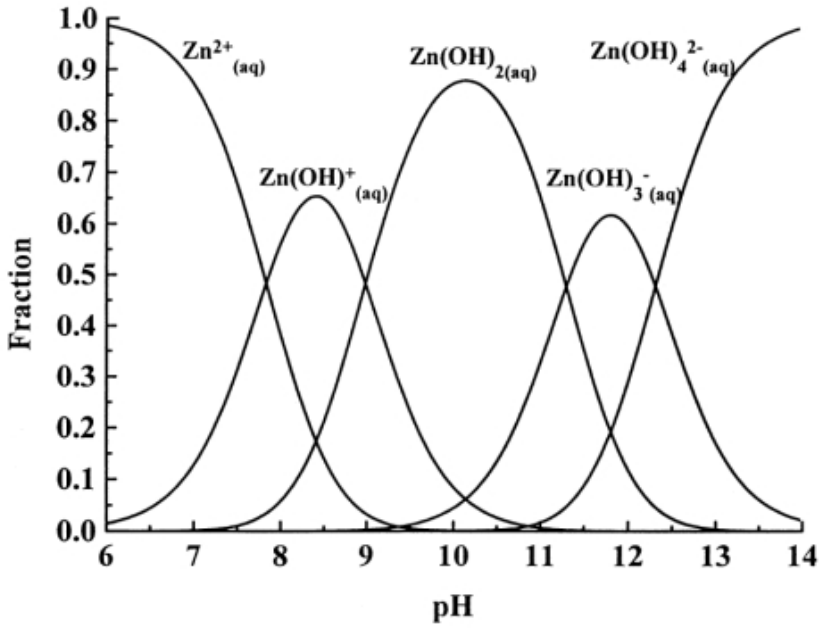

Figure 4.20: Fraction of Zn (II) ion species as Zn^{2+}, $Zn(OH)^{+}$, $Zn(OH)_2$, $Zn(OH)_3^-$ and $Zn(OH)_4^{2-}$ between pH 6 and 14 at 25°C [162].

Both the uncoated and PVA-coated ZnO nanopowders aggregated. According to both Franklin et al. [146], the ZnO dissolution rate was similar for both bulk and nanoparticulate ZnO. The accepted theory in NP research was that the rate of dissolution was proportional to the particle surface area; as NPs have higher surface area, they should dissolve faster than bulk particles. Yang et al. [163] did indeed observe that ZnO dissolution was faster for ZnO NPs than microparticles. They found that NPs released a maximum of 95% of the Zn^{2+}ions after ~50 hours incubation while microparticles released 85% after ~250 hours. One proposed reason for the differing results by Franklin et al. [146] was the observed aggregation in the nanoparticulate ZnO. Aggregation could decrease the available surface area, which would decrease the dissolution rate. This would then bring the nanoparticulate dissolution rate similar to the bulk ZnO. In this study, both the uncoated and PVA-coated ZnO nanopowders tended to aggregate. The slightly smaller individual and aggregate sizes for the PVA-coated ZnO would suggest a greater ZnO dissolution, but the slightly less toxic curve when compared to $ZnCl_2$ indicated otherwise. The ICP-OES analysis further confirmed a lower ZnO dissolution for the PVA-coated ZnO nanopowders as the ZnO dissolution in the lysosomal buffer for

the PVA-coated ZnO nanopowders was statistically significantly less than the uncoated ZnO nanopowders. These results suggested that the PVA-coating may affect ZnO dissolution. However, further studies are required to confirm that the ZnO nanopowders are fully coated with PVA. The PVA-coating was expected to promote ZnO solubility, but as both nanopowders aggregated, this suggested that there may have been problems with the PVA-coating or that the PVA-coating was ineffective with ZnO nanopowders.

The ability for ZnO NPs to absorb UV A and B (280–400 nm) light rays made them ideal candidates for UV protection in sunscreen. However, studies found that when excited, ions and free radicals such as Zn^{+}, Zn^{2+}, O^{-}, OH^{-}, and H_2O_2 could be formed. In the presence of oxygen, Zn^{+} and O^{-} species were generated [166], while in the presence of water and oxygen, the highly reactive free radical hydrogen peroxide (H_2O_2) was created [167]. The other NP commonly found in sunscreen, TiO_2, was similarly found to generate ROS in the presence of water or oxygen, including O^{-}, O_2^{-}, and OH^{-} [168]. *In vitro*, TiO_2 was found to be cytotoxic and genotoxic to lymphoma [169], cervical carcinoma [170], colon carcinoma [171], fibroblast [172], and ovary cells [173]. Coating TiO_2 with silica, alumina, or zirconium eliminated the ROS generation by UV radiation; however, Brezova et al. [174] still found that irradiating commercial sunscreen products at wavelengths > 300 nm generated ROS. It was still uncertain whether the ROS generating potential of UV-excited TiO_2 resulted in any significant consequences *in vivo* or topically, but the European Union cosmetic regulatory bodies in 2000 concluded that TiO_2 was not cytotoxic, phototoxic, or genotoxic [175]. What remains to be seen is whether ZnO behaves similarly when excited with UV radiation *in vitro*. Studies examining this possibility are required as well as whether any consequences exist *in vivo* or topically. Additionally, the PVA-coating appeared to decrease the emission intensity of the ZnO nanopowders. Depending on the *in vitro* effects of ZnO under UV radiation, the PVA-coating could attenuate any ROS generation from UV radiation.

With clear evidence that ZnO is acutely toxic, further studies are required to isolate the source of the toxicity. ZnO dissolution has been implicated, although the extent of its contribution remains unclear. Different techniques will be required to determine whether the cell death is from the Zn^{2+} cations that have dissolved in the culture medium before treatment or after it has entered the cell, to isolate whether the ZnO nanopowder itself contributes to any toxicity, and to determine which components of the cell are affected by either the Zn^{2+} cations

or ZnO nanopowder. Additionally, understanding what causes the sudden acceleration in cell death, where the threshold concentration is and what affects it, and whether such behavior is consistent across all cell types may provide further clues. As zinc has also been associated with neurological disorders, results from these studies may contribute to further understanding in this area.

4.5 Conclusion

Both the uncoated and PVA-coated ZnO nanopowders exhibited acute toxicity after only 24 hours, and the rate of toxicity increased after a certain threshold (12.5–25 μg/mL). The observed toxicity seemed to result from ZnO dissolution as supported by a similar toxicity curve between the ZnO nanopowders and $ZnCl_2$ and the slight increase in observed mitochondrial abnormality with ZnO nanopowder treatment. Acidic pH was found to promote ZnO dissolution with the lysosomal buffer (pH of 5.0) resulting in the greatest dissolution. BF TEM imaging revealed an increased presence of pronounced microfilaments and pyknotic mitochondria; however, EDX analysis could not confirm the presence of ZnO. In this study, it was the first time that:

- ZnO dissolution was compared between four different cellular buffers using ICP-OES,
- a TEM mitochondrial sterology was used to assess potential effects of the ZnO nanopowders to mitochondria,
- multiple sample preparations (cryo-immobilisation followed by freeze-drying, cryo-immobilisation by fixation then freeze-drying, and anhydrous preparation) were used in the attempt to retain ZnO nanopowders within cells.

The results from this study conclude that ZnO nanopowders are acutely toxic. As ZnO NPs may be exposed occupationally and in consumer products, it is critical to determine the safe exposure limit in NP size, amount, and duration in order to establish appropriate safety precautions.

Chapter 5

Conclusion

5.1 General discussion

For this PhD, MWNTs, SWNTs, and ZnO were assessed on primary HMM cells using a variety of cell viability assays—NR, MTT, LDH, live dead—and microscopy techniques—confocal, TEM, SEM—to attempt to draw a comprehensive conclusion on their toxic potential. The unpurified and purified MWNTs were acutely toxic with 8–43% cell death (depending on the assay used) at the highest concentration (20 μg/mL) and longest time point (4 days) while the residual iron yielded no toxicity at all. Mainly necrotic death was observed, and MWNTs entered the cells both actively and passively. They were observed in the cytoplasm and nuclei. HiPco SWNTs were mildly acutely toxic with 7–18% cell death at the highest concentration and time point while a separate set of unpurified and purified SWNTs yielded no toxicity at all. For the ZnO, both the uncoated and PVA-coated exhibited highly acute toxicity after only 24 hours. Both accelerated cell death after a certain threshold concentration (12–25 μg/mL). Comparison with $ZnCl_2$ and mitochondrial analysis suggested that ZnO dissolution contributed to the observed toxicity.

5.1.1 Comparing MWNTs and SWNTs

The MWNTs in this study were slightly more toxic than the SWNTs. When comparing the unpurified MWNTs with the HiPco SWNTs, the unpurified MWNTs were significantly toxic at $\geq$ 10 μg/mL while the HiPco SWNTs at $\geq$ 20 μg/mL. At highest concentration (20 μg/mL)

		MWNT			SWNT				ZnO				Assay	Toxicity
		Size	BET m^2/g	Impurity		Size	BET m^2/g	Impurity		Size	BET m^2/g	Impurity		
This study	Unpurified	L: 26 µm D: 68 nm	50	6.20%	HiPco	D: 1.05 nm	644	5% Fe	Uncoated	L: 80 nm S: 52 nm	13.7	0.03%	NR MTT LDH Live dead	ZnO > MWNT > SWNT
	Purified	L: 12 µm D: 68 nm	50	0%	Unpurified	D: 1.25 nm	250	70% Fe/MgO	PVA	L: 76 nm S: 52 nm	13.2	0.03%		
					Purified	D: 1.24 nm	850-900	0%						
De Nicola		L: 5-9 µm D: 110-170 nm	130	<0.1%		L: 2-20 nm D: 5-9 nm	1700	1% Co 1% Mo					Hema-cyto-meter	SWNT > MWNT
Kang		L: 70 µm D: 30 nm		0.62%		L: 2 µm D: 0.9 nm		0.81%					*E. coli* DAPI / PI	SWNT > MWNT
Walker		L: 10-20 µm D: 10-50 nm	56	3-5%		D: 0.8-2.2 nm	641	1-1.5%					WST-1 LDH	MWNT = SWNT
Karlsson		L: 5-9 µm D: 100-200 nm								L: 20-200 nm	15		Trypan blue	ZnO > MWNT
Zhu		L: 5-15 µm D: 10-20 nm		< 2%		L: 5-15 µm D: < 2 nm		< 40%	Bulk Nano	20 nm		< 0.4%	*Daphnia magna*	ZnO > SWNT > MWNT
										1 µm		<1 %		
Yang		L: < 5 µm D: 8 nm					< 0.01%			19.6 nm		< 0.1%	MTT WST LDH	ZnO > CNTs

Figure 5.1: Summary of MWNT, SWNT, and ZnO characteristics, assays, and toxicity results from this study and other studies. L = length, D = diameter, S = short dimension.

and longest time point (4 days), the unpurified MWNTs yielded a significant cell death of NR 8%, MTT 43%, and live dead 21% while the HiPco SWNTs yielded NR 18%, minimal change in the LDH, and live dead 14%. These results contradicted several other studies concluding that SWNTs were more toxic than MWNTs. Three of these studies [65, 104, 105] used the MTT assay which might explain the higher toxic response as SWNTs were found to bind the MTT formazan crystals and yield an inflated toxic response. The study by De Nicola et al. [58] determined cell death with a hemacytometer, an interactive method where the total number of cells was determined by counting the number of cells within a specified unit volume, and found that SWNTs caused greater concentration and time dependent toxicity and decrease in plasma membrane potential than MWNTs. A different study analysing the antibacterial effects found that SWNTs were more efficient at degrading *E. coli* cell membrane integrity [176]. Both studies attributed the effects to the higher surface area and smaller dimensions of the SWNTs. Indeed, the SWNTs in this study had a higher surface area and smaller dimension than the MWNTs, but when analysed closely, both De Nicola et al. [58] and Kang et al. [176] used shorter MWNTs while the length in this study was between the two studies. For surface area, the CNTs in the study by De Nicola et al. [58] were much higher while purity varied amongst all three studies. As the CNTs in all three studies were different, it was difficult to make a fair comparison (Figure 5.1). One study observed similar toxicity between MWNTs and SWNTs when exposed to human aortic endothelial cells [177]. As the CNT dimensions and properties were similar to those in this study, the differing results might be due to the different cell types used. Clearly, the numerous dissimilar factors make definite conclusions difficult. Further studies using similar or same CNTs on different cell types or using different CNTs on the same cell types may bring better insight.

As no further studies on the mechanism of uptake nor type of cell death were performed on the SWNTs due to its small size and advanced imaging techniques required, no further comparisons could be made between the two CNTs within this study.

5.1.2 Comparing all three NPs

Comparing all three NPs in this study, the general cytotoxic potential was ZnO > MWNTs > SWNTs. Although MWNTs exhibited significant cell death at a lower concentration (10

μg/mL) than ZnO (12.5 μg/mL), ZnO at 12.5 μg/mL caused much higher cell death (uncoated ZnO—NR: 28% toxicity, live dead: 45%) than the MWNTs (unpurified MWNT—NR: 9% toxicity, live dead: 6%). Three other studies concluded similarly with ZnO generally causing greater toxicity than CNTs [178, 179, 180]. Different NP characteristics, assays, and cell types were used across all studies, yet results coincided (Figure 5.1). One common assay was the LDH where Yang et al. [179] and this study observed minimal LDH leakage from both CNTs and ZnO suggesting that membrane damage was not the likely cause of cell death.

5.1.3 Efficacy of analysis techniques

The assay control experiments in this study revealed minimal to no interactions with the NPs. One exception was the NR assay where interactions with ZnO became apparent after 50 μg/mL. Fortunately, this was beyond the highest concentration used in the viability studies here. As MTT interaction with CNTs has been confirmed in several studies, the NR and live dead assays remain better assay tools. The ideal method to eliminate any doubts of possible NP and assay interactions is to integrate microscopy with viability, such as the live dead assay and TEM analysis used in this study. The disadvantages are the extensive time and effort required to yield statistically significant data; however, they can provide further certainty to the viability results.

The confocal microscope is effective only at imaging larger, reflective, or fluorescent NPs; and very little cell detail can be seen. The SEM has a higher resolving power but is limited to analysing surfaces. In order to investigate the internal interactions of NPs with cells, the TEM becomes a critical tool. Several papers have been published detailing further techniques (e.g. dark-field TEM, EF TEM, HAADF-STEM, tomography [121, 181]) that enable visualising nano-sized or non-reflective NPs in cells. However, even the TEM has its limitations in biological investigations as samples must be specially treated and specimen thickness is restricted. Consequently, the type of microscopy technique used depends on the ultimate goal. As with the viability assays, using a combination of microscopy techniques may provide greater certainty and comprehensive conclusions as each technique analyses a different facet of NP interaction with cells.

5.2 Future outlook

This study remains in the infancy stage as many confounding factors exist: size, degree of dispersion, aggregation, surface coating, and purity. Slight variations in any of these factors can alter results as detailed in the previous chapters. In a review by Hussain et al. [182], it states:

> The overall agreement for nanoscale and nanostructured materials and methods and controls, from synthesis, processing, characterization, to applications of materials containing true nanosize dimensions or nanostructures, is still in its infancy. Currently, in the study of particle characterization there is no single instrument that is the right tool for every assay and methodology, and there are in fact, more than 400 different techniques for particle counting, sizing, and characterization.

Although a general conclusion can be drawn regarding the extent MWNTs, SWNTs, and ZnO cause cell death, the cause for the toxicities remain uncertain when compared with other studies. As the synthesis condition, purification technique, purity of the NPs, use of solvent, NP surface chemistry, aggregation potential, assay type, and research model differ amongst every study, more detailed characterisation of the NPs in this study and further studies into the cell processes affected by the NPs are required. As the ZnO NPs are yielding such significant toxicity, it would be interesting to see whether ZnO nanowires will behave similarly, especially if ZnO dissolution does contribute to cell death and zinc ion species can dissolve from the nanowires. The results may reveal if any differences exist between the ZnO NPs themselves and the nanowires that are formed. The nanowires can also be compared to the MWNTs and SWNTs to further understand how these NPs fit into the fibre toxicity paradigm: whether the toxicity is caused by dimension, dose, durability, or other factors [183].

In this study, all three NPs—MWNTs, SWNTs, and ZnO—exhibited acute toxicity to varying degrees, indicating that caution is required in using these NPs. Researchers have explored ways of decreasing or eliminating the toxicities; well-dispersed MWNTs and SWNTs via surface functionalisation have been shown to reduce toxicity. Several studies using a variety of assays and imaging techniques should be performed to confirm their lack of toxicity. Prior to confirmation, products containing these NPs should remain in the research and development

stage, especially with ZnO as they exhibited such acute toxicities. Once confirmed, a consistent way of producing these NPs should be developed as slight variations in the production conditions (e.g. temperature, time, amount of carbon or catalyst, type of catalyst, contamination) can alter the characteristics of the NPs.

Occupationally, safety measures should be promoted, educated, implemented, and monitored as this is the main contact point with the raw materials before modification. Additionally, safe disposal or elimination methods should be examined. Kohler et al. [184] assessed where raw CNTs would be exposed when produced in lithium ion batteries and textiles and found that CNTs were released during production, wear and tear damage, waste disposal, and recycling. If the NPs are to be used medically, safe bodily excretion should be determined. These measures may impede technological advancement; however, preemptive cautious measures may prevent subsequent health consequences. For now, all three NPs should remain off-the-market until safer versions are developed and their safety confirmed.

Bibliography

[1] C Buzea, I I Pacheco, and K Robbie. Nanomaterials and nanoparticles: sources and toxicity. *Biointerphases*, 2(4):MR17–MR71, Dec 2007. 1.1

[2] G Oberdörster, E Oberdörster, and J Oberdörster. Nanotoxicology: an emerging discipline evolving from studies of ultrafine particles. *Environ Health Perspect*, 113(7):823–839, Jul 2005. 1.1, 1.2.2, 1.1

[3] Nanotechnology project. Online, 2009. 1.1

[4] L Greer. Nanomaterials. NE.05 Part A Lecture notes, October 2006. 1.1

[5] P Hoet, I Brüske-Hohlfeld, and O Salata. Nanoparticles - known and unknown health risks. *J Nanobiotechnol*, 2(1):12, Dec 2004. 1.2.1, 1.2.2

[6] H Brannon. Skin anatomy. Online, April 2007. 1.2.1

[7] R Alvarez-Roman, A Naik, Y Kalia, RH Guy, and H Fessi. Skin penetration and distribution of polymeric nanoparticles. *J Controlled Release*, 99(1):53–62, SEP 14 2004. 1.2.1

[8] A V Zvyagin, X Zhao, A Gierden, W Sanchez, J A Ross, and M S Roberts. Imaging of zinc oxide nanoparticle penetration in human skin in vitro and in vivo. *J Biomed Opt*, 13(6):064031, 2008. 1.2.1, 4.1

[9] F Pflucker, V Wendel, H Hohenberg, E Gartner, T Will, S Pfeiffer, R Wepf, and H Gers-Barlag. The human stratum corneum layer: An effective barrier against dermal uptake of different forms of topically applied micronised titanium dioxide. *Skin Pharmacol Appl Skin Physiol*, 14(Suppl. 1):92–97, 2001. Workshop on Structure and Function of the Stratum Corneum as a Border Organ, BERLIN, GERMANY, NOV, 2000. 1.2.1

[10] J Lademann, H Richter, A Teichmann, N Otberg, U Blume-Peytavi, J Luengo, B Weiss, U F Schaefer, C Lehr, R Wepf, and W Sterry. Nanoparticles - An efficient carrier for drug delivery into the hair follicles. *Eur J Pharm Biopharm*, 66(2):159–164, MAY 2007. 1.2.1

[11] R Toll, U Jacobi, H Richter, J Lademann, H Schaefer, and U Blume-Peytavi. Penetration profile of microspheres in follicular targeting of terminal hair follicles. *J Invest Dermatol*, 123(1):168–176, JUL 2004. 1.2.1

[12] K Donaldson and C L Tran. Inflammation caused by particles and fibers. *Inhal Toxicol*, 14(1):5–27, Jan 2002. 1.2.2, 1.2

[13] A T Florence and N Hussain. Transcytosis of nanoparticle and dendrimer delivery systems: evolving vistas. *Adv Drug Deliv Rev*, 50 Suppl 1:S69–S89, Oct 2001. 1.2.3

[14] L Szentkuti. Light microscopical observations on luminally administered dyes, dextrans, nanospheres and microspheres in the pre-epithelial mucus gel layer of the rat distal colon. *J Control Release*, 46(3):233–242, JUN 2 1997. 1.2.3

[15] P U Jani, D E Mccarthy, and A T Florence. Titanium-dioxide (rutile) particle uptake from the rat GI tract and translocation to systemic organs after oral-administrations. *Int J Pharm*, 105(2):157–168, MAY 2 1994. 1.2.3

[16] D M Mosser and J P Edwards. Exploring the full spectrum of macrophage activation. *Nat Rev Immunol*, 8(12):958–969, Dec 2008. 1.3, 1.3.1

[17] G H Bourne and J F Danielli. *International Review of Cytology*, volume 36. Academic Press, 1973. 1.3

[18] V Stvrtinová, J Jakubovský, and I Hulín. *Pathophysiology: Principles of Diseases*. Academic Electronic Press, 1995. 1.3, 1.3.1

[19] T C Jones, R D Hunt, and N W King. *Veterinary Pathology*. Wiley-Blackwell, 6th edition, March 1997. 1.3

[20] W G Spector and K M Wynne. Proliferation of macrophages in inflammation. *Agents Actions*, 6(1-3):123–126, Feb 1976. 1.3

[21] D H Cormack. *Essential Histology*. Lippincott Williams & Wilkins, 2001. 1.3

[22] D C Dale, L Boxer, and W C Liles. The phagocytes: neutrophils and monocytes. *Blood*, 112(4):935–945, Aug 2008. 1.3, 1.3.1

[23] E J Brown. Phagocytosis. *Bioessays*, 17(2):109–117, Feb 1995. 1.3.1

[24] A Aderem. How to eat something bigger than your head. *Cell*, 110(1):5–8, Jul 2002. 1.3.1

[25] C A Janeway, P Travers, M Walport, and M J Shlomchik. *Immunobiology: The Immune System in Health and Disease*. Garland Science Publishing, London, 6th edition, 2005. 1.3.1

[26] M Djaldetti, H Salman, M Bergman, R Djaldetti, and H Bessler. Phagocytosis–the mighty weapon of the silent warriors. *Microsc Res Tech*, 57(6):421–431, Jun 2002. 1.3.1

[27] A Aderem and D M Underhill. Mechanisms of phagocytosis in macrophages. *Annu Rev Immunol*, 17:593–623, 1999. 1.3.1

[28] Steinberg T H Brown E J. *Phagocytosis.*, volume 4, pages 33–64. JAI Press, Inc, 1996. 1.3.1

[29] M Dorger, S Munzing, AM Allmeling, K Messmer, and F Krombach. Differential responses of rat alveolar and peritoneal macrophages to man-made vitreous fibers in vitro. *Environ Res*, 85(3):207–214, MAR 2001. 1.3.1.1

[30] G J Cannon and J A Swanson. The macrophage capacity for phagocytosis. *J Cell Sci*, 101 (Pt 4):907–913, Apr 1992. 1.3.1.1

[31] M J Farabee. Transport in and out of cells. Internet, 2007. 1.3.2

[32] K Kirk and K Strange. Functional properties and physiological roles of organic solute channels. *Annu Rev Physiol*, 60:719–739, 1998. 1.3.2

[33] P Barker. Ion channels. NE.08 Lecture 12 notes, 2007. 1.3.2

[34] C Haslett. Granulocyte apoptosis and its role in the resolution and control of lung inflammation. *Am J Respir Crit Care Med*, 160(5 Pt 2):S5–11, Nov 1999. 1.3.3, 2b

[35] A Gewies. Introduction to apoptosis. Online, 2003. 1.3

[36] N A Monteiro-Riviere, A O Inman, and L W Zhang. Limitations and relative utility of screening assays to assess engineered nanoparticle toxicity in a human cell line. *Toxicol Appl Pharmacol*, 234(2):222–235, Jan 2009. 1.1, 1.4.1, 3.4.2, 3.5

[37] Sigma-Aldrich, Inc, 3050 Spruce St, Saint Louis, Missouri 83103, USA. *In vitro toxicology assay kit: Neutral Red based*, 2007. 1.4.1

[38] Sigma-Aldrich, Inc, 3050 Spruce St, Saint Louis, Missouri 83103, USA. *In vitro toxicology assay kit: MTT based*, 2007. 1.4.1

[39] Roche Applied Science, 68298 Mannheim, Germany. *Cytotoxicity Detection Kit (LDH)*, July 2005. 1.4.1, 3.3.1

[40] H S Slayter. *Light and Electron Microscopy*. Cambridge University Press, 1992. 1.4.2

[41] FEI Company, 5350 NE Dawson Creek Drive, Hillsboro, OR 97124-5793, USA. *All you wanted to know about Electron Microscopy*, 2004. 1.4.2.1, 1.4.2.2

[42] The Transmission Electron Microscope. Internet, 2007. Nobelprize.org. 1.4.2.1

[43] P A Midgley. Characterisation techniques on the nanoscale. NE.01 Lecture notes, 2006. 1.4.2.1, 1.4.2.2, 1.4.2.3

[44] M J Dykstra. *A Manual of Applied Techniques for Biological Electron Microscopy*. Springer, 1993. 1.4.2.1

[45] J P Sibilia. *A Guide to Materials Characterization and Chemical Analysis*. Wiley-VCH, 2nd edition, 1996. 1.4.2.3

[46] Molecular probes. Internet. updated 2006, cited 2007 Feb 21. 1.4.2.4, 2.3.3.1

[47] L C Junqueira and J Carneiro. *Basic Histology: Text and Atlas*. McGraw-Hill Companies, Inc, 11th edition, 2005. 1.4.2.4

[48] D Semwogerere and E R Weeks. *Confocal Microscopy*, pages 1–10. Taylor & Francis, 2005. 1.4.2.4, 1.4, 3.4.6

[49] E Oberdörster. Manufactured nanomaterials (fullerenes, C60) induce oxidative stress in the brain of juvenile largemouth bass. *Environ Health Perspect*, 112(10):1058–1062, Jul 2004. 1.5

[50] P Miaudet, S Badaire, M Maugey, A. Derré, V Pichot, P Launois, P Poulin, and C Zakri. Hot-drawing of single and multiwall carbon nanotube fibers for high toughness and alignment. *Nano Lett*, 5(11):2212–2215, Nov 2005. 2.1

[51] V N Popov. Carbon nanotubes: properties and application. *Mat Sci Eng R*, 43(3):61–102, JAN 2004. 2.1, 3.1

[52] J Cho and I M Daniel. Reinforcement of carbon/epoxy composites with multi-wall carbon nanotubes and dispersion enhancing block copolymers. *Scripta Mater*, 58(7):533 – 536, 2008. 2.1

[53] M Endo, S Koyama, Y Matsuda, T Hayashi, and Y A Kim. Thrombogenicity and blood coagulation of a microcatheter prepared from carbon nanotube-nylon-based composite. *Nano Lett*, 5(1):101–105, Jan 2005. 2.1

[54] B S Harrison and A Atala. Carbon nanotube applications for tissue engineering. *Biomater*, 28(2):344–353, Jan 2007. 2.1

[55] M Bottini, S Bruckner, K Nika, N Bottini, S Bellucci, A Magrini, A Bergamaschi, and T Mustelin. Multi-walled carbon nanotubes induce T lymphocyte apoptosis. *Toxicol Lett*, 160(2):121–126, Jan 2006. 2.1, 2.3.3.1

[56] S Hirano, S Kanno, and A Furuyama. Multi-walled carbon nanotubes injure the plasma membrane of macrophages. *Toxicol Appl Pharmacol*, 232(2):244–251, Oct 2008. 2.1, 2.4

[57] A Simon-Deckers, B Gouget, M Mayne-L'Hermite, N Herlin-Boime, C Reynaud, and M Carriere. In vitro investigation of oxide nanoparticle and carbon nanotube toxicity

and intracellular accumulation in A549 human pneumocytes. *Toxicol*, 253(1-3):137–146, Nov 2008. 2.1, 2.1, 2.1, 2.3.4, 2.4

[58] M De Nicola, S Bellucci, E Traversa, G De Bellis, F Micciulla, and L Ghibelli. Carbon nanotubes on Jurkat cells: effects on cell viability and plasma membrane potential. *J Phys Condens Matt*, 20(47), Nov 2008. 4th International Workshop and Summer School on Nanoscience and Nanotechnology, Thessaloniki, GREECE, 2007. 2.1, 2.3.3.1, 2.4, 3.1, 5.1.1

[59] L Ding, J Stilwell, T Zhang, O Elboudwarej, H Jiang, J P Selegue, P A Cooke, J W Gray, and F F Chen. Molecular characterization of the cytotoxic mechanism of multiwall carbon nanotubes and nano-onions on human skin fibroblast. *Nano Lett*, 5(12):2448–2464, Dec 2005. 2.1, 2.3.3.1

[60] N A Monteiro-Riviere, R J Nemanich, A O Inman, Y Y Wang, and J E Riviere. Multiwalled carbon nanotube interactions with human epidermal keratinocytes. *Toxicol Lett*, 155(3):377–384, Mar 2005. 2.1, 2.1

[61] L Zhu, D W Chang, L Dai, and Y Hong. DNA damage induced by multiwalled carbon nanotubes in mouse embryonic stem cells. *Nano Lett*, 7(12):3592–3597, Dec 2007. 2.1, 2.3.6

[62] B Kateb, M Van Handel, L Zhang, M J Bronikowski, H Manohara, and B Badie. Internalization of MWCNTs by microglia: possible application in immunotherapy of brain tumors. *Neuroimage*, 37 Suppl 1:S9–17, 2007. 2.1

[63] K Pulskamp, S Diabaté, and H F Krug. Carbon nanotubes show no sign of acute toxicity but induce intracellular reactive oxygen species in dependence on contaminants. *Toxicol Lett*, 168(1):58–74, Jan 2007. 2.1, 2.1, 2.4, 3.1, 3.4.4, 3.5

[64] C Grabinski, S Hussain, K Lafdi, L Braydich-Stolle, and J Schlager. Effect of particle dimension on biocompatibility of carbon nanomaterials. *Carbon*, 45(14):2828–2835, Nov 2007. 2.1

[65] A M Schrand, L Dai, J J Schlager, S M Hussain, and E Osawa. Differential biocompatibility of carbon nanotubes and nanodiamonds. *Diamond Relat Mat*, 16(12):2118–2123, Dec 2007. 2.1, 5.1.1

[66] A A Shvedova, V Castranova, E R Kisin, D Schwegler-Berry, A R Murray, V Z Gandelsman, A Maynard, and P Baron. Exposure to carbon nanotube material: assessment of nanotube cytotoxicity using human keratinocyte cells. *J Toxicol Environ Health A*, 66(20):1909–1926, Oct 2003. 2.1

[67] I Fenoglio, G Greco, M Tomatis, J Muller, E Raymundo-Pi nero, Fr Béguin, A Fonseca, J B Nagy, D Lison, and B Fubini. Structural defects play a major role in the acute lung toxicity of multiwall carbon nanotubes: physicochemical aspects. *Chem Res Toxicol*, 21(9):1690–1697, Sep 2008. 2.2, 2.1

[68] J Muller, F Huaux, A Fonseca, J B Nagy, N Moreau, M Delos, E Raymundo-Pi nero, F Béguin, M Kirsch-Volders, I Fenoglio, B Fubini, and D Lison. Structural defects play a major role in the acute lung toxicity of multiwall carbon nanotubes: toxicological aspects. *Chem Res Toxicol*, 21(9):1698–1705, Sep 2008. 2.2, 2.1, 2.3.4

[69] C A Poland, R Duffin, I Kinloch, A Maynard, W A H Wallace, A Seaton, V Stone, S Brown, W Macnee, and K Donaldson. Carbon nanotubes introduced into the abdominal cavity of mice show asbestos-like pathogenicity in a pilot study. *Nat Nanotechnol*, 3(7):423–428, Jul 2008. 2.1

[70] J Muller, F Huaux, N Moreau, P Misson, J F Heilier, M Delos, M Arras, A Fonseca, J B Nagy, and D Lison. Respiratory toxicity of multi-wall carbon nanotubes. *Toxicol Appl Pharmacol*, 207(3):221–231, Sep 2005. 2.1

[71] L Lacerda, A Soundararajan, R Singh, G Pastorin, K T. Al-Jamal, J Turton, P Frederik, M A. Herrero, S L A Bao, D Emfietzoglou, S Mather, W T. Phillips, M Prato, A Bianco, B Goins, and K Kostarelos. Dynamic imaging of functionalized multi-walled carbon nanotube systemic circulation and urinary excretion. *Adv Mater*, 20(2):225, Jan 2008. 2.1

[72] V Raffa, G Ciofania, S Nitodasb, T Karachalios, D D'Alessandro, M Masinie, and A Cuschieria. Can the properties of carbon nanotubes influence their internalization by living cells? *Carbon*, 46:1600–1610, 2008. 2.1

[73] D M Brown, I A Kinloch, U Bangert, A H Windle, D M Walter, G S Walker, C A Scotchford, K Donaldson, and V Stone. An in vitro study of the potential of carbon nanotubes and nanofibres to induce inflammatory mediators and frustrated phagocytosis. *Carbon*, 45(9):1743–1756, Aug 2007. 2.1

[74] C F Lopez, S O Nielsen, P B Moore, and M L Klein. Understanding nature's design for a nanosyringe. *Proc Natl Acad Sci U S A*, 101(13):4431–4434, Mar 2004. 2.1, 2.1, 2.4

[75] W Huang, Y Wang, GH Luo, and F Wei. 99.9% purity multi-walled carbon nanotubes by vacuum high-temperature annealing. *Carbon*, 41(13):2585–2590, 2003. 2.2.2

[76] M Endo, Y A Kim, Y Fukai, T Hayashi, M Terrones, H Terrones, and M S Dresselhaus. Comparison study of semi-crystalline and highly crystalline multiwalled carbon nanotubes. *Appl Phys Lett*, 79(10):1531–1533, Sep 2001. 2.2.2

[77] R Andrews, D Jacques, D Qian, and E C Dickey. Purification and structural annealing of multiwalled carbon nanotubes at graphitization temperatures. *Carbon*, 39(11):1681–1687, 2001. 2.2.2

[78] T W Clyne and J A Curran. Porosity in plasma electrolytic oxide coatings. *Acta Mater*, 54(7):1985–93, April 2006. 2.2.3

[79] A Jorio, R Saito, G Dresselhaus, and M S Dresselhaus. Determination of nanotubes properties by Raman spectroscopy. *Philos Trans R Soc London, Ser A*, 362(1824):2311–2336, Nov 2004. 2.2.3

[80] E M Denholm and F M Wolber. A simple method for the purification of human peripheral blood monocytes: a substitute for Sepracell-MN. *J Immunol Methods*, 144(2):247–251, Nov 1991. 2.2.4

[81] K B Cheong, S K Cheong, and N Y Boo. Surfactant protein A and stable microbubble formation in tracheal aspirates. *Malays J Pathol*, 18(2):101–105, Dec 1996. 2.2.5

[82] S H Yu and F Possmayer. Role of bovine pulmonary surfactant-associated proteins in the surface-active property of phospholipid mixtures. *Biochim Biophys Acta*, 1046(3):233–241, Oct 1990. 2.2.5

[83] M C Buford, R F Hamilton, and A Holian. A comparison of dispersing media for various engineered carbon nanoparticles. *Part Fibre Toxicol*, 4:6, 2007. 2.2.5

[84] S J Hardwick, L Hegyi, K Clare, N S Law, K L Carpenter, M J Mitchinson, and J N Skepper. Apoptosis in human monocyte-macrophages exposed to oxidized low density lipoprotein. *J Pathol*, 179(3):294–302, Jul 1996. 2.2.9, 2.3.3.1, 2.8

[85] A Warley and J N Skepper. Long freeze-drying times are not necessary during the preparation of thin sections for X-ray microanalysis. *J Microsc*, 198(Pt 2):116–123, May 2000. 2.2.10

[86] V A Fadok, D R Voelker, P A Campbell, J J Cohen, D L Bratton, and P M Henson. Exposure of phosphatidylserine on the surface of apoptotic lymphocytes triggers specific recognition and removal by macrophages. *J Immunol*, 148(7):2207–2216, Apr 1992. 2.3.3.1

[87] T Cindrova, J N Skepper, and L A Sellers. The signalling mechanisms activated concomitantly with the proliferative or apoptotic responses evoked by oxysterols in human umbilical vein endothelial cells (HUVECs). *Brit J Pharm*, 135(Suppl. S), MAR 2002. 3

[88] K Rydell-Törmänen, L Uller, and J S Erjefält. Direct evidence of secondary necrosis of neutrophils during intense lung inflammation. *Eur Respir J*, 28(2):268–274, Aug 2006. 2b

[89] J Muller, I Decordier, P H Hoet, N Lombaert, L Thomassen, F Huaux, D Lison, and M Kirsch-Volders. Clastogenic and aneugenic effects of multi-wall carbon nanotubes in epithelial cells. *Carcinogenesis*, 29(2):427–433, Feb 2008. 2.3.6, 2.3.6

[90] J M Worle-Knirsch, K Pulskamp, and H F Krug. Oops they did it again! Carbon nanotubes hoax scientists in viability assays. *Nano Lett*, 6(6):1261–1268, Jun 2006. 2.4, 3.4.2, 3.5

[91] A Casey, E Herzog, M Davoren, F M Lyng, H J Byrne, and G Chambers. Spectroscopic analysis confirms the interactions between single walled carbon nanotubes and various dyes commonly used to assess cytotoxicity. *Carbon*, 45(7):1425–1432, Jun 2007. 2.4, 3.1, 3.4.2, 3.5

[92] P Wick, P Manser, L K Limbach, U Dettlaff-Weglikowska, F Krumeich, S Roth, W J Stark, and A Bruinink. The degree and kind of agglomeration affect carbon nanotube cytotoxicity. *Toxicol Lett*, 168(2):121–131, Jan 2007. 2.4, 3.1

[93] F Tian, D Cui, H Schwarz, G G Estrada, and H Kobayashi. Cytotoxicity of single-wall carbon nanotubes on human fibroblasts. *Toxicol In Vitro*, 20(7):1202–1212, Oct 2006. 2.4

[94] M Zheng, A Jagota, E D Semke, B A Diner, R S McLean, S R Lustig, R E Richardson, and N G Tassi. DNA-assisted dispersion and separation of carbon nanotubes. *Nat Mater*, 2(5):338–342, May 2003. 2.4

[95] L Lacerda, A Bianco, M Prato, and K Kostarelos. Carbon nanotubes as nanomedicines: from toxicology to pharmacology. *Adv Drug Deliv Rev*, 58(14):1460–1470, Dec 2006. 3.1

[96] A Windle. Carbon nanostructures: buckyballs and nanotubes. NE.05 Part B Lecture notes, November 2006. 3.1

[97] Wikipedia. SWNT chiral vector. Online, April 2005. 3.1

[98] Wikipedia. SWNT types, 2008. 3.1

[99] P Ball. Roll up for the revolution. *Nature*, 414(6860):142–144, Nov 2001. 3.1

[100] J H Hafner, C L Cheung, A T Woolley, and C M Lieber. Structural and functional imaging with carbon nanotube AFM probes. *Prog Biophys Mol Biol*, 77(1):73–110, 2001. 3.1

[101] D Pantarotto, J P Briand, M Prato, and A Bianco. Translocation of bioactive peptides across cell membranes by carbon nanotubes. *Chem Commun*, (1):16–17, Jan 2004. 3.1

[102] N W S Kam and H Dai. Single walled carbon nanotubes for transport and delivery of biological cargos. *Phys Status Solidi B*, 243(13):3561–3566, Nov 2006. 20th International Winterschool/Euroconference on Electronic Properties of Novel Materials, Kirchberg, AUSTRIA, MAR 04-11, 2006. 3.1

[103] N W S Kam, M O'Connell, J A Wisdom, and H Dai. Carbon nanotubes as multifunctional biological transporters and near-infrared agents for selective cancer cell destruction. *Proc Natl Acad Sci U S A*, 102(33):11600–11605, Aug 2005. 3.1

[104] G Jia, H Wang, L Y, X Wang, R Pei, T Yan, Y Zhao, and X Guo. Cytotoxicity of carbon nanomaterials: single-wall nanotube, multi-wall nanotube, and fullerene. *Environ Sci Technol*, 39(5):1378–1383, Mar 2005. 3.1, 5.1.1

[105] D Zhang, C Yi, J Zhang, Y Chen, X Yao, and M Yang. The effects of carbon nanotubes on the proliferation and differentiation of primary osteoblasts. *Nanotechnol*, 18(47), Nov 2007. 3.1, 5.1.1

[106] D Cui, F Tian, C S Ozkan, M Wang, and H Gao. Effect of single wall carbon nanotubes on human HEK293 cells. *Toxicol Lett*, 155(1):73–85, Jan 2005. 3.1, 3.5

[107] M Pacurari, X J Yin, J Zhao, M Ding, S S Leonard, D Schwegler-Berry, B S Ducatman, D Sbarra, M D Hoover, V Castranova, and V Vallyathan. Raw single-wall carbon nanotubes induce oxidative stress and activate MAPKs, AP-1, NF-kappaB, and Akt in normal and malignant human mesothelial cells. *Environ Health Perspect*, 116(9):1211–1217, Sep 2008. 3.1, 3.1, 3.4.5, 3.5

[108] A Shvedova, E Kisin, A Murray, D Schwegler-Berry, V Gandelsman, P Baron, A Maynard, M Gunter, and V Castranova. Exposure of human bronchial cells to carbon nanotubes caused oxidative stress and cytotoxicity. In *Proceedings of the Meeting of the SFRR Europe*, 2003. 3.1, 3.4.4, 3.5

[109] C S S R Kumar, editor. *Nanomaterials for Cancer Diagnosis*. Wiley-VCH, 2007. 3.1

[110] R Singh, D Pantarotto, L Lacerda, G Pastorin, C Klumpp, M Prato, A Bianco, and K Kostarelos. Tissue biodistribution and blood clearance rates of intravenously admin-

istered carbon nanotube radiotracers. *Proc Natl Acad Sci U S A*, 103(9):3357–3362, Feb 2006. 3.1

[111] L Guo, A Von Dem Bussche, M Buechner, A Yan, A B Kane, and R H Hurt. Adsorption of essential micronutrients by carbon nanotubes and the implications for nanotoxicity testing. *Small*, 4(6):721–727, Jun 2008. 3.1, 3.5

[112] M Davoren, E Herzog, A Casey, B Cottineau, G Chambers, H. J. Byrne, and F M Lyng. In vitro toxicity evaluation of single walled carbon nanotubes on human A549 lung cells. *Toxicol In Vitro*, 21(3):438–448, APR 2007. 3.1, 3.4.3, 3.5

[113] N R Jacobsen, G Pojana, P White, P Moller, C A Cohn, K S Korsholm, U Vogel, A Marcomini, S Loft, and H Wallin. Genotoxicity, cytotoxicity, and reactive oxygen species induced by single-walled carbon nanotubes and C-60 fullerenes in the FE1-Muta (TM) mouse lung epithelial cells. *Environ Molec Mutagensis*, 49(6):476–487, Jul 2008. 3.1

[114] O Zeni, R Palumbo, R Bernini, L Zeni, M Sarti, and M R Scarfi. Cytotoxicity investigation on cultured human blood cells treated with single-wall carbon nanotubes. *Sensors*, 8(1):488–499, Jan 2008. 3.1, 3.4.5

[115] E Herzog, H J. Byrne, A Casey, M Davoren, A G Lenz, K L. Maier, A Duschl, and G J Oostingh. SWCNT suppress inflammatory mediator responses in human lung epithelium in vitro. *Toxicol Appl Pharmacol*, 234(3):378–390, Feb 2009. 3.1, 3.4.3

[116] M J Bronikowski, P A Willis, D T Colbert, K A Smith, and R E Smalley. Gas-phase production of carbon single-walled nanotubes from carbon monoxide via the hipco process: a parametric study. *J Vac Sci Technol A*, 19(4, Part 2):1800–1805, Jul-Aug 2001. 47th International Symposium of AVS, BOSTON, MASSACHUSETTS, OCT 02-06, 2000. 3.2.1

[117] S S Islam and K A Shah. Method for determination of nature of single-wall carbon nanotubes (SWCNTs) in a bundle prepared by chemical vapor deposition technique. *IEICE Electron. Express*, 3(1):5–10, 2006. 3.2.3.1

[118] J Bendall. *The Effects of the Encapsulation of Inorganic Halides within Carbon Nanotubes*. PhD thesis, University of Cambridge, February 2006. 3.2, 3.3.3.1

[119] A Casey, E Herzog, F M Lyng, H J Byrne, G Chambers, and M Davoren. Single walled carbon nanotubes induce indirect cytotoxicity by medium depletion in A549 lung cells. *Toxicol Lett*, 179(2):78–84, Jun 2008. 3.4.3

[120] E Herzog, H J Byrne, M Davoren, A Casey, A Duschl, and G J Oostingh. Dispersion medium modulates oxidative stress response of human lung epithelial cells upon exposure to carbon nanomaterial samples. *Toxicol Appl Pharmacol*, 236(3):276–281, May 2009. 3.5

[121] A E Porter, M Gass, K Muller, J N Skepper, P A Midgley, and M Welland. Direct imaging of single-walled carbon nanotubes in cells. *Nat Nanotechnol*, 2(11):713–717, Nov 2007. 3.5, 5.1.3

[122] Toxicological profile for zinc, August 2005. 4.1, 4.3.4, 4.4

[123] B L Vallee and K H Falchuk. The biochemical basis of zinc physiology. *Physiol Rev*, 73(1):79–118, Jan 1993. 4.1, 4.3.3

[124] A Takeda. Movement of zinc and its functional significance in the brain. *Brain Res Brain Res Rev*, 34(3):137–148, Dec 2000. 4.1

[125] Z L Wang. Zinc oxide nanostructures: growth, properties and applications. *J Phys Condens Matter*, 16(25):R829–R858, 2004. 4.1

[126] B Y Oh, M C Jeong, T H Moon, W Lee, J M Myoung, J Y Hwang, and D S Seo. Transparent conductive Al-doped ZnO films for liquid crystal displays. *J Appl Phys*, 99(12), JUN 15 2006. 4.1

[127] D C Look. Recent advances in ZnO materials and devices. *Mater Sci Eng B*, 80(1-3):383 – 387, 2001. 4.1

[128] K Keis, C Bauer, G Boschloo, A Hagfeldt, K Westermark, H Rensmo, and H Siegbahn. Nanostructured ZnO electrodes for dye-sensitized solar cell applications. *J. Photochem. Photobiol., A*, 148(1-3, Sp. Iss. SI):57–64, MAY 31 2002. 1st International Conference on Semiconductor Photochemistry (SP-1), GLASGOW, SCOTLAND, JUL 23-25, 2001. 4.1

[129] D D Lee and D S Lee. Environmental gas sensors. *IEEE Sens J*, 1(3):214–224, Oct 2001. 4.1

[130] L Jing, Z Xu, X Sun, J Shang, and W Cai. The surface properties and photocatalytic activities of ZnO ultrafine particles. *Appl Surf Sci*, 180(3-4):308 – 314, 2001. 4.1

[131] S M Al-Hilli and M Willander. Optical properties of zinc oxide nano-particles embedded in dielectric medium for UV region: Numerical simulation. *J Nanopart Res*, 8(1):79–97, FEB 2006. 4.1

[132] T Iwasaki, M Satoh, T Masuda, and T Fujita. Powder design for UV-attenuating agent with high transparency for visible light. *J Mater Sci*, 35(16):4025–4029, AUG 2000. 4.1

[133] M Roselli, A Finamore, I Garaguso, M Serena Britti, and E Mengheri. Zinc oxide protects cultured enterocytes from the damage induced by *Escherichia coli*. *J Nutr*, 133(12):4077–4082, Dec 2003. 4.1

[134] N Padmavathy and R Vijayaraghavan. Enhanced bioactivity of ZnO nanoparticles–an antimicrobial study. *Sci Technol Adv Mater*, 9(3):035004 (7pp), 2008. 4.1

[135] P Kaye, H Young, and I O'Sullivan. Metal fume fever: a case report and review of the literature. *Emerg Med J*, 19(3):268–269, May 2002. 4.1

[136] W S Beckett, D F Chalupa, A Pauly-Brown, D M Speers, J C Stewart, M W Frampton, M J Utell, L S Huang, C Cox, W Zareba, and G Oberdörster. Comparing inhaled ultrafine versus fine zinc oxide particles in healthy adults: a human inhalation study. *Am J Respir Crit Care Med*, 171(10):1129–1135, May 2005. 4.1

[137] J M Fine, T Gordon, L C Chen, P Kinney, G Falcone, and W S Beckett. Metal fume fever: characterization of clinical and plasma il-6 responses in controlled human exposures to zinc oxide fume at and below the threshold limit value. *J Occup Environ Med*, 39(8):722–726, Aug 1997. 4.1

[138] G Hallmans and S Lidén. Penetration of 65Zn through the skin of rats. *Acta Derm Venereol*, 59(2):105–112, 1979. 4.1

[139] M S Agren. Percutaneous absorption of zinc from zinc oxide applied topically to intact skin in man. *Dermatologica*, 180(1):36–39, 1990. 4.1

[140] A O Gamer, E Leibold, and B van Ravenzwaay. The in vitro absorption of microfine zinc oxide and titanium dioxide through porcine skin. *Toxicol In Vitro*, 20(3):301–307, Apr 2006. 4.1

[141] H A Jeng and J Swanson. Toxicity of metal oxide nanoparticles in mammalian cells. *J Environ Sci Health A Tox Hazard Subst Environ Eng*, 41(12):2699–2711, 2006. 4.1, 4.3.3

[142] W Lin, Y Xu, C C Huang, Y Ma, K B. Shannon, D R Chen, and Y W Huang. Toxicity of nano- and micro-sized ZnO particles in human lung epithelial cells. *J Nanopart Res*, 11(1):25–39, JAN 2009. 4.1, 4.3.3

[143] W M U Daniels, J Hendricks, R Salie, and S J van Rensburg. A mechanism for zinc toxicity in neuroblastoma cells. *Metab Brain Dis*, 19(1-2):79–88, Jun 2004. 4.1

[144] T Xia, M Kovochich, M Liong, L Mädler, B Gilbert, H Shi, J I Yeh, J I Zink, and A E Nel. Comparison of the mechanism of toxicity of zinc oxide and cerium oxide nanoparticles based on dissolution and oxidative stress properties. *ACS Nano*, 2(10):2121–2134, Oct 2008. 4.1, 4.3.4

[145] V Sharma, R K Shukla, N Saxena, D Parmar, M Das, and A Dhawan. DNA damaging potential of zinc oxide nanoparticles in human epidermal cells. *Toxicol Lett*, 185(3):211–218, Mar 2009. 4.1, 4.3.3

[146] N M Franklin, N J Rogers, S C Apte, G E Batley, G E Gadd, and P S Casey. Comparative toxicity of nanoparticulate ZnO, bulk ZnO, and ZnCl2 to a freshwater microalga (*Pseudokirchneriella subcapitata*): the importance of particle solubility. *Environ Sci Technol*, 41(24):8484–8490, Dec 2007. 4.1, 4.3.4, 4.4

[147] M Heinlaan, A Ivask, I Blinova, H C Dubourguier, and A Kahru. Toxicity of nanosized and bulk ZnO, CuO and TiO2 to bacteria *Vibrio fischeri* and crustaceans *Daphnia magna* and *Thamnocephalus platyurus*. *Chemosphere*, 71(7):1308–1316, Apr 2008. 4.1, 4.3.4

[148] T Fujii, M Noami, K Tomita, and Y Furuya. PVA copolymer: the new coating agent. *Pharm Tech Europe*, 20(10), October 2008. 4.2.1

[149] H K Kammler, L Madler, and S E Pratsinis. Flame synthesis of nanoparticles. *Chem Eng Technol*, 24(6):583–596, JUN 2001. 4.2.1

[150] L Madler, H K Kammler, R Mueller, and S E Pratsinis. Controlled synthesis of nanostructured particles by flame spray pyrolysis. *J Aero Sci*, 33(2):369–389, FEB 2002. 4.2.1

[151] S Haywood, D M Simpson, G Ross, and R J Beynon. The greater susceptibility of North Ronaldsay sheep compared with Cambridge sheep to copper-induced oxidative stress, mitochondrial damage and hepatic stellate cell activation. *J Comp Pathol*, 133(2-3):114–127, 2005. 4.2.6.1

[152] J Hradil, A Pisarev, M Babic, and D Horak. Dextran-modified iron oxide nanoparticles. *China Particuol*, 5(1-2):162–168, Feb-Apr 2007. 4.3.1.1

[153] H M Cheng, H C Hsu, S L Chen, W T Wu, C C Kao, L J Lin, and W F Hsieh. Efficient UV photoluminescence from monodispersed secondary ZnO colloidal spheres synthesized by sol-gel method. *J Cryst Growth*, 277(1-4):192–199, APR 15 2005. 4.3.1.2

[154] A Umar, B Karunagaran, E-K Suh, and Y B Hahn. Structural and optical properties of single-crystalline ZnO nanorods grown on silicon by thermal evaporation. *Nanotechnol*, 17(16):4072–4077, AUG 28 2006. 4.3.1.2

[155] Gang Xiong, U. Pal, and J. Garcia Serrano. Correlations among size, defects, and photoluminescence in ZnO nanoparticles. *J Appl Phys*, 101(2):024317, 2007. 4.3.1.3

[156] X Deng, Q Luan, W Chen, Y Wang, M Wu, H Zhang, and Z Jiao. Nanosized zinc oxide particles induce neural stem cell apoptosis. *Nanotechnol*, 20(11):115101, Mar 2009. 4.3.3

[157] K E Dineley, T V Votyakova, and I J Reynolds. Zinc inhibition of cellular energy production: implications for mitochondria and neurodegeneration. *J Neurochem*, 85(3):563–570, May 2003. 4.3.5

[158] S L Sensi, H Z Yin, S G Carriedo, S S Rao, and J H Weiss. Preferential Zn2+ influx through Ca2+-permeable AMPA/kainate channels triggers prolonged mitochondrial superoxide production. *Proc Natl Acad Sci U S A*, 96(5):2414–2419, Mar 1999. 4.3.5

[159] P Marin, M Israël, J Glowinski, and J Prémont. Routes of zinc entry in mouse cortical neurons: role in zinc-induced neurotoxicity. *Eur J Neurosci*, 12(1):8–18, Jan 2000. 4.3.5

[160] M S Horning, L J Blakemore, and P Q Trombley. Endogenous mechanisms of neuroprotection: role of zinc, copper, and carnosine. *Brain Res*, 852(1):56–61, Jan 2000. 4.4

[161] M P Cuajungco and G J Lees. Zinc metabolism in the brain: relevance to human neurodegenerative disorders. *Neurobiol Dis*, 4(3-4):137–169, 1997. 4.4

[162] A Degen and M Kosec. Effect of pH and impurities on the surface charge of zinc oxide in aqueous solution. *J Eur Ceram Soc*, 20(6):667–673, MAY 2000. 4.4, 4.20

[163] Z Yang and C Xie. Zn2+ release from zinc and zinc oxide particles in simulated uterine solution. *Colloids Surf B Biointerfaces*, 47(2):140–145, Feb 2006. 4.4, 4.4

[164] M M Wu, J Llopis, S Adams, J M McCaffery, M S Kulomaa, T E Machen, H P Moore, and R Y Tsien. Organelle pH studies using targeted avidin and fluorescein-biotin. *Chem Biol*, 7(3):197–209, Mar 2000. 4.4

[165] K L Audus and T J Raub. *Biological barriers to protein delivery*. Springer, 1993. 4.4

[166] M Anpo and Y Kubokawa. Photoluminescence of zinc-oxide powder as a probe of electron-hole surface processes. *J Phys Chem*, 88(23):5556–5560, 1984. 4.4

[167] D R Dixon and T W Healey. Photochemical redox reactions at zinc oxide-water interface in additive-free systems. *Aust J Chem*, 24(6):1193–&, 1971. 4.4

[168] R Konaka, E Kasahara, W C Dunlap, Y Yamamoto, K C Chien, and M Inoue. Irradiation of titanium dioxide generates both singlet oxygen and superoxide anion. *Free Radic Biol Med*, 27(3-4):294–300, Aug 1999. 4.4

[169] Y Nakagawa, S Wakuri, K Sakamoto, and N Tanaka. The photogenotoxicity of titanium dioxide particles. *Mutat Res*, 394(1-3):125–132, Nov 1997. 4.4

[170] R Cai, Y Kubota, T Shuin, H Sakai, K Hashimoto, and A Fujishima. Induction of cytotoxicity by photoexcited TiO2 particles. *Cancer Res*, 52(8):2346–2348, Apr 1992. 4.4

[171] A P Zhang and Y P Sun. Photocatalytic killing effect of TiO2 nanoparticles on Ls-174-t human colon carcinoma cells. *World J Gastroenterol*, 10(21):3191–3193, Nov 2004. 4.4

[172] W G Wamer, J J Yin, and R R Wei. Oxidative damage to nucleic acids photosensitized by titanium dioxide. *Free Radic Biol Med*, 23(6):851–858, 1997. 4.4

[173] T Uchino, H Tokunaga, M Ando, and H Utsumi. Quantitative determination of OH radical generation and its cytotoxicity induced by TiO(2)-UVA treatment. *Toxicol In Vitro*, 16(5):629–635, Oct 2002. 4.4

[174] V Brezová, S Gabcová, D Dvoranová, and A Stasko. Reactive oxygen species produced upon photoexcitation of sunscreens containing titanium dioxide (an EPR study). *J Photochem Photobiol B*, 79(2):121–134, May 2005. 4.4

[175] Opinion of the scientific committee on cosmetic products and non-food products intended for consumers concerning titanium dioxide, October 2000. 4.4

[176] S Kang, M Herzberg, D F Rodrigues, and M Elimelech. Antibacterial effects of carbon nanotubes: size does matter! *Langmuir*, 24(13):6409–6413, Jun 2008. 5.1.1

[177] V G Walker, Z Li, T Hulderman, D Schwegler-Berry, M L Kashon, and P P Simeonova. Potential in vitro effects of carbon nanotubes on human aortic endothelial cells. *Toxicol Appl Pharmacol*, 236(3):319–328, May 2009. 5.1.1

[178] H L Karlsson, P Cronholm, J Gustafsson, and L Möller. Copper oxide nanoparticles are highly toxic: a comparison between metal oxide nanoparticles and carbon nanotubes. *Chem Res Toxicol*, 21(9):1726–1732, Sep 2008. 5.1.2

[179] H Yang, C Liu, D Yang, H Zhang, and Z Xi. Comparative study of cytotoxicity, oxidative stress and genotoxicity induced by four typical nanomaterials: the role of particle size, shape and composition. *J Appl Toxicol*, 29(1):69–78, Jan 2009. 5.1.2

[180] X Zhu, L Zhu, Z Duan, R Qi, Y Li, and Y Lang. Comparative toxicity of several metal oxide nanoparticle aqueous suspensions to Zebrafish (*Danio rerio*) early developmental stage. *J Environ Sci Health A Tox Hazard Subst Environ Eng*, 43(3):278–284, Feb 2008. 5.1.2

[181] A E Porter, K Muller, J Skepper, P Midgley, and M Welland. Uptake of C-60 by human monocyte macrophages, its localization and implications for toxicity: Studied by high resolution electron microscopy and electron tomography. *Acta Biomater*, 2(4):409–419, JUL 2006. 5.1.3

[182] S M Hussain, L K Braydich-Stolle, A M Schrand, R C Murdock, K O Yu, D M Mattie, J J Schlager, and M Terrones. Toxicity evaluation for safe use of nanomaterials: Recent achievements and technical challenges. *Adv Mater*, 21(16):1549–1559, APR 27 2009. 5.2

[183] L D Maxim, J G Hadley, R M Potter, and R Niebo. The role of fiber durability/biopersistence of silica-based synthetic vitreous fibers and their influence on toxicology. *Regul Toxicol Pharm*, 46(1):42 – 62, 2006. 5.2

[184] A R Kohler, C Som, A Helland, and F Gottschalk. Studying the potential release of carbon nanotubes throughout the application life cycle. *J Clean Prod*, 16(8-9):927–937, 2008. 5.2